ANALYTICAL AND EXPERIMENTAL INVESTIGATIONS OF HYBRID AIR FOIL BEARINGS

A Thesis

by

MANISH KUMAR

Submitted to the Office of Graduate Studies of
Texas A&M University
in partial fulfillment of the requirements for the degree of

MASTER OF SCIENCE

August 2008

Major Subject: Mechanical Engineering

ANALYTICAL AND EXPERIMENTAL INVESTIGATIONS OF HYBRID AIR FOIL BEARINGS

A Thesis

by

MANISH KUMAR

Submitted to the Office of Graduate Studies of
Texas A&M University
in partial fulfillment of the requirements for the degree of

MASTER OF SCIENCE

Chair of Committee,	Daejong Kim
Committee Members,	Alan B. Palazzolo
	Hae-Kwon Jeong
Head of Department,	Dennis O' Neal

August 2008

Major Subject: Mechanical Engineering

ABSTRACT

Analytical and Experimental Investigations of Hybrid Air Foil Bearings. (August 2008)

Manish Kumar, B.Tech., Indian Institute of Technology

Chair of Advisory Committee: Dr. Daejong Kim

Air foil bearings offer several advantages over oil-lubricated bearings in high speed micro-turbomachinery. With no contact between the rotor and bearings, the air foil bearings have higher service life and consequently lesser standstills between operations. However, the foil bearings have reliability issues that come from dry rubbing during start-up/shutdown and limited heat dissipation capability. Regardless of lubricating media, the hydrodynamic pressure generated provides only load support but no dissipation of parasitic energy generated by viscous drag and the heat conducted from other parts of the machine through the rotor.

The present study is a continuation of the work on hybrid air foil bearings (HAFB) developed by Kim and Park, where they present a new concept of air foil bearing combining hydrodynamic air foil bearing with hydrostatic lift. Their experimental studies show that HAFB has superior performance compared to its hydrodynamic counterpart in load capacity and cooling performance.

In this article, the bearing stiffness and damping coefficients of HAFB are calculated using a linear perturbation method developed for HAFB. The study focuses on circular HAFB with a single continuous top foil supported by bump foil. The research also

includes a parametric study which outlines the dependence of the stiffness and damping coefficients on various design parameters like supply pressure (P_s), feed parameter (Γ_s), excitation frequency (ν), and bearing number (Λ).

Furthermore the present research also includes experimental investigation of HAFB with bump foil as compliant structure. In the first phase of the experimental research a high speed test facility was designed and fabricated. The facility has the capability of running up to 90,000 RPM and has an electric motor drive. This article gives detailed description of this test rig and also includes data acquired during the commissioning phase of the test rig. The test rig was then used to measure the load capacity of HAFB.

ACKNOWLEDGEMENTS

I would like to thank my committee chair, Dr. Kim, and my committee members, Dr. Palazzolo, Dr. Hung and Dr. Jeong, for their guidance and support throughout the course of this research.

My thanks also go to my friends and colleagues at the Turbomachinery Lab at Texas A&M University. This project is supported by the Texas Engineering Experiment Station, Turbomachinery Laboratory at Texas A&M University and Turbomachinery Research Consortium.

NOMENCLATURE

A_b : Effective area that one bump covers

A_0 : Reference orifice curtain area, $A_0 = \pi d_o C$

C : Nominal clearance

p_a : Ambient pressure

P : Non-dimensional pressure, $P = \dfrac{p}{p_a}$

P_0 : Non-dimensional zeroth order pressure

p_s : Supply pressure

C_b : Non-dimensional damping coefficient of elastic foundation, $C_b = \dfrac{c_b C \omega}{p_a A_b}$

c_b : Bump damping

h : Film thickness

H : Non-dimensional film thickness, $H = \dfrac{h}{C}$

$H_{X,Y}$: Non-dimensional perturbed film thickness gradient in X and Y

k : Ratio of specific heats for air

K_b : Non-dimensional stiffness coefficient of elastic foundation, $K_b = \dfrac{k_b C}{p_a A_b}$

k_b : Bump stiffness

m_r : Rotor mass

$\dot{m}_s$: Mass flow rate

R_g : Gas constant of air

T : Gas temperature

C_d : Discharge coefficient

$\dot{M}_s$: Non-dimensional mass flow rate, $\dot{M}_s = \dfrac{12\mu R_g T\dot{m}_s}{{p_a}^2 C^3}$

Γ_s : Feed parameter, $\Gamma_s = \dfrac{12\mu C_d A_0 \sqrt{R_g T}}{p_a C^3}$

$P_{X,Y}$: Non-dimensional perturbed pressure gradient in X and Y

R : Bearing radius

U : Non-dimensional bump deflection, $U = \dfrac{u}{C}$

u : Bump deflection

Z : Non-dimensional axial coordinate, $Z = \dfrac{z}{R}$

Greeks

ΔH : Non-dimensional perturbed film thickness

ΔP : Non-dimensional perturbed pressure field

η : Structural loss factor, $\eta = \dfrac{c_b \omega_s}{k_b}$

ω : Rotor speed

ω_s : Excitation frequency

μ : Air viscosity

Λ : Bearing number, $\Lambda = \dfrac{6\mu\omega}{p_a}\left(\dfrac{R}{C}\right)^2$

ν : Excitation frequency ratio (EFR), $\nu = \dfrac{\omega_s}{\omega}$

θ : Circumferential coordinate, $\theta = \dfrac{x}{R}$

τ : Non-dimensional time, $\tau = \omega t$

TABLE OF CONTENTS

Page

LIST OF FIGURES

Page

LIST OF TABLES

Page

1 INTRODUCTION

Air/Gas foil bearings have shown tremendous promise in the field of high-speed micro to mid-sized turbomachinery. Compared to roller element bearings, air foil bearings circumvent the need of oil lubrication circuits and complex seals making the system less complicated and more environmentally friendly. Because of lesser number of parts required to support rotating machinery and no lubrication/seal system, air foil bearings have higher reliability. Consequently air foil bearings require lesser scheduled maintenance resulting in higher service life and low operating costs.

Air foil bearings have been successfully deployed in many turbomachinery applications. Air Cycle Machines (ACM) used in Environmental Control System (ECS) of aircrafts use air foil bearings. ECS with air foil bearings in Boeing 747 aircraft have demonstrated a robust service life with Mean Time Before Failure (MTBF) exceeding 100,000 hours [1]. Other applications include rotary flow compressor, micro-turbines [2] and oil-free turbochargers [3].

Air Foil bearings, however, have reliability issues that stem from the wear caused by dry rubbing during startups and stops. These bearings also have limited heat dissipation capability of parasitic heat generated within the turbomachinery. The reason behind the low dissipation is the low heat capacity of air. Another disadvantage of air foil bearing is that they have low load capacity as compared to roller or oil bearing. Low viscosity of air is the reason behind the limited load capacity.

This thesis follows the style of *Journal of Tribology*.

The air foil bearing consists of a top foil and compliant elastic foundation which sustains the applied load and provides structural stiffness and damping. The compliant structure can also accommodate misalignments and distortions of the shaft. One of the most commonly used compliant structures is a corrugated bump foil. Air foil bearing with bump foil as complaint structure is shown in Figure 1. Hydrodynamic pressure is generated when the shaft drags the air between the rotor surface and the top foil. Because of the hydrodynamic pressure the rotor is elevated and compliant structure deforms elastically.

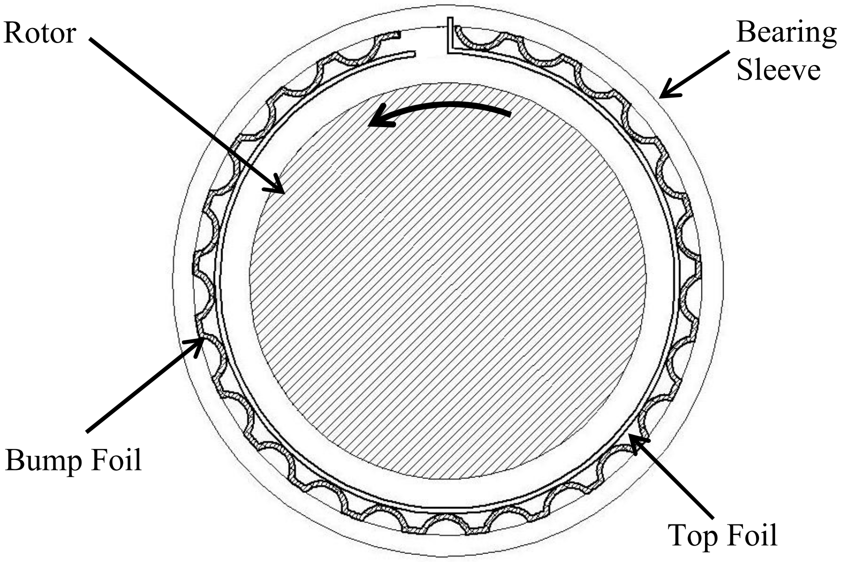

Figure 1: Hydrodynamic air foil bearing

1.1 Scope of the present research

The present study is a continuation of the work done by Kim and Park [4], where they adopt time-domain orbit method to investigate the rotordynamic performance of a rigid rotor in cylindrical mode. Ideally air foil bearings (and most air bearings) are best-suited for high speed rigid rotors (with large shaft diameter) operating below their first bending critical speed. However, air foil bearings are often considered with flexible rotors with locally large shaft diameter in regions where the bearings are located. Adoption of time-domain non-linear orbit simulations to these flexible rotors supported on air foil bearings require enormous computational time and thus is not practical. For general synchronous rotordynamic vibration analyses, stiffness and damping coefficients of the air foil bearings can be used with commercial rotordynamic software.

As pointed out earlier, non-linear time domain rotordynamic analyses on a flexible rotor supported by air foil bearings require intense computational effort. As a preliminary design step, usage of bearing stiffness and damping coefficients with commercial rotordynamic software can reduce the computational time and provide quick design guidelines of whole rotor-bearing system.

In this article, the bearing stiffness and damping coefficients of HAFB are calculated using a linear perturbation method developed for HAFB. The first phase of the study focuses on circular HAFB with a single continuous top foil supported by bump foils (page 11). The thesis also includes a parametric study which outlines the dependence of the stiffness and damping coefficients on various design parameters like supply pressure (P_s), feed parameter (Γ_s), excitation frequency (ν), and bearing number (Λ).

The above mentioned parametric study gives us only a theoretical insight into the HAFB. To completely understand the characteristics of these bearings or any other air bearings an experimental investigation is very important. One of the impediments in doing that is the requirement of a facility which can give the capability to test the air bearings under moderate to high speed operations. The second phase of this study addresses this issue and centers on the design and fabrication of such a test rig. Following the fabrication of the test rig, the HAFB was tested for the load capacity at various operating speeds. The load capacity study followed the procedure outlined in [4].

2 LITERATURE REVIEW ON AIR FOIL BEARINGS

Extensive research in air foil bearings have been made over the past three decades. One of the first works on the analytical side was done by Heshmat et al [5]. They solved the Reynolds equation numerically to find the pressure profile, film thickness and load capacity. They also evaluated the effect of various structural, geometric and operational variables on the performance of the air foil bearing.

Ku and Heshmat [6] present a theoretical model of corrugated bump foil strip considering frictional forces between the bump foil and the bearing housing and also between the bump foil and the top foil. They also included local interaction forces, variable load distribution and different bump geometries in the investigation. They showed that higher frictional coefficients between the top foil and the bump foil can help in achieving efficient Coulomb damping and higher stiffness. Their follow up paper [7], presented the experimental verification of the model.

Peng and Carpino [8] calculated the stiffness and damping coefficient of an elastically supported gas foil bearing. For their structural model they used a thin and extendable material as foil surface. The model neglected any bending and membrane effect and inertia of foil was also neglected. The Reynolds equation to obtain pressure and film thickness was solved using finite element methods. Dynamic coefficients were solved using perturbation method where Reynolds equation was linearized to yield force coefficients. Their results showed that the compliance of the bearing at relatively low speeds primarily depends on the hydrodynamic gas film. But, at high speeds the stiffness of the hydrodynamic gas film becomes very large and hence the compliance is due to the underlying elastic foundation. Later, Carpino [9] also developed a finite element perturbation approach to predict foil bearing rotor dynamic coefficients.

Han et al [10] studied the characteristics of air bearings with external pressurization. Their analysis involved determination of force coefficients using perturbation analysis and a parametric study to see the dependence of these coefficients on bearing size, external pressure and number of supply restrictors. The study also involved theoretical calculation to predict the rotor orbit and was verified with experimental investigations.

Dellacorte and Valco [11] introduced a simple “Rule of Thumb” to estimate the load capacity of air foil bearings. The rule empirically related the load capacity of the bearing to the bearing size and operating speed using data available in the literature and from the experiments done by the authors.

Radil et al [12] studied the dependence of load capacity of air foil bearings on the radial clearance. They showed that air foil bearings have an optimum radial clearance, below which thermal run-away can occur in the bearing which leads to gas film rupture. Above the optimum value the load capacity of the bearing is reduced.

Wilde and San Andrés [13] did a comparative study involving rotordynamic predictions and test response of a three lobed hybrid gas bearings. The bearing was termed as hybrid because it was both hydrostatic, from external pressurization, and hydrodynamic in nature. They showed that by increasing the external pressurization the critical speeds can be shifted but the effective damping of the bearing is decreased. The measurements done by them also showed that whirl ratio decreased with increase in supply pressure.

Peng and Khonsari [14] developed a thermo-hydrodynamic model to analyze air foil bearings. The temperature distribution on the top-foil of the bearing was evaluated by solving coupled Reynolds equation and Energy equation. The analysis model developed by them incorporated the compressibility of air and temperature dependence of air viscosity. The numerical results were verified with the existing experimental data and a comparative study of the thermal performance of solid walled bearing and foil bearing was also conducted.

More recently Song and Kim [15] developed a new kind of compliant elastic foundation made of commercially-available compression springs. They did analytical and experimental studies to determine the performance of this new air foil bearing. The analytical studies involved stiffness calculation of springs under lateral loading and the results were validated with experimental investigation. Further in analytical studies a computational model was developed using time-domain orbit simulations that could predict limit cycle behaviors encountered in air foil bearings. They showed that as with any other air bearing with elastic foundations; their bearing could suppress the vibrations at critical speeds but not the onset of instability. Experimental investigations revealed the possibility of large load capacity with appropriate cooling.

In subsequent studies, Kim [16] conducted parametric studies on two different types of air foil bearings, circular and three-pads, and investigated the dependence of rotor dynamic stability on the distribution of stiffness and damping of the compliant surface. The study showed that rotordynamic characteristics are more sensitive to the overall bearing geometry rather than stiffness and damping distribution within the elastic foundation. The author compared the results from linear stability analysis and orbit simulations and found different onset speed of instability from the two methods. The discrepancy between the two methods was attributed to the limitation of linear stability analysis in the stability predictions.

Kim and Park [4] developed air foil bearing with external pressurization. The complaint structure of the bearing developed by them had compression springs arranged axially and was similar in construction to the bearing in [15]. Their bearing was both hydrodynamic and hydrostatic in nature and hence was a Hybrid air foil bearing (HAFB). External pressurization was provided through the bump foil and top foil to the rotor surface. Four external feed tubes were used for this purpose. The study included both numerical analysis and experimental investigation. The numerical investigation was concerned with the evaluation of pressure profile and film thickness of the bearing under hybrid operation. Coast-down simulations for the bearing were also performed. The simulations showed that hybrid operation increased the onset speed of instability as compared to hydrodynamic operation. Their experimental investigation dealt with the estimation of load capacity and starting torque of hybrid air foil bearing. They showed that load capacity of the bearing increased under hybrid operation and also the frictional drag associated during startups was reduced considerably.

3 DETERMINATION OF FORCE COEFFICIENTS*

3.1 Description of hybrid air foil bearing

A schematic of the proposed bearing is shown in Figure 2. The bearing shown has a single continuous top foil and a two strip bump foil. External pressurization is supplied through four feed tubes which directly discharge air through the top foil to the bearing clearance. Circumferential arrangement of the feed tubes is shown in Figure 2(b). The feed tubes are located at θ = 72°, 166°, 247°, and 341°. The purpose of the unsymmetrical placement of the feed tubes is to put the orifices on top of the bumps as described in Figure 2. Table 1 gives the parameters of the bearing used during the simulations, the bump stiffness was calculated using the formula for free-free case presented by Iordanoff [17].

---

* Reprinted with permission from "Parametric Studies on Dynamic Performance of Hybrid Airfoil Bearing" by Kumar, M., and Kim, D., 2008. *Journal of Engineering for Gas Turbines and Power*, **130**, Copyright 2008 by ASME.

Table 1: Bearing parameters – Simulation

Parameters	Value
Bearing diameter, 2*R*	38.1 mm
Bearing axial length, *L*	38.1 mm
Nominal clearance, *C*	32 μm
Bump stiffness per unit area	4.7 GN/m^3
Top foil thickness	100μm
Orifice Size (Diameter)	0.5 mm

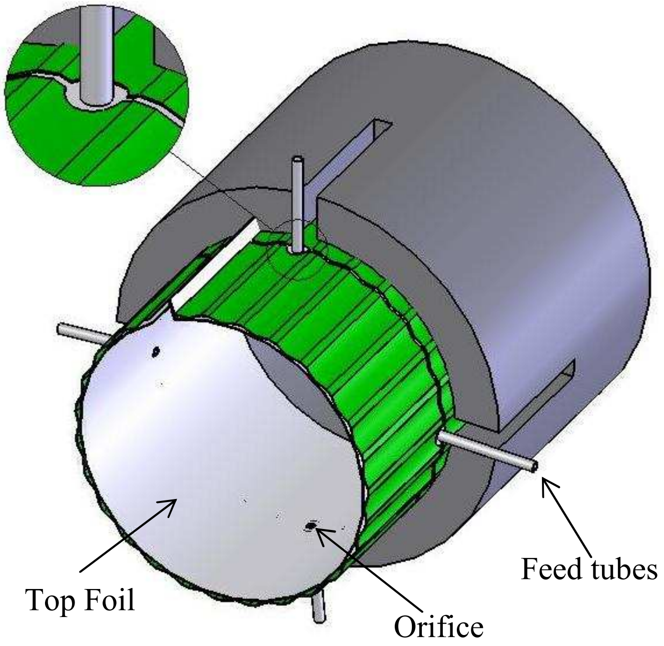

(a) Schematic description of HAFB

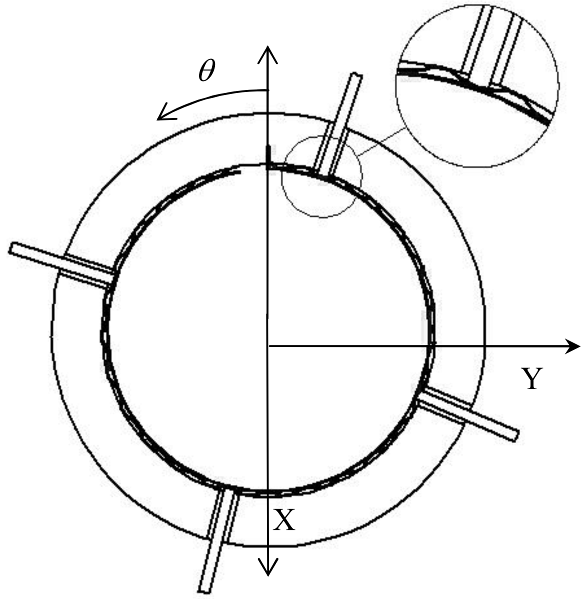

(b) Coordinate system for analysis

Figure 2: Schematic descriptions of circular HAFB and coordinate system for analysis

3.2 Solution methodology

The solution methodology followed in this paper is based on Finite Volume methods. Figure 3 shows the grid scheme for the control volume and the dynamic mass balance.

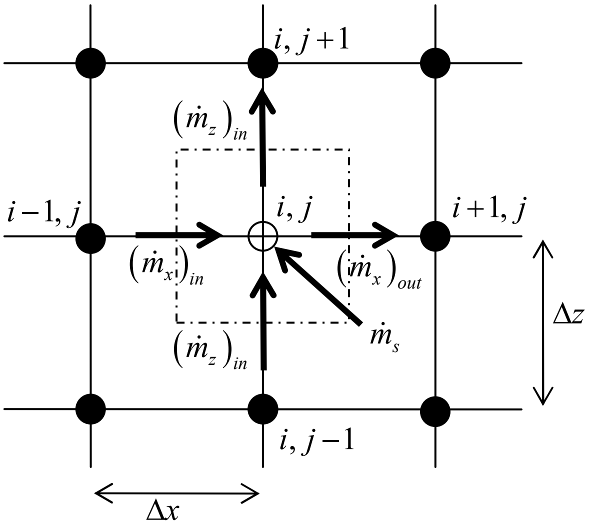

Figure 3: Mesh defined for analysis

In Figure 3, $\dot{m}_s$ is the air mass flow rate through the orifice. Also, $\dot{m}_x$ and $\dot{m}_z$ from the classical formulation of Couette-Poiseuille flows are defined as

$$\dot{m}_x = \left(-\frac{1}{12\mu} \frac{p}{R_g T} h^3 \frac{\partial p}{\partial x} + \frac{p}{R_g T} \frac{hR\omega}{2} \right) \Delta z \tag{1}$$

$$\dot{m}_z = \left(-\frac{1}{12\mu} \frac{p}{R_g T} h^3 \frac{\partial p}{\partial z} \right) \Delta x \tag{2}$$

In the above equations x is a local coordinate attached on the bearing surface along the circumferential direction, z is a coordinate in axial direction, h is a film thickness, p is pressure, μ is viscosity of air, R_g is the gas constant of air and T is the temperature of supplied air. The dynamic mass balance of the control volume under transient condition gives

$$\left(\dot{m}_x + \dot{m}_z\right)_{in} + \dot{m}_s - \left(\dot{m}_x + \dot{m}_z\right)_{out} = \frac{d\left(\rho V\right)}{dt} = \frac{\Delta x \Delta z}{R_g T}\frac{d\left(ph\right)}{dt} \tag{3}$$

Substituting values from (1) and (2) in the above equation we get the Reynolds Equation for compressible fluids with hydrostatic supply

$$\frac{\partial}{\partial x}\left(-\frac{1}{12\mu}ph^3\frac{\partial p}{\partial x} + \frac{R\omega}{2}ph\right) + \frac{\partial}{\partial z}\left(-\frac{1}{12\mu}ph^3\frac{\partial p}{\partial z}\right) + \frac{\partial(ph)}{\partial t} = \frac{R_g T\dot{m}_s}{\Delta x \Delta z} \tag{4}$$

Non-dimensionalizing Eq. (4) yields (see Appendix A for more details)

$$\frac{\dot{M}_s}{\Delta\theta\Delta Z} + \frac{\partial}{\partial\theta}\left(PH^3\frac{\partial P}{\partial\theta}\right) + \frac{\partial}{\partial Z}\left(PH^3\frac{\partial P}{\partial\theta}\right) = \Lambda\frac{\partial}{\partial\theta}\left(PH\right) + 2\Lambda\nu\frac{\partial}{\partial\tau}\left(PH\right) \tag{5}$$

where $P = \frac{p}{P_a}$, $\theta = \frac{x}{R}$, $Z = \frac{z}{R}$, $\tau = \omega_s t$, $H = \frac{h}{C}$, bearing number $\Lambda = \frac{6\mu\omega}{p_a}\left(\frac{R}{C}\right)^2$, excitation frequency ratio $\nu = \frac{\omega_s}{\omega}$, and $\dot{M}_s = \frac{12\mu R_g T\dot{m}_s}{p_a{}^2 C^3}$. ω_s is the excitation frequency. See Figure 2 for more details on the coordinate system used.

Assuming the flow through the orifice as an isentropic process, the mass flow rates of the compressible fluid for the choked and un-choked conditions are given by

Un-Choked: $\frac{P}{P_s} > \left(\frac{2}{k+1}\right)^{\frac{k}{(k-1)}} = 0.5283$

$$\dot{M}_S = \Gamma_s P_s H \left[\frac{2k}{k-1} \left(\left(\frac{P}{P_s} \right)^{2/k} - \left(\frac{P}{P_s} \right)^{(k+1)/k} \right) \right]^{1/2} \tag{6}$$

Choked: $\frac{P}{P_s} < \left(\frac{2}{k+1} \right)^{\frac{k}{(k-1)}} = 0.5283$

$$\dot{M}_S = \Gamma_s P_s H \left(2 \frac{k}{k+1} \right)^{1/2} \left(\frac{2}{k+1} \right)^{1/(k-1)} \tag{7}$$

where $\Gamma_s = \frac{12\mu C_d A_0 \sqrt{R_g T}}{p_a C^3}$ is a feed parameter, P_s is the supply pressure, k is the ratio of specific heats for air, C_d is a discharge coefficient. In the feed parameter, A_0 is the reference orifice curtain area defined as $A_0 = \pi d_o C$, where d_0 is the orifice diameter.

For the perturbation analysis, equation of motion for the elastic foundation corresponding to the computational finite domain should be developed. For simplicity, the inertia of the elastic foundation is neglected and it is further assumed that each elastic foundation supports the corresponding top foil independently. Then the equation of motion of elastic foundation becomes

$$pA_b = k_b u + c_b \frac{du}{dt} \tag{8}$$

where k_b and c_b are the effective stiffness and viscous damping coefficients of the elastic foundation, and A_b is effective area for the elastic foundation. Note the stiffness per unit area in Table 1 is k_b / A_b. Assuming the motion of elastic foundation is sinusoidal in normal operating conditions, the equivalent viscous damping coefficient can be found from structural damping model through structural loss factor, i.e.,

$\eta = \dfrac{c_b \omega_s}{k_b}$. For the present simulations, the structural loss coefficient of 0.25 is used for every elastic foundation. The chosen structural loss factor is from the empirical results of a well-designed bump foil bearings [18], [19] and [20]. Writing the bump dynamic equation in non-dimensional form yields

$$P = K_b U + C_b \nu \frac{dU}{d\tau} \tag{9}$$

where $K_b = \dfrac{k_b C}{p_a A_b}$ and $C_b = \dfrac{c_b C \omega}{p_a A_b}$ are non-dimensional bump stiffness and damping coefficients, respectively. Linearizing Eqs. (5) and (9) yields the zeroth and first order equations (see Appendix B for details)

Zeroth Order:

$$\begin{aligned} &\frac{\partial}{\partial \theta}\left(P_0 H_0^3 \frac{\partial P_0}{\partial \theta} \right) + \frac{\partial}{\partial z}\left(P_0 H_0^3 \frac{\partial P_0}{\partial z} \right) + \left(\frac{2k}{k-1} \right)^{1/2} \frac{\Gamma_s P_s}{\Delta\theta \Delta Z} f(H_0, P_0) \\ &= \Lambda \frac{\partial}{\partial \theta}\left[P_0 H_0 \right] + 2\Lambda \nu \frac{\partial}{\partial \tau}\left[P_0 H_0 \right] \end{aligned} \tag{10}$$

First Order:

$$\begin{aligned} &\frac{\partial}{\partial \theta}\left[P_0 H_0{}^3 \frac{\partial P_\alpha}{\partial \theta} \right] + \frac{\partial}{\partial Z}\left[P_0 H_0{}^3 \frac{\partial P_\alpha}{\partial Z} \right] \\ &+ \left(\frac{2k}{k-1} \right)^{\frac{1}{2}} \frac{\Gamma_s P_s}{\Delta Z \Delta \theta} \left[\left. \frac{\partial f(P,H)}{\partial P} \right|_{P_0, H_0} P_\alpha + \left. \frac{\partial f(P,H)}{\partial H} \right|_{P_0, H_0} \left(\frac{P_a}{K_b \left(1 + \eta i \right)} + g_\alpha \right) \right] \\ &\frac{\partial}{\partial \theta}\left[\left(3H_0{}^2 P_0 \left(\frac{P_a}{K_b \left(1 + \eta i \right)} + g_\alpha \right) + H_0{}^3 P_\alpha \right) \left(\frac{\partial P_0}{\partial \theta} \right) \right] \\ &+ \frac{\partial}{\partial Z}\left[\left(3H_0{}^2 P_0 \left(\frac{P_a}{K_b \left(1 + \eta i \right)} + g_\alpha \right) + H_0{}^3 P_\alpha \right) \left(\frac{\partial P_0}{\partial Z} \right) \right] \\ &= \Lambda \frac{\partial}{\partial \theta}\left(P_0 \left(\frac{P_a}{K_b \left(1 + \eta i \right)} + g_\alpha \right) + P_\alpha H_0 \right) + 2\Lambda \nu i P_0 \left(P_0 \left(\frac{P_a}{K_b \left(1 + \eta i \right)} + g_\alpha \right) + P_\alpha H_0 \right) \end{aligned} \tag{11}$$

where $\alpha = X, Y$ and $g_X = \cos\theta$, $g_Y = \sin\theta$. Note that P_X and P_Y are complex number with real and imaginary parts. The values of $f(H_0, P_0)$, $\left.\dfrac{\partial f(P,H)}{\partial P}\right|_{P_0,H_0}$ and $\left.\dfrac{\partial f(P,H)}{\partial H}\right|_{P_0,H_0}$ for choked and un-choked conditions are given below.

Choked

$$f(H_0, P_0) = H_0 \tag{12}$$

$$\left.\frac{\partial f(P,H)}{\partial P}\right|_{P_0,H_0} = 0 \tag{13}$$

$$\left.\frac{\partial f(P,H)}{\partial H}\right|_{P_0,H_0} = 1 \tag{14}$$

Un-choked

$$f(H_0, P_0) = H_0 \left(\left(\frac{P_0}{P_s} \right)^{\frac{2}{k}} - \left(\frac{P_0}{P_s} \right)^{\frac{(k+1)}{k}} \right)^{\frac{1}{2}} \tag{15}$$

$$\left.\frac{\partial f(P,H)}{\partial P}\right|_{P_0,H_0} = H_0 \frac{1}{2} \left(\left(\frac{P_0}{P_s} \right)^{\frac{2}{k}} - \left(\frac{P_0}{P_s} \right)^{\frac{k+1}{k}} \right)^{-\frac{1}{2}} \left(\frac{2}{k} \left(\frac{1}{P_s} \right)^{\frac{2}{k}} P_0^{\left(\frac{2}{k}-1\right)} - \frac{k+1}{k} \left(\frac{1}{P_s} \right)^{\frac{k+1}{k}} P_0^{\frac{1}{k}} \right) \tag{16}$$

$$\left.\frac{\partial f(P,H)}{\partial H}\right|_{P_0,H_0} = \left(\left(\frac{P_0}{P_s} \right)^{\frac{2}{k}} - \left(\frac{P_0}{P_s} \right)^{\frac{k+1}{k}} \right)^{\frac{1}{2}} \tag{17}$$

Once the zeroth order equation is solved for equilibrium pressure profile and film thickness (P_0, H_0), the first order equation is solved to get the perturbed pressures. The perturbed pressure profile is then used to find the frequency-dependent stiffness and damping coefficients.

$$\begin{bmatrix} k_{xx} & k_{xy} \\ k_{yx} & k_{yy} \end{bmatrix} = \frac{W_0}{C} \begin{bmatrix} K_{xx} & K_{xy} \\ K_{yx} & K_{yy} \end{bmatrix} = -\frac{W_0}{C} \frac{R}{2L} \iint \begin{bmatrix} \mathrm{Re}(P_x)\cos\theta & \mathrm{Re}(P_y)\cos\theta \\ \mathrm{Re}(P_x)\sin\theta & \mathrm{Re}(P_y)\sin\theta \end{bmatrix} \quad (18)$$

and

$$\begin{bmatrix} c_{xx} & c_{xy} \\ c_{yx} & c_{yy} \end{bmatrix} = \frac{W_0}{C\omega_s} \begin{bmatrix} C_{xx} & C_{xy} \\ C_{yx} & C_{yy} \end{bmatrix} = -\frac{W_0}{C\omega_s} \frac{R}{2L} \iint \begin{bmatrix} \mathrm{Im}(P_x)\cos\theta & \mathrm{Im}(P_y)\cos\theta \\ \mathrm{Im}(P_x)\sin\theta & \mathrm{Im}(P_y)\sin\theta \end{bmatrix} \quad (19)$$

As mentioned earlier, both the zeroth order and first order equations were solved using finite volume methods with under relaxation. The grid size used for the numerical analysis was 104 in the circumferential direction and 14 in the axial. The grid independency study of the numerical method followed in the present paper was done in [4]. The convergence criteria for the pressure was $\max\left(\frac{P_{i,j}^{n+1} - P_{i,j}^{n}}{P_{i,j}^{n}}\right) \le 5\times 10^{-6}$, where n is the iteration index.

The equilibrium position of the rotor was found using orbit simulations which are detailed in [16]. For the zeroth order solution, 1-D analytical beam model developed by Kim and Park [4] is adopted to consider top foil sagging effect under pressure. The 1-D beam model uses the computational grid scheme shown in Figure 4. Note that between the elastic foundations, three computational grid points are assigned to accurately capture the effect of top foil sagging. Further details regarding this model can be found in [4]. Figure 5 shows the pressure profile obtained by numerically solving the zeroth order equation. The peaks in the pressure profile are due to hydrostatic feed lines, the highest of which corresponds to the loaded region of the bearing.

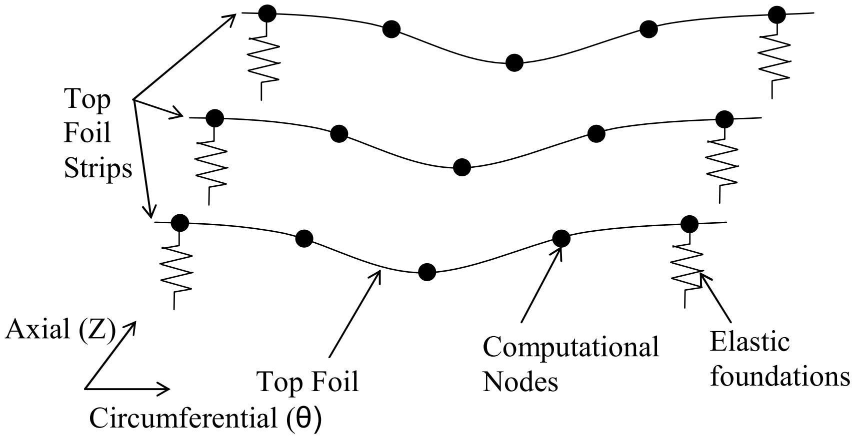

Figure 4: Grid scheme

In the first order solution, the pressure and film thickness solved in the zeroth order solution are used as inputs. The first order solution uses the same computational grid as shown in Figure 4 but the stiffness per unit area (Table 1) and corresponding equivalent damping are assigned to each computational grid point. The perturbed pressure in X-direction obtained from the first order equation is shown in Figure 6.

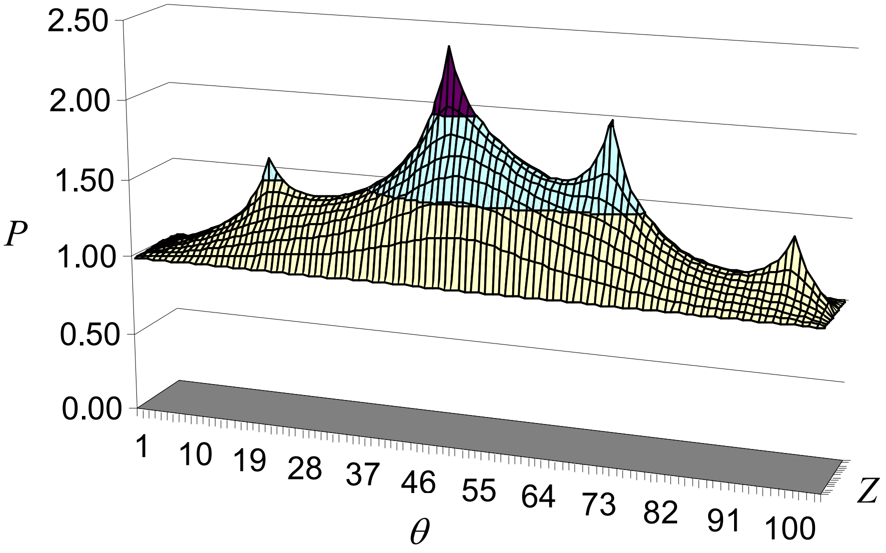

Figure 5: Zeroth order pressure profile, Λ=1.25, static load 60N

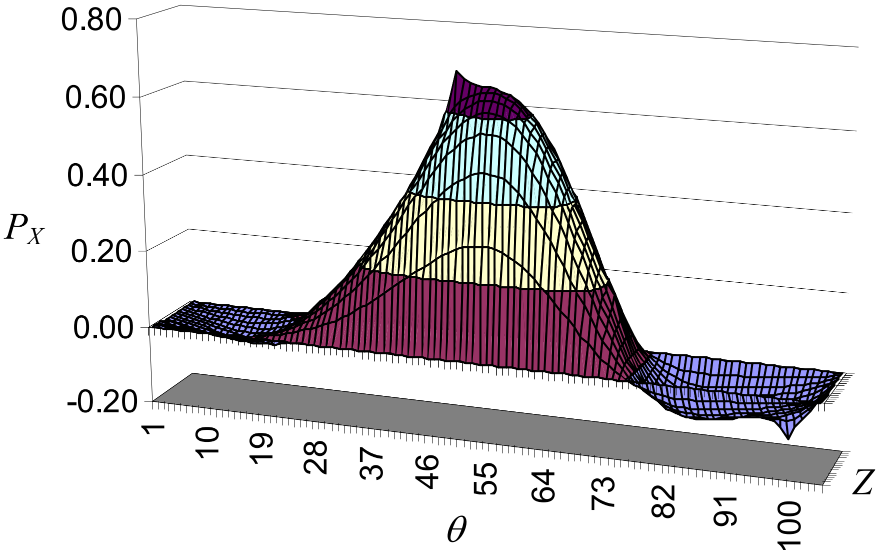

Figure 6: First order perturbed pressure profile (P_X), Λ=1.25, static load 60N

3.3 Results and discussion

The bearing stiffness and damping coefficients of HAFB were calculated with various feed parameters (Γ_s), excitation frequencies (ν), supply pressures, and bearing numbers (Λ). Note that the feed parameter and bearing number are directly proportional to the orifice diameter and rotational speed, respectively.

Firstly, effect of various feed parameters on the bearing coefficients was investigated for different supply pressures at fixed bearing number of $\Lambda = 1.25$ (rotor speed of about 30,000 rpm). For all the simulations the bearing is under a static load of 60N in X-direction (see Figure 2).

Figure 7 depicts the predicted synchronous direct stiffness coefficients versus the feed parameter. In general, the direct stiffness decreases with increase in either the feed parameter or the supply pressure. At very low feed parameters the stiffness value for all the pressures converge to a single value which corresponds to the hydrodynamic case. The decrease in stiffness with supply pressure or feed parameter can be explained from journal eccentricity and attitude angles as shown in Figure 8 and Figure 9.

Figure 9 presents the trend in attitude angle versus the feed parameter for different supply pressures. Higher supply pressure or increase in feed parameter decreases the attitude angle. At relatively high values of the supply pressure and feed parameter the attitude angle is negative. This can be attributed to the fact that with higher pressures we have more hydrostatic thrust on the rotor. Now with more thrust and with the present arrangements of the feed tubes (Figure 2), especially the 2nd tube in the direction of increasing θ, the rotor moves into the forth quadrant corresponding to θ and hence we get negative attitude angles. The small attitude angle in HAFB is very beneficial in terms of reducing cross-coupled stiffness and resultant hydrodynamic instability.

Figure 10 shows predicted synchronous cross-coupled stiffness which contributes to destabilizing forces in the gas bearings. In general, the cross-coupled stiffness decreases with supply pressure. For all pressures, stiffness values are decreasing for $\Gamma_s < 0.8$, after which they increase gradually. Figure 10 shows predicted synchronous cross-coupled stiffness which contributes to destabilizing forces in the gas bearings. In general, the cross-coupled stiffness decreases with supply pressure. For all pressures, stiffness values are decreasing for $\Gamma_s < 0.8$, after which they increase gradually.

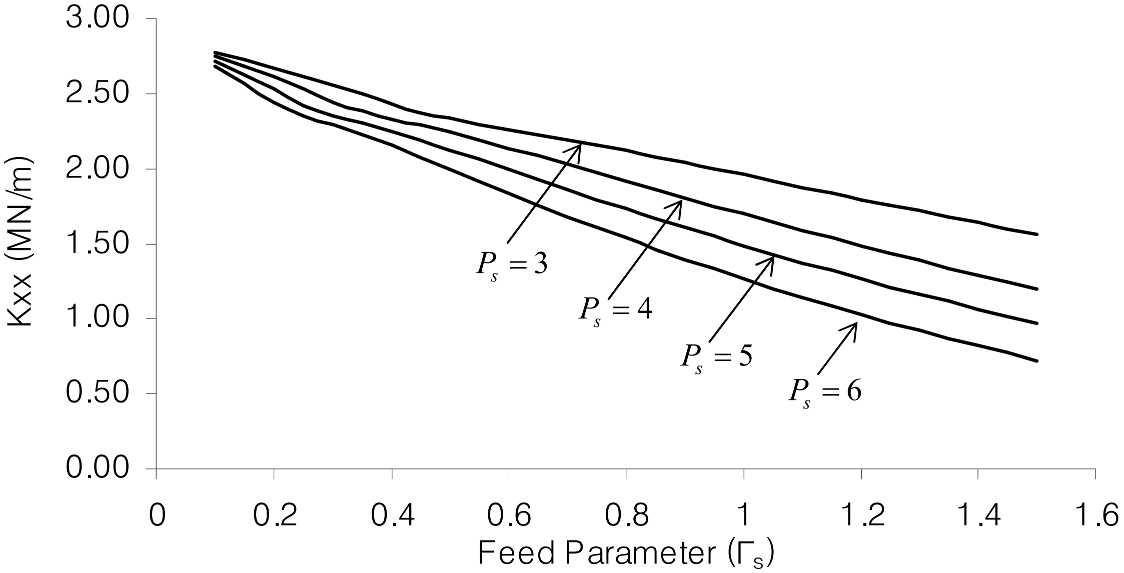

Figure 7: Predicted direct stiffness coefficients vs. feed parameter (Γ_s) with increasing supply pressure, Λ=1.25

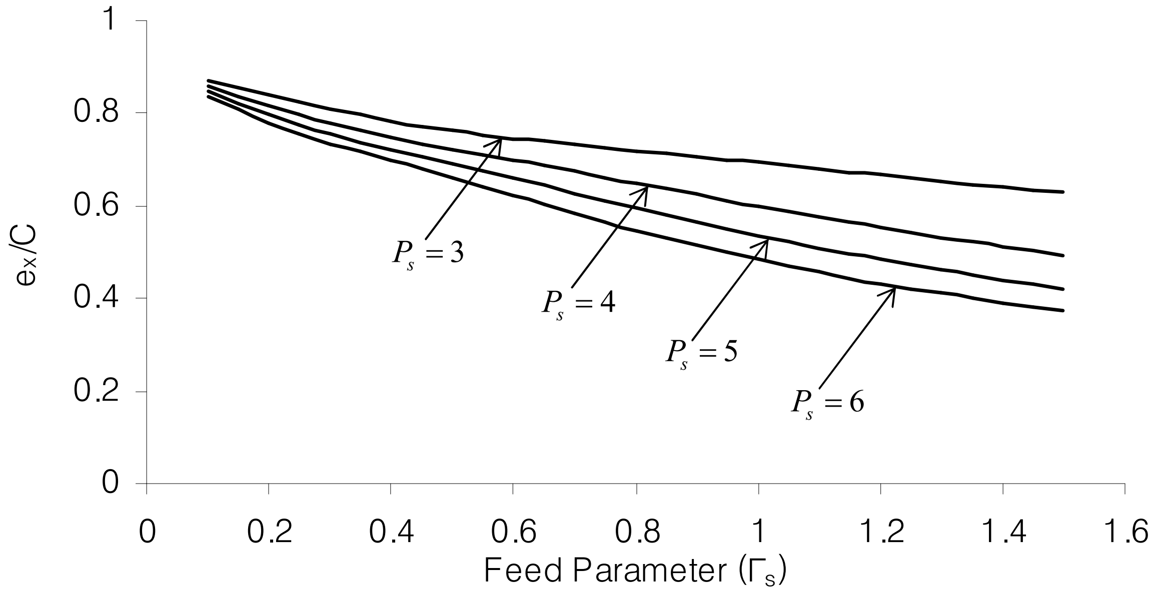

Figure 8: Predicted journal eccentricities vs. feed parameter (Γ_s) with increasing supply pressure, Λ=1.25

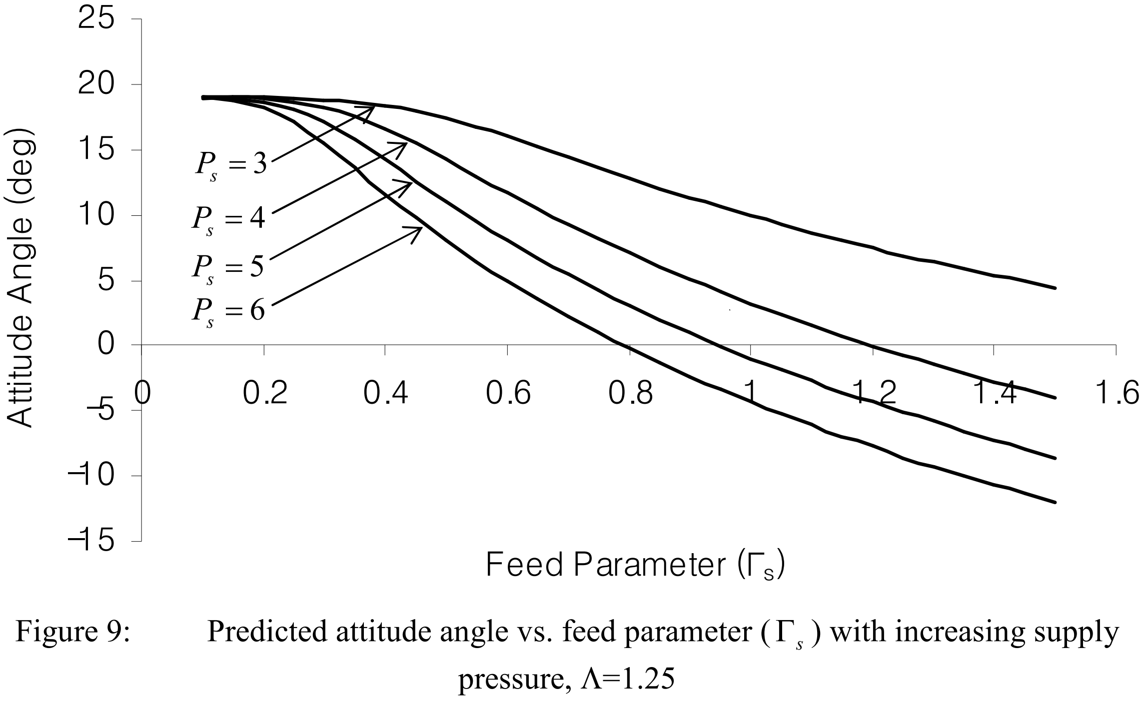

Figure 9: Predicted attitude angle vs. feed parameter (Γ_s) with increasing supply pressure, Λ=1.25

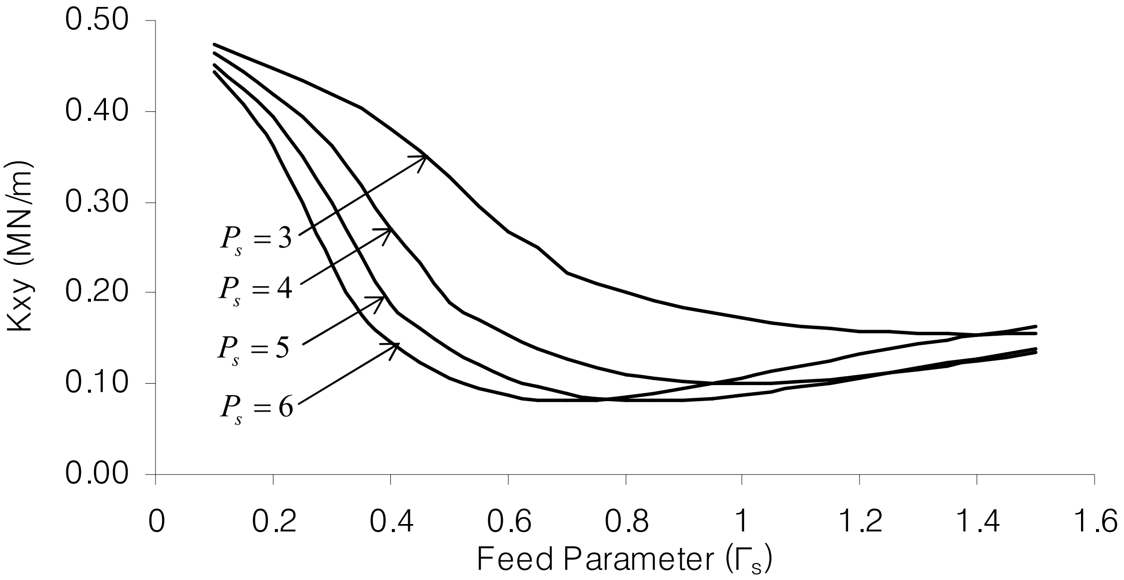

Figure 10: Predicted cross-coupled stiffness coefficients vs. feed parameter (Γ_s) with increasing supply pressure, Λ=1.25

Figure 11 and Figure 12 show the direct and cross-coupled damping coefficients, respectively. Both damping coefficients increase slightly with increase in feed parameter. The variation is not much for the direct damping coefficient, but significant for the cross-coupled damping for $\Gamma_s < 1$. The damping coefficients show a converging trend at higher feed parameters for all the supply pressures. The cross-coupled damping crosses over at $\Gamma_s = 1.2$ as shown in Figure 12. This can be attributed to the fact that higher the pressure the earlier the cross-coupled damping becomes insensitive to increasing feed parameter. The cross over happens because damping in the case of $P_s = 6$ becomes insensitive to feed parameter much earlier as compared to $P_s = 3$.

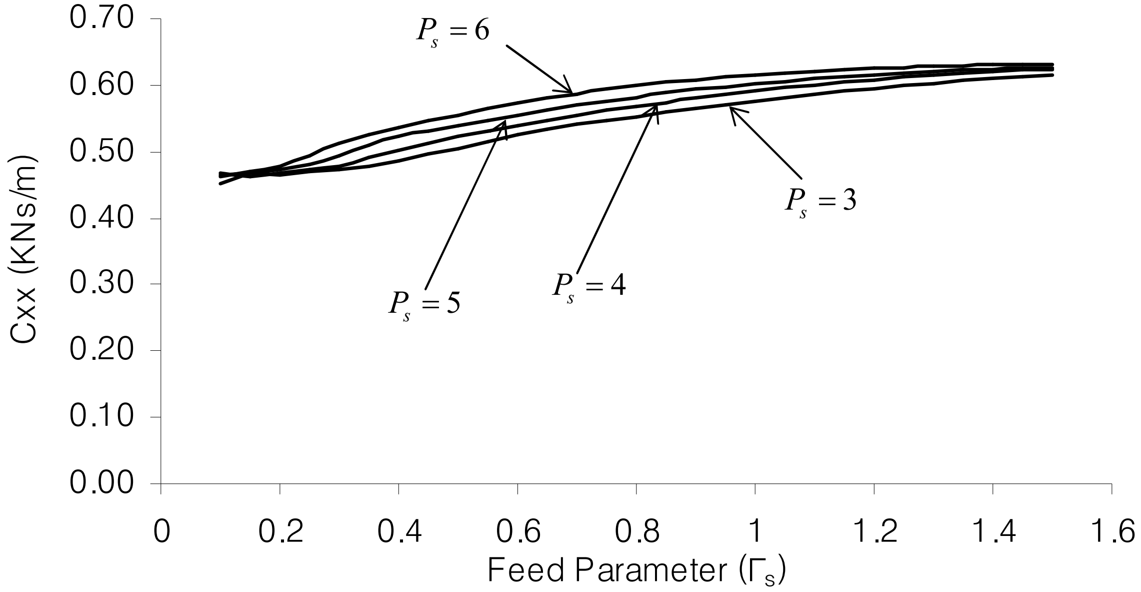

Figure 11: Predicted direct damping coefficients vs. feed parameter (Γ_s) with increasing supply pressure, Λ=1.25

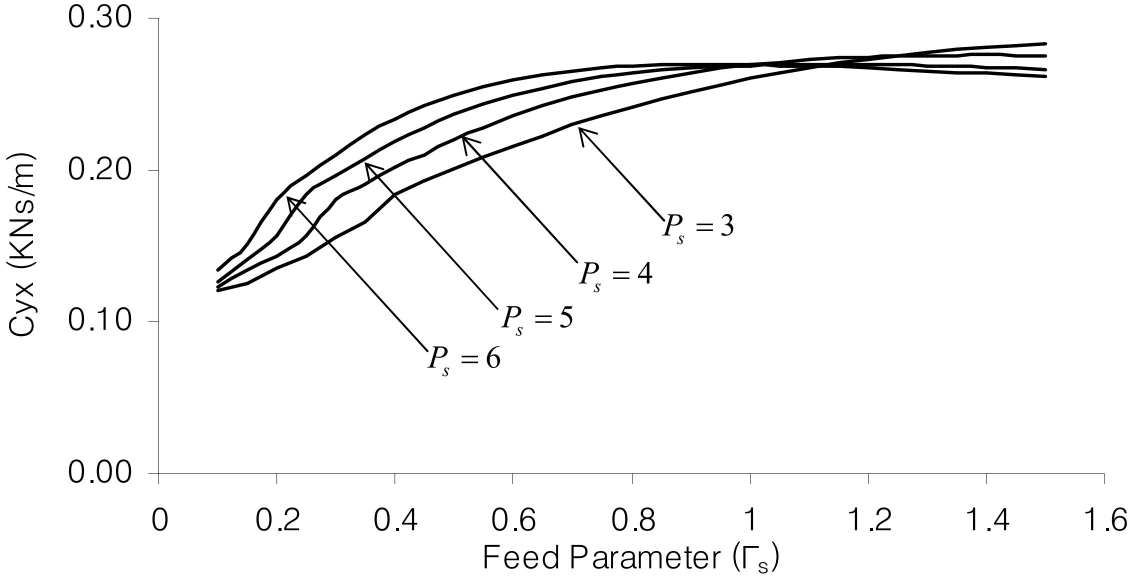

Figure 12: Predicted cross-coupled damping coefficients vs. feed parameter (Γ_s) with increasing supply pressure, Λ=1.25

Figure 13 depicts the predicted direct stiffness coefficients versus the excitation frequency ratio (ν) at increasing supply pressures. Stiffness coefficients increase for $\nu <$ 1 but show converging trend at high excitation frequency ratios. In general at low ν, lower pressures give higher stiffness values but the variation is not much with the supply pressure at higher frequencies. Cross-coupled stiffness versus ν is shown in Figure 14. The cross-coupled stiffness is rather high at ν<1 with rapid decrease with ν. However, the cross-coupled stiffness is almost independent of the ν for $\nu >$ 1.

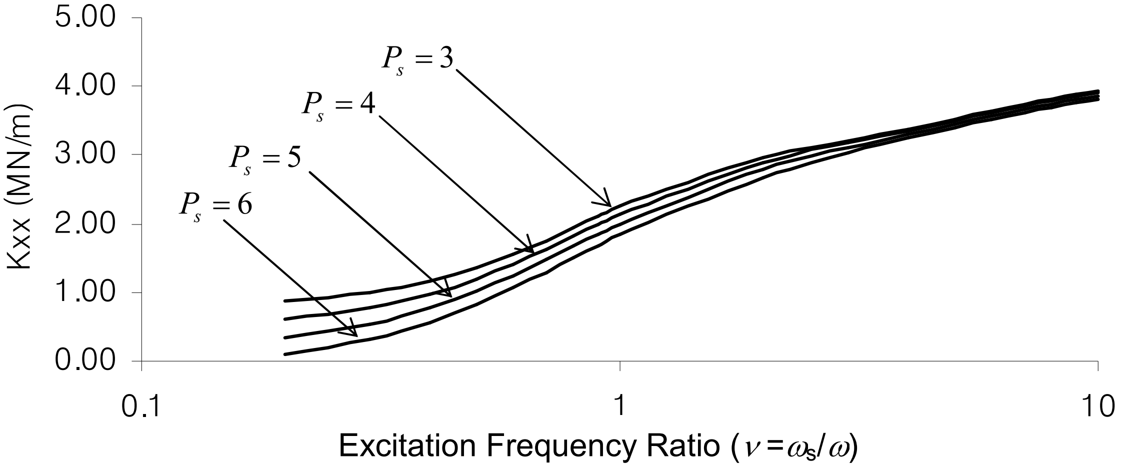

Figure 13: Predicted direct stiffness coefficients vs. excitation frequency ratio with increasing supply pressure, Λ=1.25

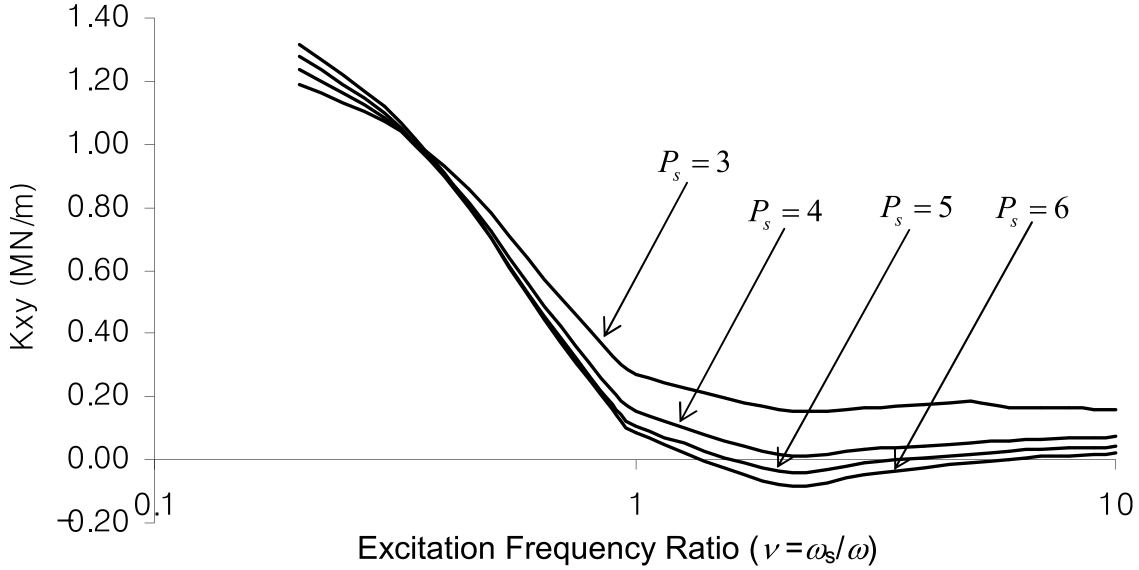

Figure 14: Predicted cross-coupled stiffness coefficients vs. excitation frequency ratio with increasing supply pressure, Λ=1.25

Frequency-dependency characteristics of direct and cross-coupled damping coefficients are shown in Figure 15 and Figure 16, respectively. Both damping coefficients show a decreasing trend with increase in ν at low ν and are almost frequency-independent at higher excitation frequencies. The damping coefficients show a converging trend towards null value at high ν. The loss of damping is accompanied by large direct stiffness coefficients at high ν (Figure 13) showing a typical hardening effect of gas bearings.

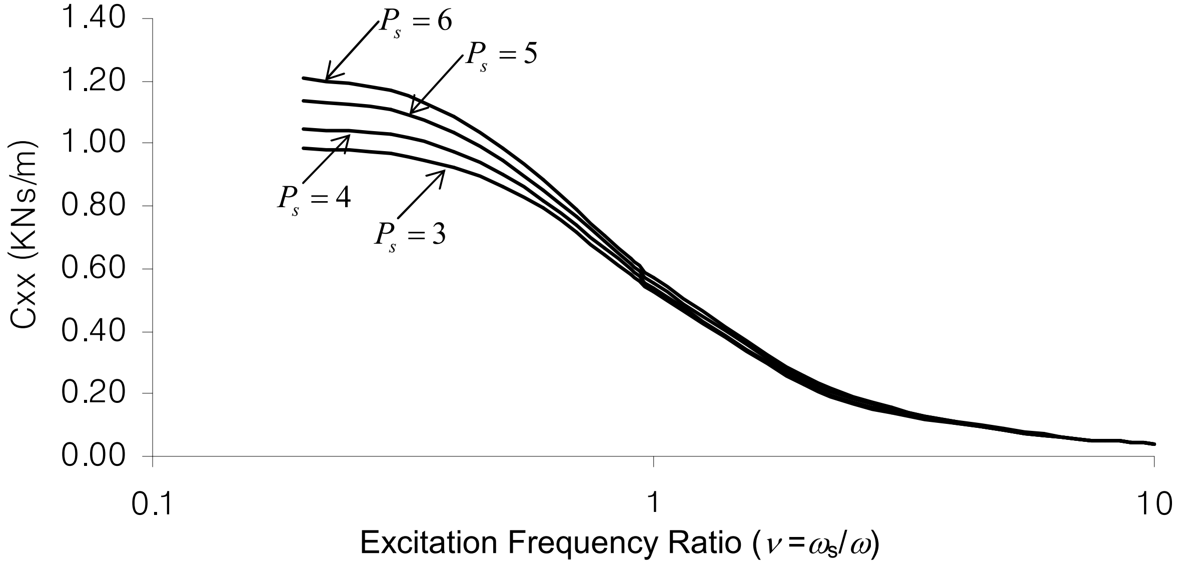

Figure 15: Predicted direct damping vs. excitation frequency ratio with increasing supply pressure, Λ=1.25

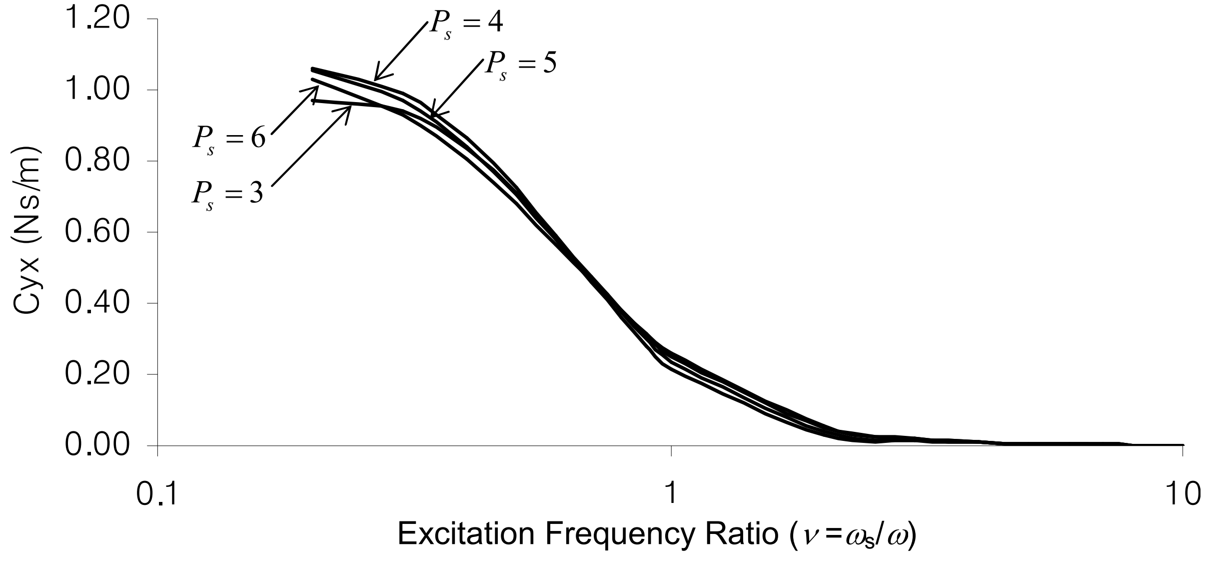

Figure 16: Predicted direct stiffness vs. excitation frequency ratio with increasing supply pressure, Λ=1.25

Figure 17 shows the predicted non-dimensional journal eccentricity versus the bearing number (Λ) for increasing supply pressures at feed parameter $\Gamma_s = 0.6$. In general, the non-dimensional eccentricity decreases with increase in either the bearing number or supply pressure. The variation in eccentricity with supply pressure is large at low bearing number (low rotational speeds). At high bearing numbers, the variation decreases and non-dimensional eccentricity shows a converging trend.

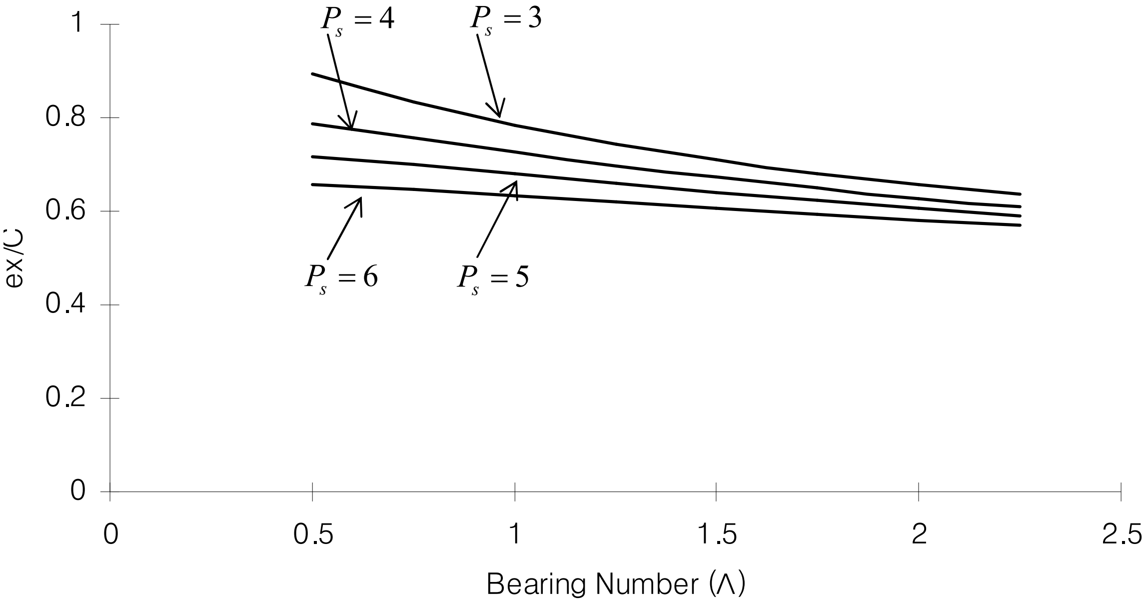

Figure 17: Predicted journal eccentricities vs. bearing number (Λ) with increasing supply pressure, Γ_s=0.6

Figure 18 and Figure 19 show the direct and cross-coupled stiffness coefficients, respectively. The direct stiffness coefficient increases rapidly at low bearing number but show converging trend at high bearing numbers. In general, lower supply pressures give higher stiffness values and this can be attributed to the fact that eccentricity increases with decreasing the supply pressure (Figure 17). Cross-coupled stiffness decreases rapidly with bearing number, and in general, higher pressures give lower cross-coupled stiffness values.

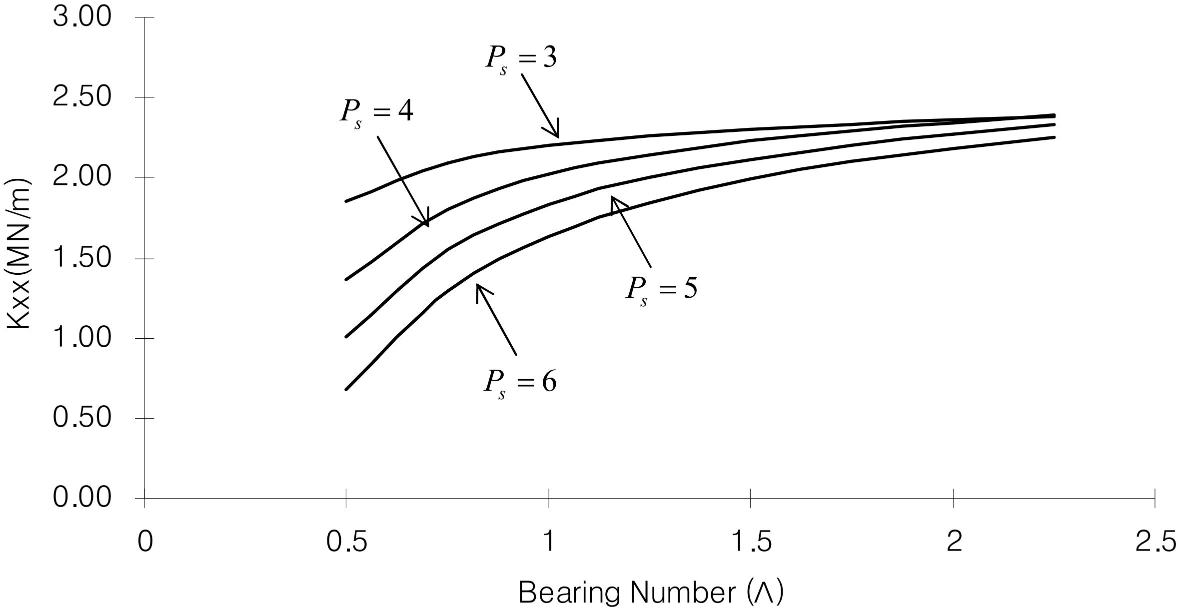

Figure 18: Predicted direct stiffness vs. bearing number (Λ) with increasing supply pressure, Γs=0.6

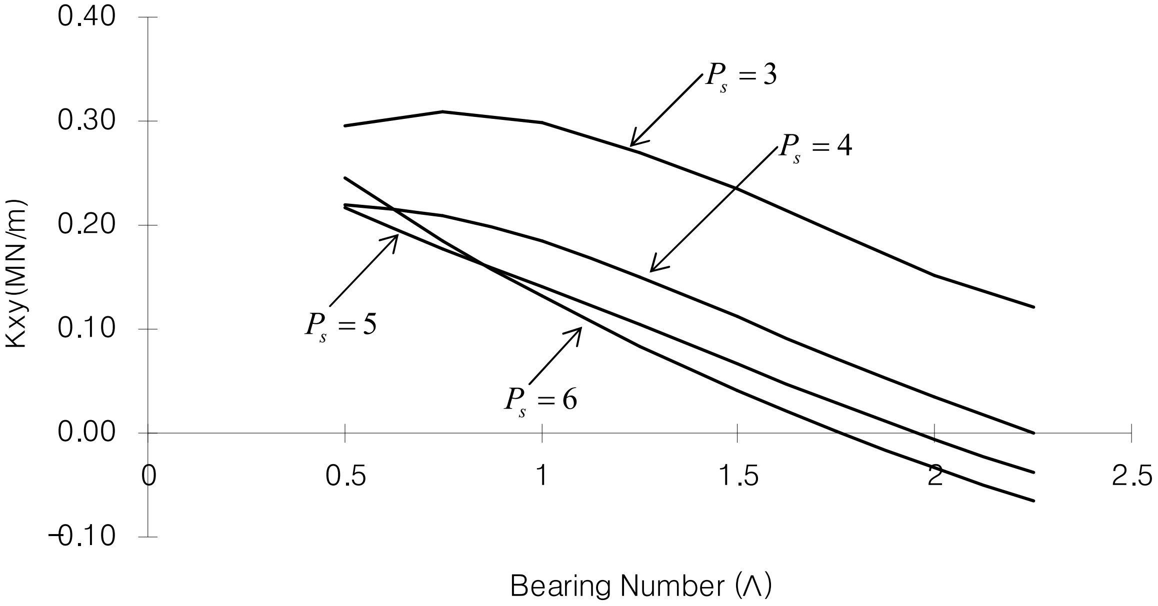

Figure 19: Predicted cross-coupled stiffness vs. bearing number (Λ) with increasing supply pressure, Γ_s=0.6

Figure 20 depicts the direct damping coefficient with increasing bearing number for various supply pressures. The direct damping coefficients decrease rapidly for $\Lambda < 1$ after which a converging trend is observed. Direct damping values are almost independent of variation in supply pressure. Cross-coupled damping (Figure 21) show similar variation with bearing number, although in this case they change with the supply pressure.

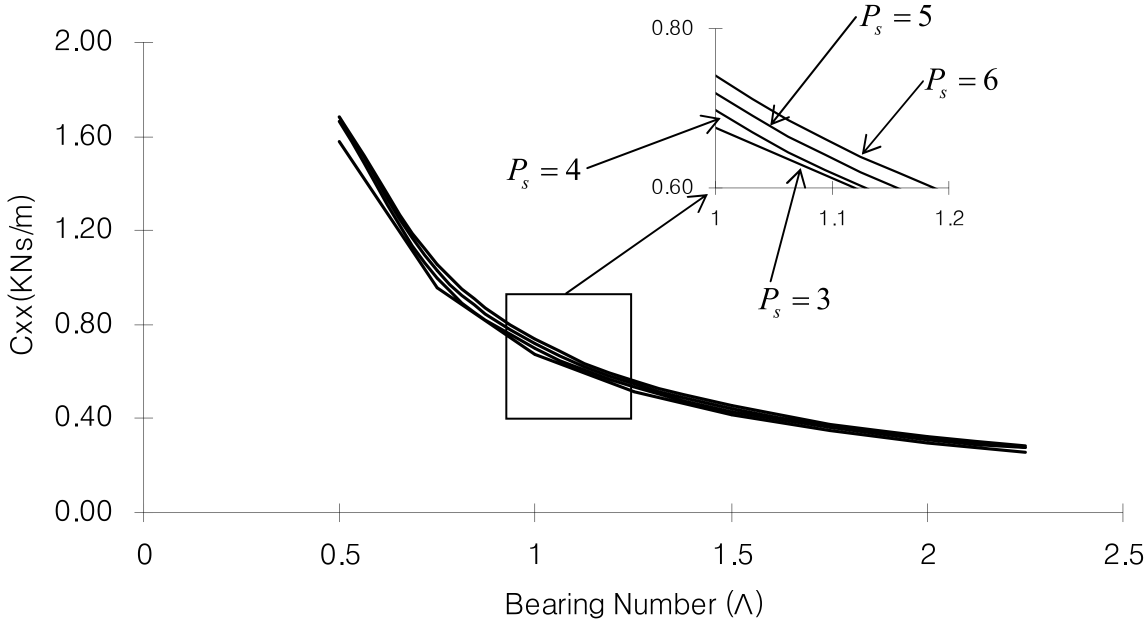

Figure 20: Predicted direct damping vs. bearing number (Λ) with increasing supply pressure, Γ_s=0.6

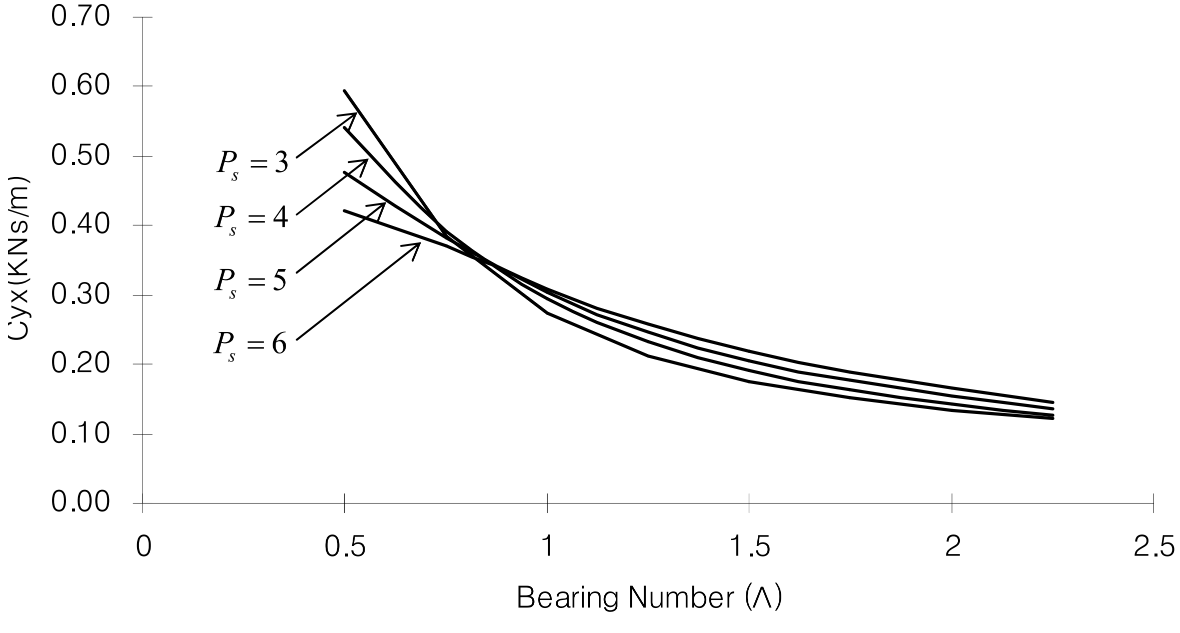

Figure 21: Predicted cross-coupled damping vs. bearing number (Λ) with increasing supply pressure, Γ_s=0.6

Benchmark results for the present analysis are included in Appendix E. There a limiting case of zero feed parameter is compared with the results by Kim [16].

4 DESIGN AND FABRICATION OF HIGH SPEED TEST RIG

The design and fabrication of a test rig which could evaluate the performance of various gas bearings at high speeds was undertaken. This section describes this unique test rig and its capabilities.

4.1 Requirements from the test tig

The basic requirement of this new test rig was to experimentally determine the capabilities of foil bearings at moderate to high speeds. The test rig was primarily envisaged to provide the capability to gather the following information

1. Load capacity of air foil bearings at various speeds
2. Thermal run way of the bearings at various speeds
3. Frictional bearing torques generated during startup, shutdown and at high speed operation.
4. Stiffness and damping coefficient of the bearings at various speeds.

Besides the experimental data that the test rig could furnish, the following features of the test rig were also desired

1. The test rig should have the capability of accommodating air foil bearings of different sizes. It is desired that in order for the test rig to test bearings of different sizes only a minimal portion of the test rig should be changed or replaced. The above requirement warrants the separation of the drive mechanism from the test section. The capability to test bearings of different sizes should be provided with the

use of appropriate adapters which can be easily attached and removed for different bearings.

2. The test rig should run on an electric motor drive. The other option besides the electric motor drive was air powered drive using impulse turbines. The later option was ruled out as it would have made the test rig extremely noisy. The air powered test rig would have also required very tight tolerances and alignments for the impulse turbines.
3. Since the test rig was designed to evaluate the thermal performance of the air bearings, the generation and transfer of parasitic heat from the driving mechanism should be minimized. The major source of heat in the electric drive train is usually the motor therefore an appropriate cooling mechanism for the motor would be required. The cooling mechanism should have the capability of using both air and water as coolant.
4. The primary function of the test rig was to measure static performance (load capacity and frictional torques) therefore the journal should be rigidly supported.
5. The test should have a loading mechanism which could provide external load to the air foil bearings.
6. Depending on the choice of support for the rotor, the support system may require appropriate lubrication, sealing and a preload mechanism.

4.2 General layout and design of the test rig

Based on the requirements listed in the previous section the author came up with a design of the test rig shown in Figure 22. Description of individual components shown in the figure is given below:

1. Electric motor: Specially fabricated 4kW electric motor, with maximum speed of 90,000 RPM.
2. Motor stator: Stator for electric motor.
3. Cooling jacket: In order to sustain such high speeds the electric motor requires cooling jacket to dissipate heat.
4. Spindle bearing. High speed spindle ball bearing with ceramic balls from GMN, Germany.
5. Bearing inserts: Inserts to support spindle bearings.
6. Housing: Aluminum housing to support rotor, motor and bearings inserts.
7. Oil jet lubrication setup: Oil jet lubrication for spindle bearings.
8. Lip seals: Hydraulic-cylinder sealing with Buna-N O-ring.
9. End plates: Plates to hold lip seals.
10. Wave spring washers – compression type: Wave springs to provide axial pre-load to spindle bearings
11. Rotor: 20mm/12” shaft.
12. Test section: Removable test section over which foil bearing is inserted.
13. Hybrid air foil bearing: Proposed hybrid air foil bearing for 1.5” shaft.
14. Foil bearing housing: Housing to hold foil bearing.

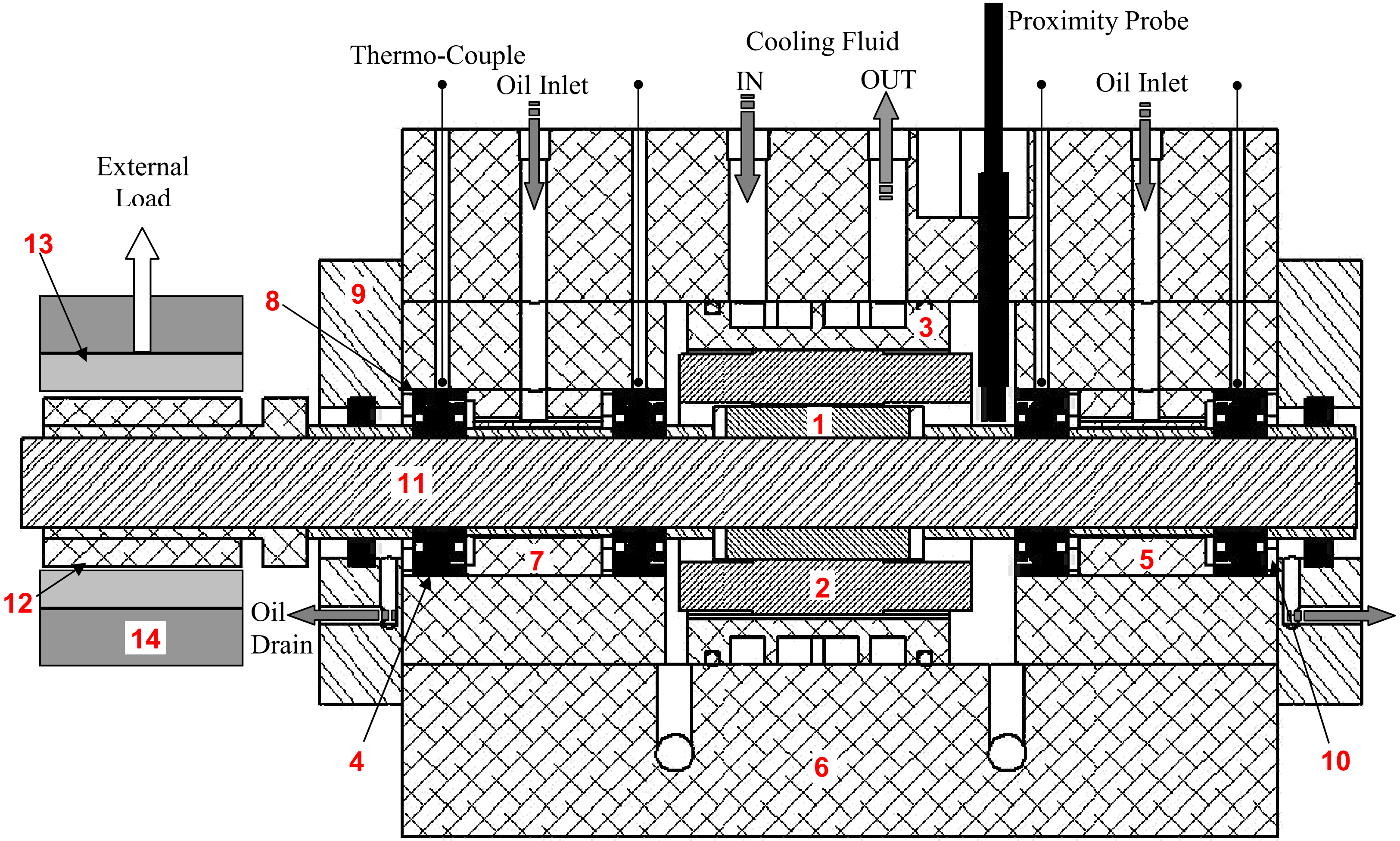

Figure 22: Test rig

4.3 Description of major test rig components

This section gives a detailed description of major components of the test rig. The rotordynamic characteristics of the spindle constructed is in the following section.

4.3.1 Spindle bearings

Given the moderate to high speed operation and rigid support requirement of the test rig, spindle bearings were used. Spindle bearings are angular contact bearings in which forces are transmitted from one raceway to other under a specific contact angle. To further increase the maximum achievable speed (limiting speed) and the service life, spindle bearings with ceramic balls were used. Spindle bearings require adjustment against a second bearing and this arrangement should be under a permanent axial load, the preload. The arrangement can either have a spring preload or rigid preload. Spring preload are suitable for high speed application and are insensitive to thermal expansion of the rotor or the bearing housing. Rigid preload though are easier to implement have lower limiting speeds as compared to spring preload. For the present test rig, bearing arrangement with spring preload was used. Spring preload was provided using wave spring washers and stainless shims were used to provide appropriate compression to these springs in order to get the required preload. The specifications and the description of ball bearing used are given in Figure 23 and Table 2. Two sets of preloaded bearings were used on either side of the motor as shown in the Figure 22. The free body diagram showing the preload forces on the bearings is shown in Figure 24.

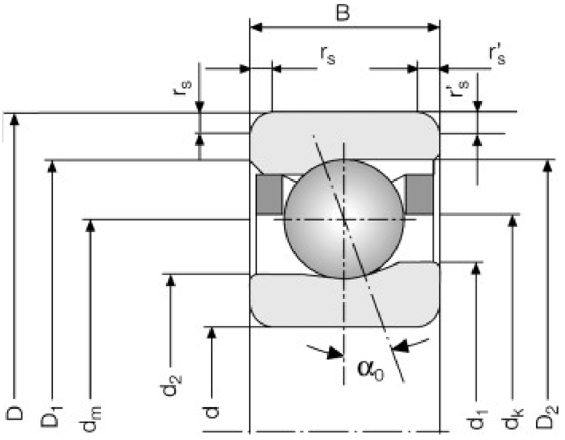

Figure 23: Spindle ball bearing, Source: GMN bearings [21]

Table 2: Spindle bearing parameters

Parameter	Value	Unit	Description
d	20	mm	Bore diameter
D	42	mm	Outer diameter
B	12	mm	Width single bearing
r_{smin}	0.6	mm	Chamfer
r'_{smin}	0.3	mm	Chamfer open side (spindle bearing)
D_w	6.35	mm	Ball diameter
Z	13	pieces	Ball complement
m	0.063	kg	Weight of bearing
d_1	26.6	mm	Outer diameter inner ring
d_2	25.4	mm	Land inner ring, open side
d_k	31.4	mm	Cage bore
d_m	31	mm	Pitch circle diameter
D_1	31.5	mm	Bore outer ring
D_2	37.3	mm	Bore outer ring (open side)
n	97500	rpm	Speed value
C	8400	N	Dynamic load rating

Table 2: Continued

Parameter	Value	Unit	Description
C_0	4150	N	Static load rating
F_v	120	N	Preload (Medium)
F_{amax}	387	N	Lift off force (Medium)
C_{ax}	37	µm	Axial rigidity (pair) (Medium)
F_f	300	mm	Minimum spring preload
α_0	15	°	Contact angle

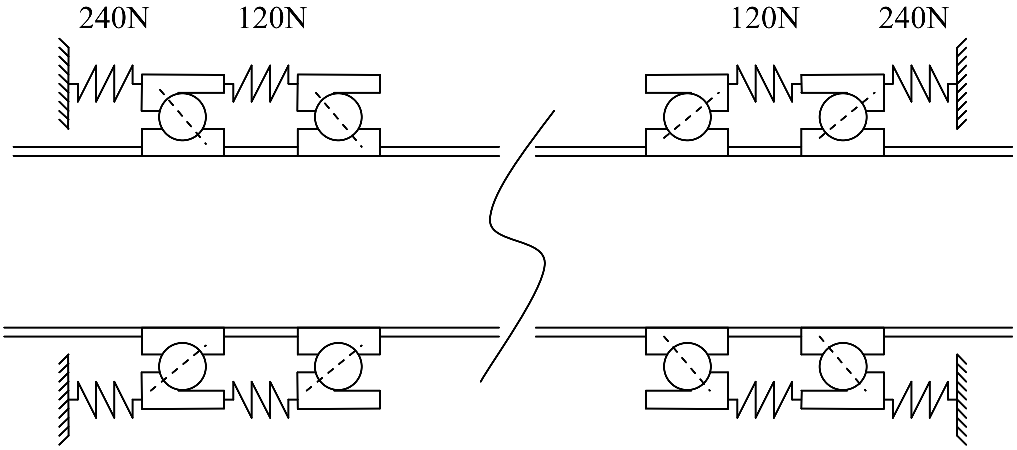

Figure 24: Bearing preload diagram

4.3.2 Test section

The test section which will be installed on the test rig is shown in Figure 25. Note the test section is a two piece assembly. The outer shell of the test section is where the air bearings will be installed. Due to numerous startups and coast-downs, the outer shell of the test section will be subject to wear. An assembly instead of a single piece test section gives the flexibility to disassemble the outer shell and have it ground and coated for lasting use. The as-built dimension of the test section (with the dimensions of the proposed bearing) should render a radial clearance of 30~40μm. It is interesting to note that with the present arrangement, the test section will act as an overhang impeller.

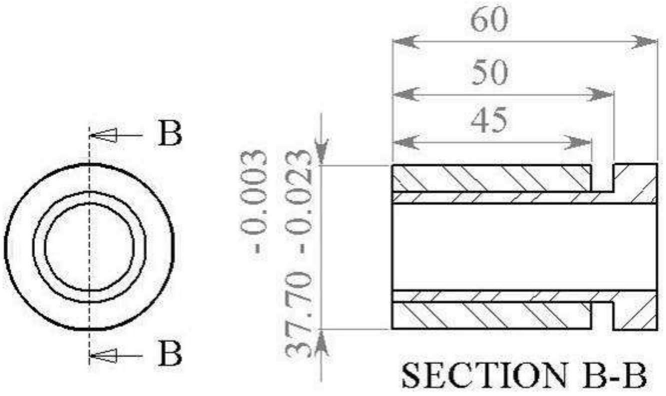

Figure 25: Test section

4.3.3 *Electric motor drive*

The description of the electric motor drive chosen for the test rig is shown in Figure 26 and Figure 27. The motor was purchased from Elektromaschinen u. Antriebe AG, Switzerland [22]. The motor is a 2-pole, asynchronous, high-speed and medium frequency motor. The motor has a wound stator and a raw rotor. Further description of the motor is given in Table 3. Because of the small size of the rotor additional balancing rings which were stacked on either side of the rotor were used for balancing. The electric motor drive requires a cooling mechanism with either water or air as a coolant. The cooling jacket designed for the present drive is shown in Figure 28. The cooling jacket has four circumferential grooves for the flow of the coolant. Clearance cuts on the top and the bottom of the jacket provide the passage of coolant from one circumferential groove to another. The cooling jacket also has grooves for the O-ring which provides sealing of the coolant.

Table 3: Electric motor drive parameters

Element		**Value**	**Units**
Motor	Speed	89,000	rpm
	Frequency	1500	Hz
	Power	2.8	kW
	Peak Power	7	kW
	Voltage	380	V
	Current	6.5	A
Stator	Insulation Class	F	–
	Maximum Permissible Heating	120	K
	Coolant Temperature	20	°C
	Coolant	Water, Air	–
Rotor	Circumferential Speed	164.9	m/s
	Material of Squirrel Cage	Copper, Ring enforced	–
	Material of Shaft	Magnetic	

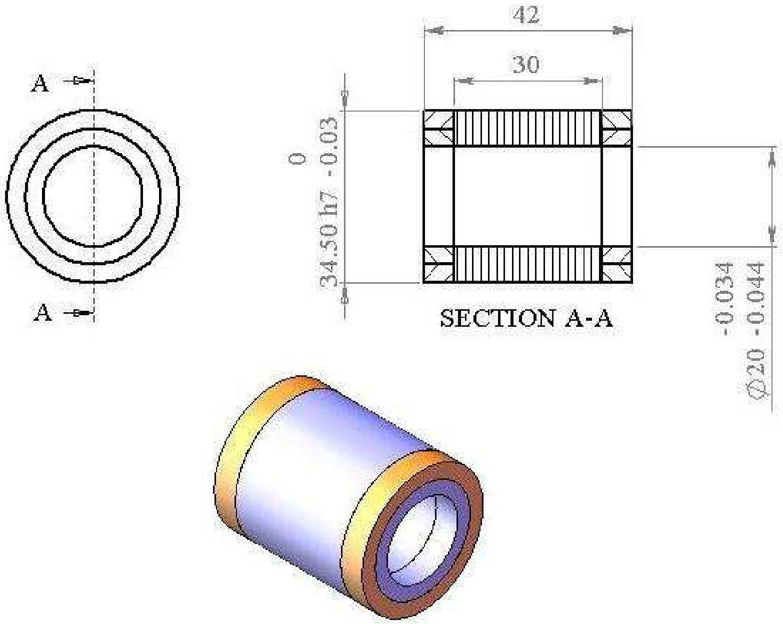

Figure 26: Electric motor drive - Motor

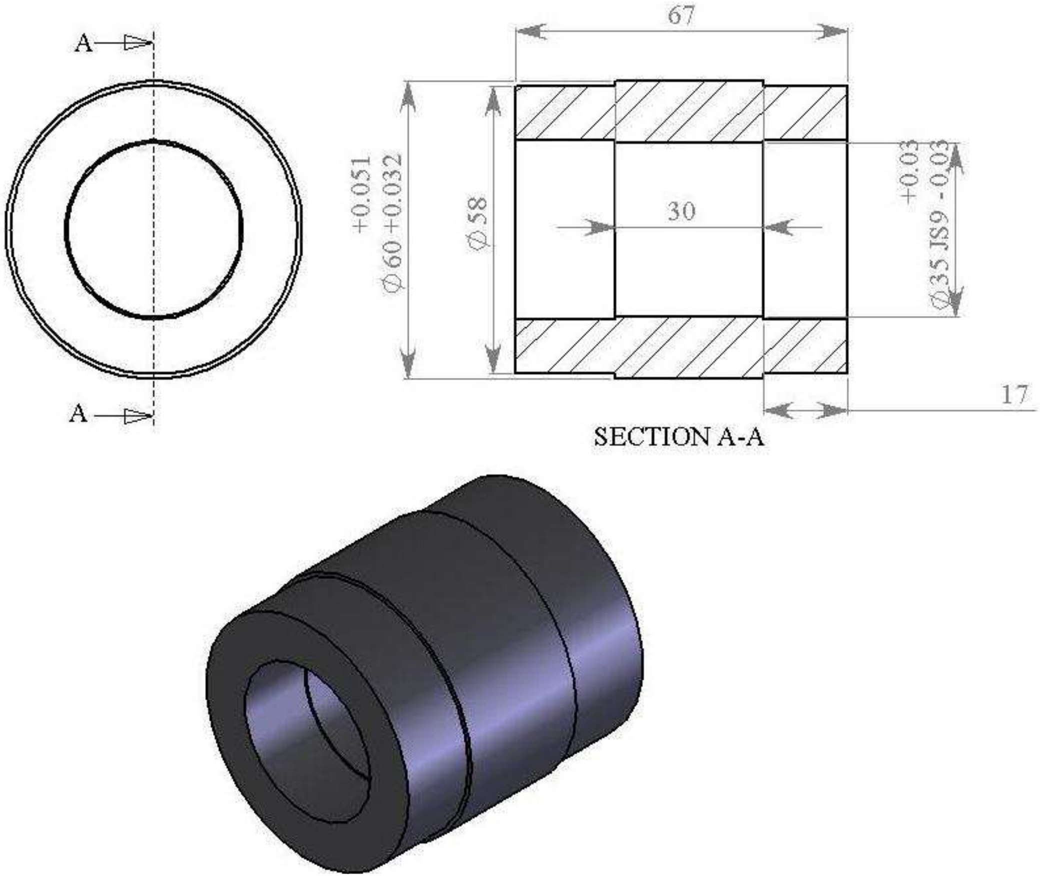

Figure 27: Electric motor drive – Stator

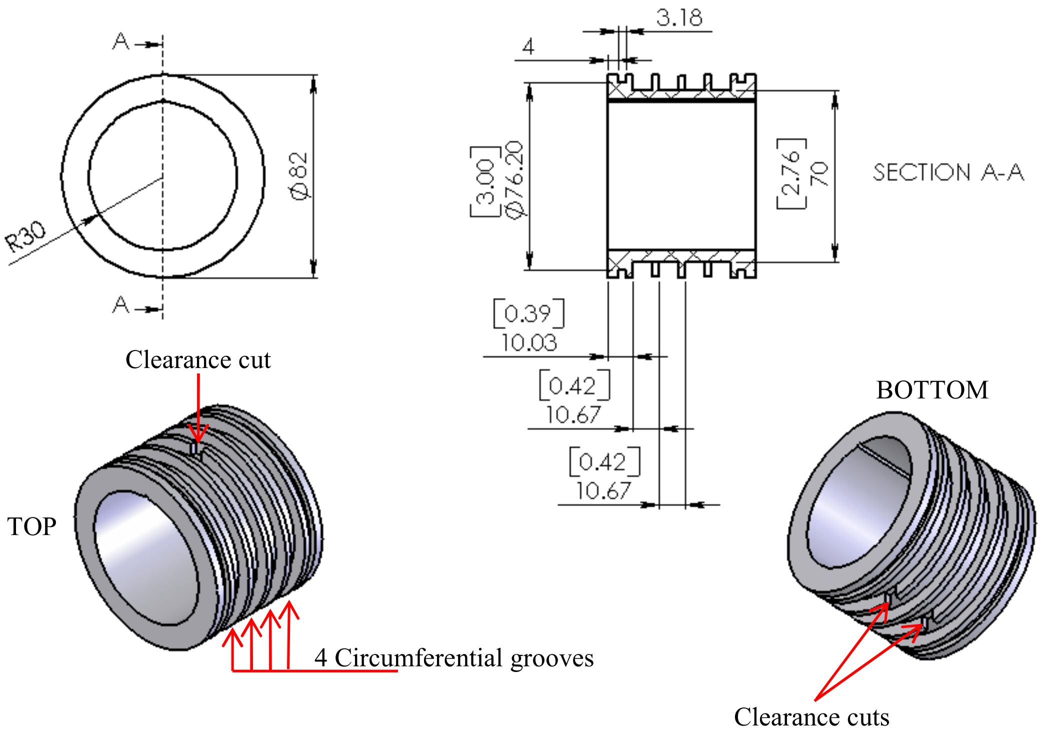

Figure 28: Electric motor drive - Cooling jacket

4.4 Rotordynamic analysis of the rotor

Lateral vibrational analysis of the rotor was done to compute critical speeds, mode shapes and undamped critical speed maps. Two methods were used for this analysis. The first method involved transfer matrices and the second was based on Finite Element Methods (FEM). Since the rotor is supported on rigid ball bearings and there is no external damping the analysis was done considering undamped conditions. Note, because there is clearance between the lip-seal and the rotor any stiffness and damping associated with the seals was not considered. Both the above mentioned methods require the shaft to be modeled as series of lumped masses and flexible mass-less beams. The rotor model and the rotor of the present test rig are shown in Figure 29. The model is made of 39 stations with bearing at stations 12, 18, 29 and 35. With the present arrangement of the rotor, the test section can be thought of as an overhang impeller and the motor as an impeller within the bearing span.

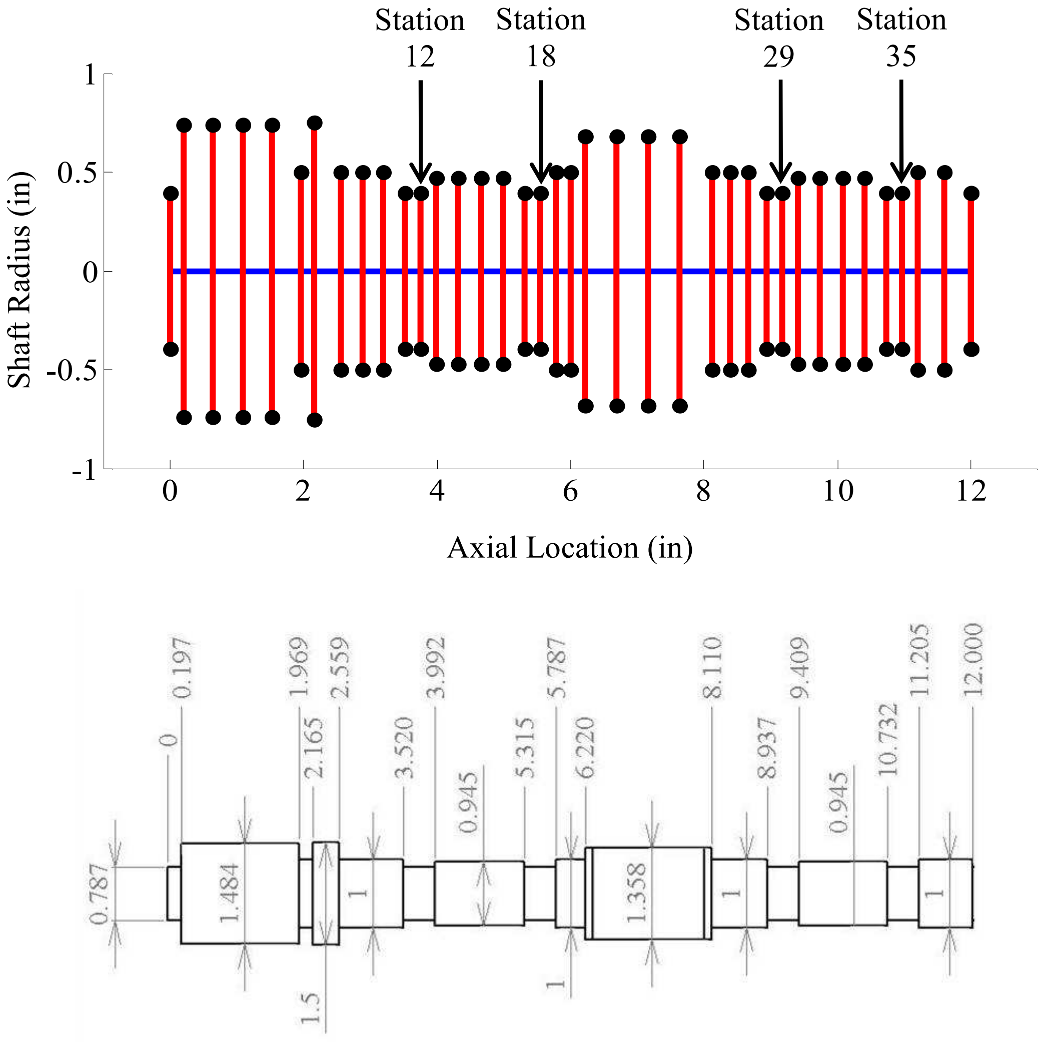

Figure 29: Rotor model and rotor

Using FEM the undamped critical speed maps of the rotor is shown in Figure 30. The map shows the natural frequencies at a given operating speed with varying support stiffness. The map is generated for the maximum continuous operating speed (MCOS) of 50,000 rpm. Note the above MCOS is when the test rig is running without oil mist lubrication and the ball bearings have only grease lubrication. The MCOS under oil-mist lubrication will be much higher. The modes shown in the map are all forward modes.

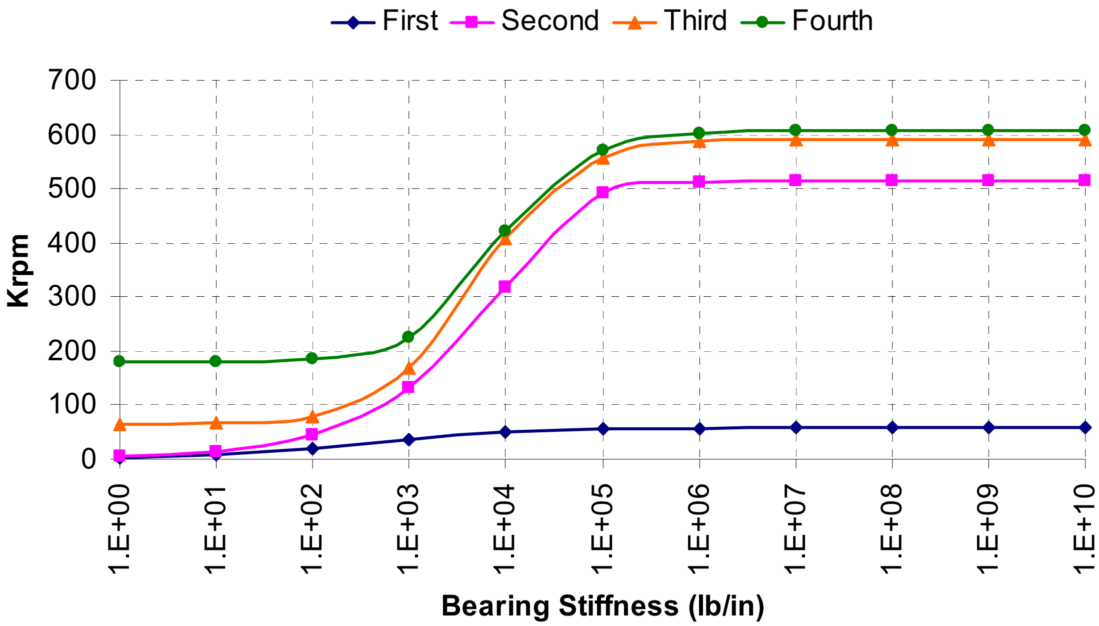

Figure 30: Undamped critical speed map at MCOS = 50,000 RPM

Note, the only mode that appear within the operating range (0~90,000 rpm) of the test rig is the first mode. It is interesting to note that the natural frequencies for all the modes are insensitive to high bearing stiffness values (>1e6 lb/in). Since the shaft has a rigid support from the ball bearings, therefore considering the higher bearing stiffness values (1e6 ~ 1e10 lb/in) in the critical speed map the first mode natural frequency is around 57,000 rpm. Figure 31 depicts the critical speed estimation of the shaft at ball bearing stiffness of ~1e6 lb/in [21]. The figure shows the backward and forward natural frequency of the shaft at various operating speeds. The critical speed by definition is the speed at which the spin frequency coincides with the natural frequency. Hence the intersection of spin = natural frequency line with the natural frequency curves are the critical speeds as shown in the figure. The critical speed from the transfer matrix function method was also calculated, the results obtained from both the methods is shown in Table 4. Note, there is a very good agreement between the two methods in the prediction of critical speeds.

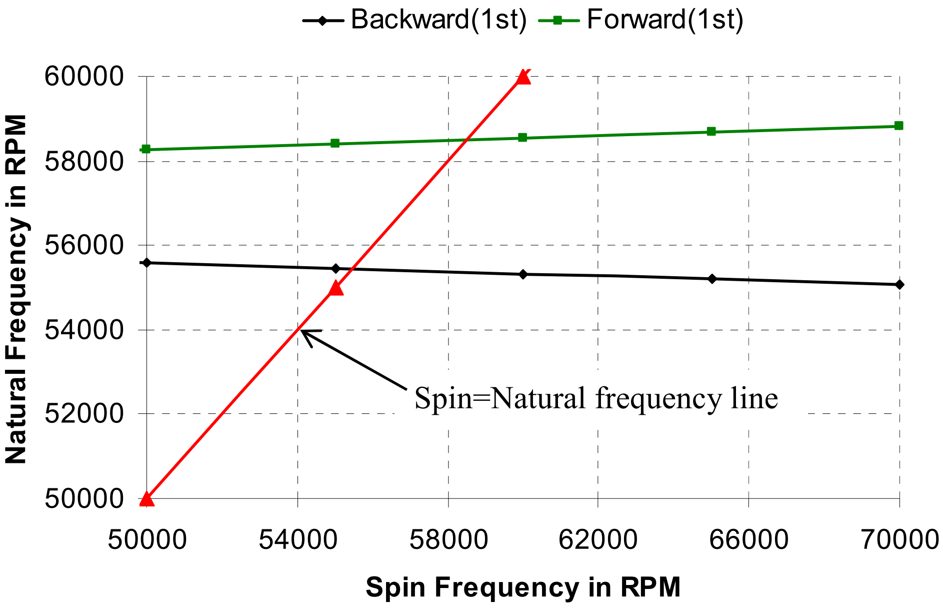

Figure 31: Critical speed estimation

Table 4: Critical speeds

Mode	Whirl Direction	Critical Speed FEM (RPM)	Critical Speed Transfer Matrix (RPM)
1st	Backward	55375	55362
1st	Forward	58375	58402

The mode shape at the above forward critical speeds is shown in Figure 32. Again we see good agreement in the results from the two methods as shown in Figure 32 (b).

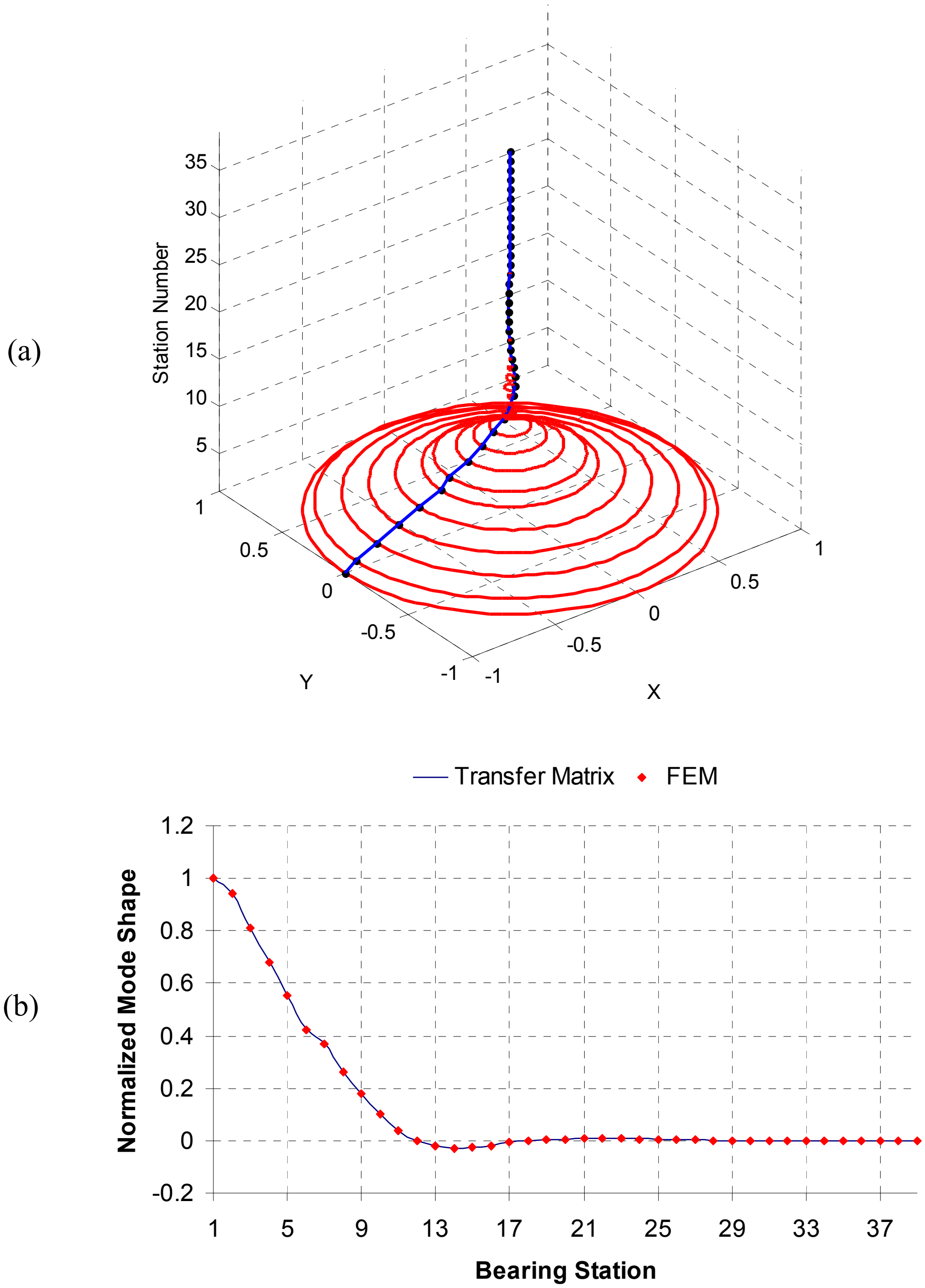

Figure 32: Mode shape plots

4.5 Commissioning of test rig

The commissioning of the test rig was conducted after the assembly of all the parts excluding the test section. The test section was not assembled as its assembly would have precluded the possibility of increasing the preload on the ball bearings located near the test section (see Figure 22). To monitor the health of the test rig thermocouples where attached on the outer races of three of the four ball bearings to monitor their temperature. The outer race of the fourth bearing was inaccessible because of the electrical connection box installed on the test rig housing for the power supply of the motor. The temperature of the motor was monitored through a thermistor which was factory installed in the stator element of the motor. The installed thermistor was of positive temperature coefficient (PTC) type and the threshold resistance value which corresponds to maximum operating temperature of motor was 3990 Ω. The calibration chart of the thermistor is shown in Appendix C. The maximum allowable operating temperature of the bearings is limited by the retaining cages that hold the balls in place within the outer and the inner race and for the present case was 120°C [21]. For the preliminary commissioning of the test rig, only grease lubrication in the ball bearings and only air as the coolant for the motor was used. Figure 33 show the commissioning report of the test rig at 30,000 and 40,000 RPM. During the tests bearing temperatures and motor resistance was monitored after every 2 minutes. The data was collected until saturation in the bearing temperature was seen. Note the irregularity in the resistance values obtained during the two tests can be attributed to the highly non-linear nature of the thermistor.

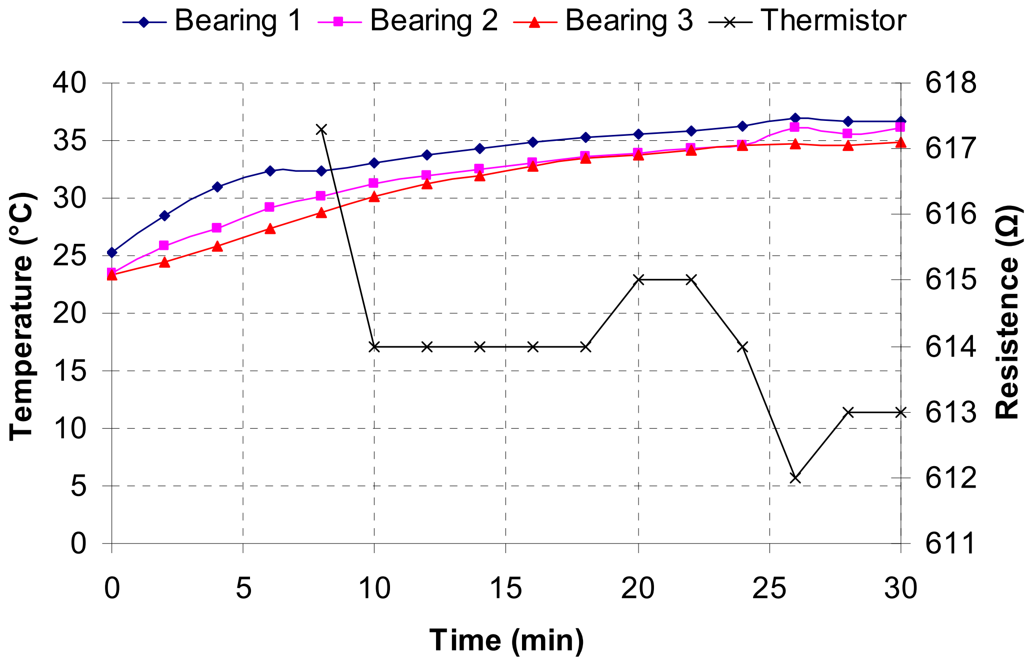

(a) Commissioning at 30,000 RPM

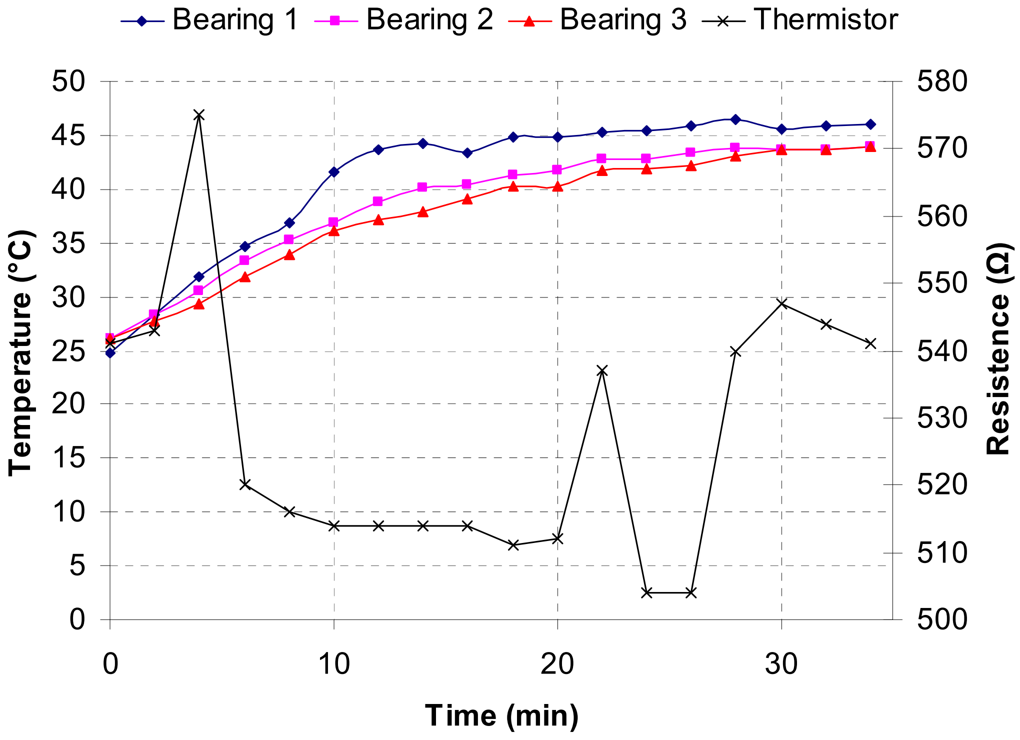

(b) Commissioning at 40,000 RPM

Figure 33: Commissioning of test rig

To determine the possibility of shaft bow and quantify it at the location of test section, proximity sensor was installed as shown in Figure 34. The sensor was installed on a manual linear stage equipped with a vernier micrometer. The proximity probe was first calibrated, see Appendix D for the calibration chart.

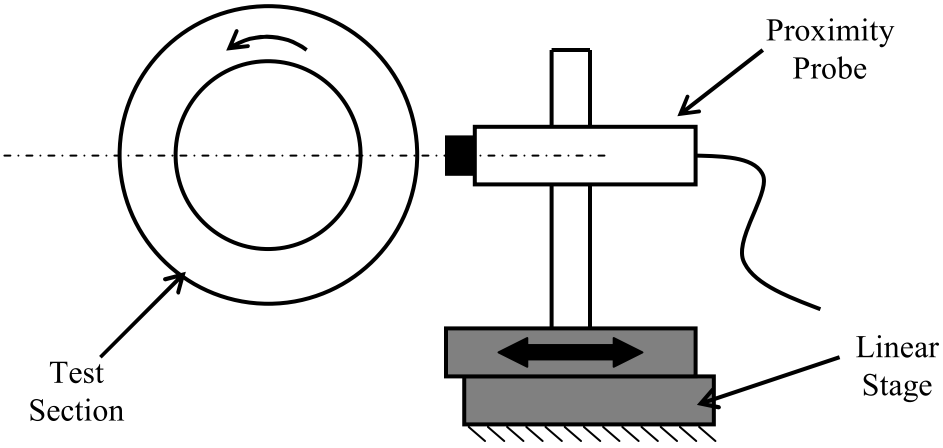

Figure 34: Proximity probe arrangement

The shaft was rotated by hand to examine the maximum and the minimum voltage output from the proximity probe. The angular separation between the points that gave these voltages was close to 180°. Furthermore using the voltage difference between these points and the calibration chart the displacement was estimated as 20µm. This displacement is the peak to peak displacement due to the shaft bow. Note, the zero to peak displacement of shaft of 10µm is considerably high given the nominal clearance of the bearing is just 25µm. Next, the level of vibrations at various operating speeds was acquired using a data acquisition program developed in LabView. The FFT data obtained for 4 different speeds are shown in Figure 35 and Figure 36.

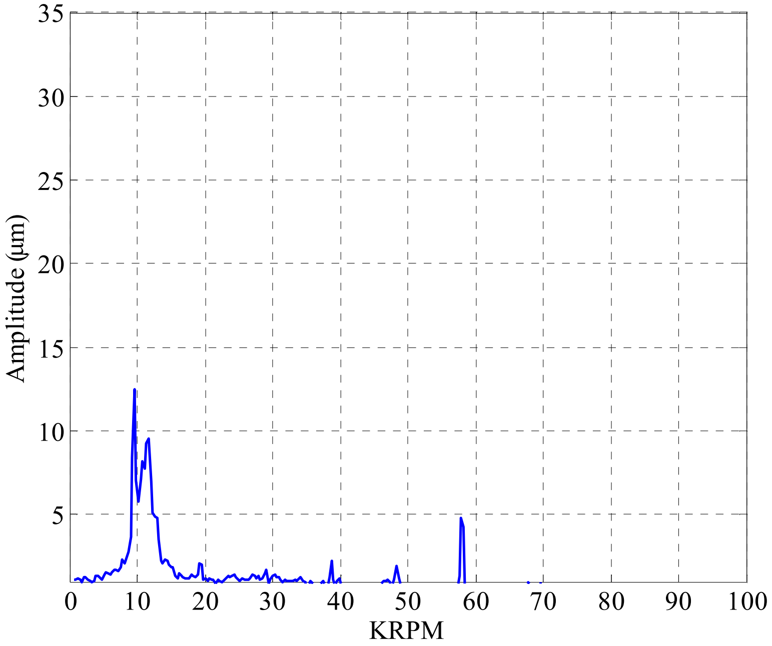

(a) Operating Speed: 10,000 RPM

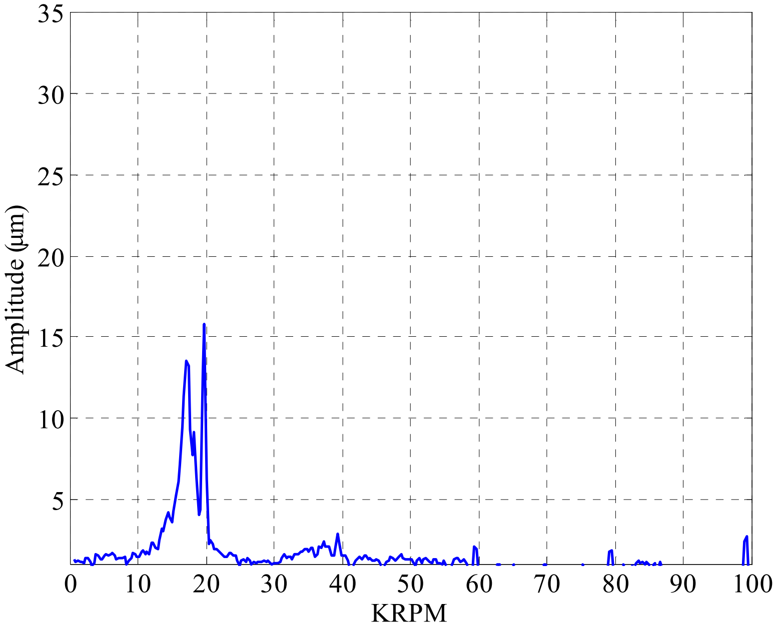

(b) Operating Speed: 20,000 RPM

Figure 35: FFT at 10,000 and 20,000 RPM

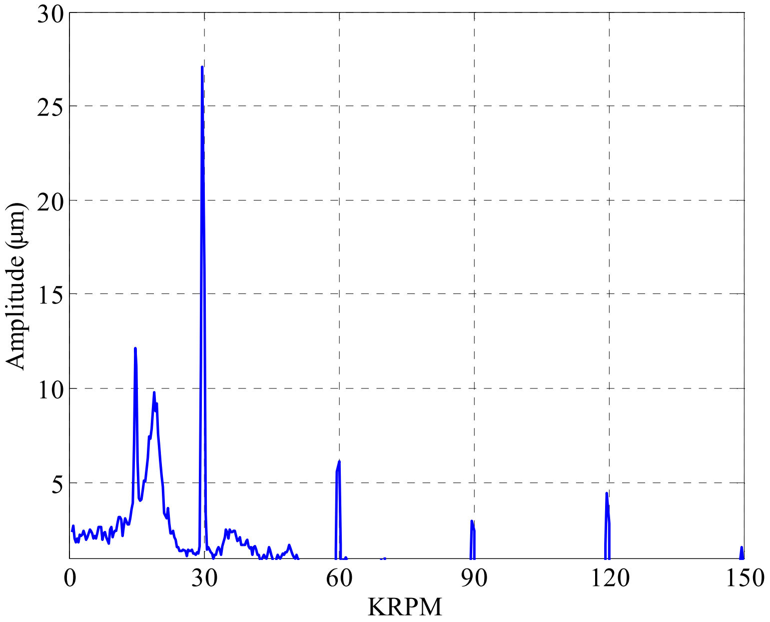

(a) Operating Speed: 30,000 RPM

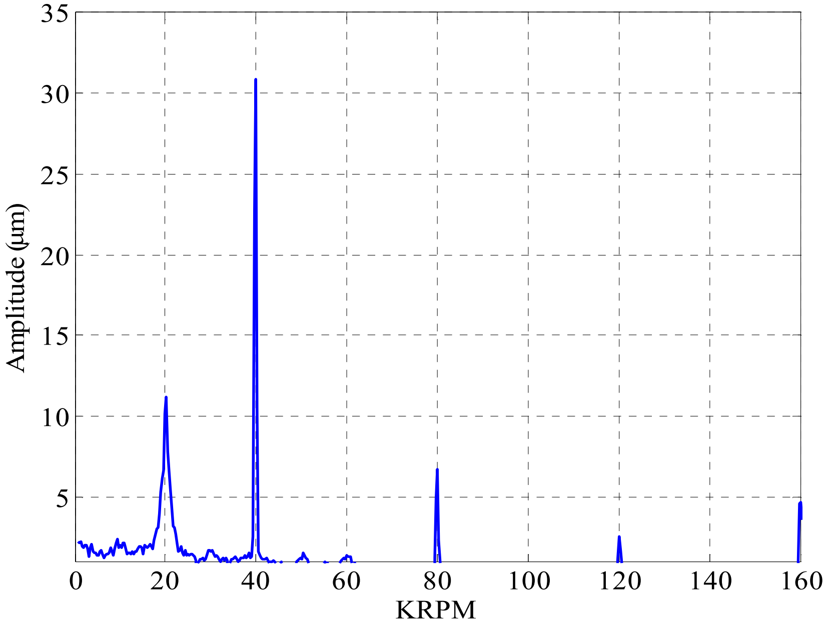

(a) Operating Speed: 40,000 RPM

Figure 36: FFT at 30,000 and 40,000 RPM

The significant bow in the shaft can be attributed to the rather cold mounting of the rotor element of the motor on to the shaft. The cold mounting had to be performed as there was limitation on the maximum temperature (300°C) up to which the rotor element could be heated. According to the motor vendor, the limitation was due to the windings inside the rotor element. All the others parts e.g. shaft sleeves, were press fitted at temperature of around 500°C.

The shaft bow was rectified by grinding the test section at slow roll. The grinding operation is depicted in Figure 37. The shaft was rotated from the non-test section end of the test rig, as shown, to nullify the shaft bow at the test section. The grinding wheel was traversed over the whole span of the test section.

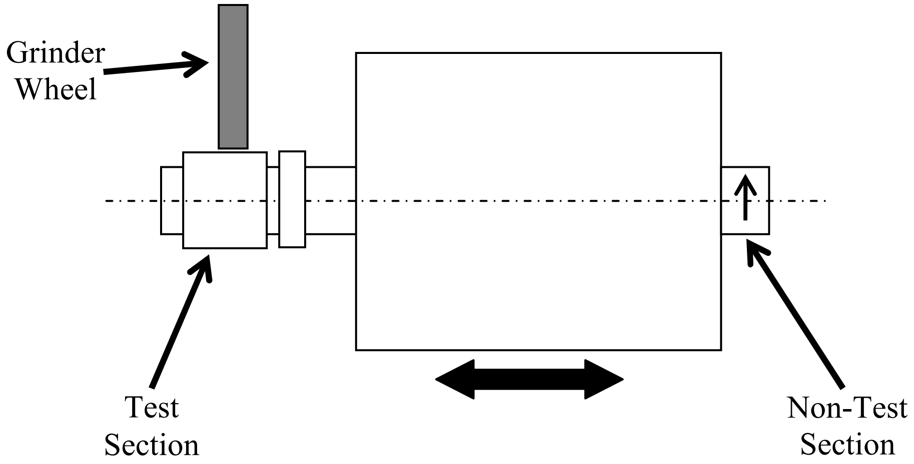

Figure 37: Grinding of test section

5 EXPERIMENTAL RESULTS

The present section describes the experimental results acquired using the newly fabricated test rig and the developed HAFB. A detailed overview of the HAB, experimental setup and the data acquisition apparatus is also included. Appendix F includes the fabrication of bump foil and top foil for the HAFB.

5.1 Description of prototype HAFB

The HAFB as described earlier has four steel feed tubes (OD: 0.05"/ ID: 0.038") for external pressurization (see Figure 38 (a)). The steel tubes are connected to the surface of the top-foil using silicone rubber tubing (OD: 0.065"/ ID: 0.03") as shown in Figure 38 (a). The rubber tubing provides flexibility and is easier to glue on to the curved surface of the top foil. For the load capacity measurements of the HAFB, a thermocouple is glued using epoxy to the back side of the top foil as shown in Figure 38 (b). Note, the location of the thermocouple is exactly opposite to the leading edge and is downstream of the second feed tube in the direction of rotation. Bearing parameters before and after removal of shaft bow is shown in Table 5.

Table 5: Prototype bearing parameters

Parameters	Value
Bearing diameter, $2R$	$1.5365^{+0.0001}_{-0.0001}$ inch
Bearing axial length, L	$1.5365^{+0.001}_{-0.001}$ inch
Nominal clearance, C (Before correction of shaft bow)	$0.002^{+0.0001}_{-0.0001}$ inch
Nominal clearance, C (After correction of shaft bow)	$0.003^{+0.0001}_{-0.0001}$ inch
Bump stiffness per unit area	4.7 GN/m^3
Top foil thickness	0.004 inch
Bump Foil Height	0.02 inch

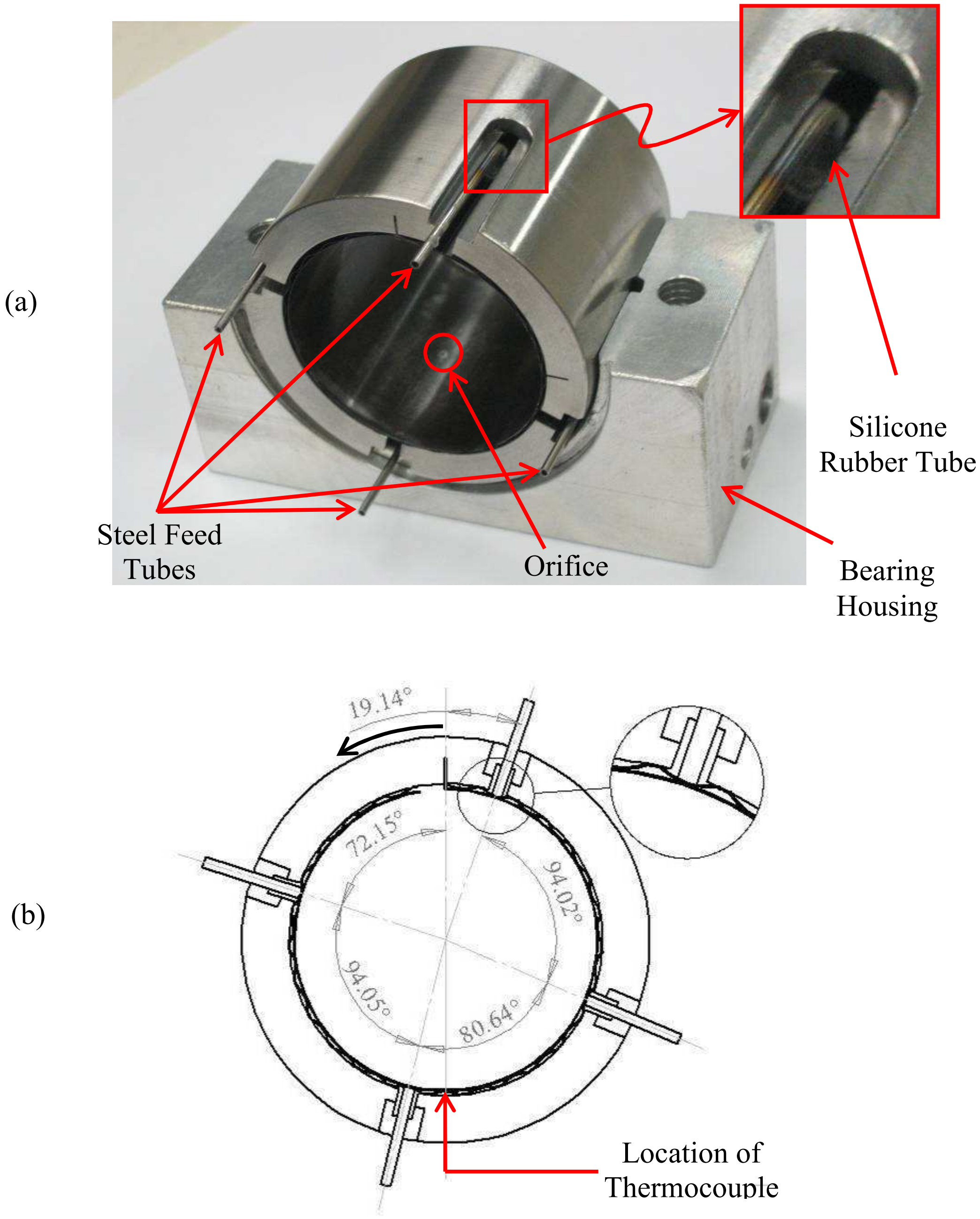

Figure 38: Hybrid air foil bearing (HAFB)

5.2 Experimental setup

The experimental setup of the test is shown in Figure 39(a). The load is applied to the bearing using a pulley system. A schematic depicting the loading mechanism is shown in Figure 39(b). The present arrangement of the load mechanism ensures that the load is applied evenly over the axial span of the bearing. The air flow to the bearing feed tubes is regulated using an acrylic panel mount flow meter and the supply pressure is measured through an air pressure gauge. The temperature data is read through a thermocouple display which is connected to the computer for data logging.

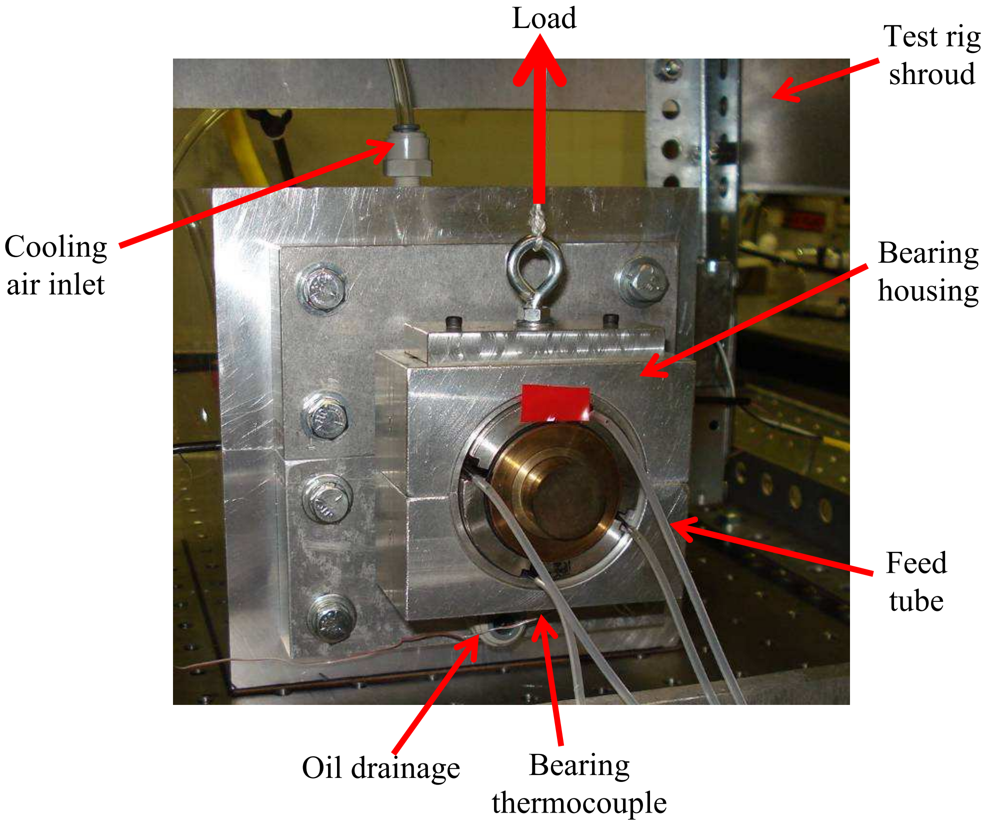

Figure 39: Test facility

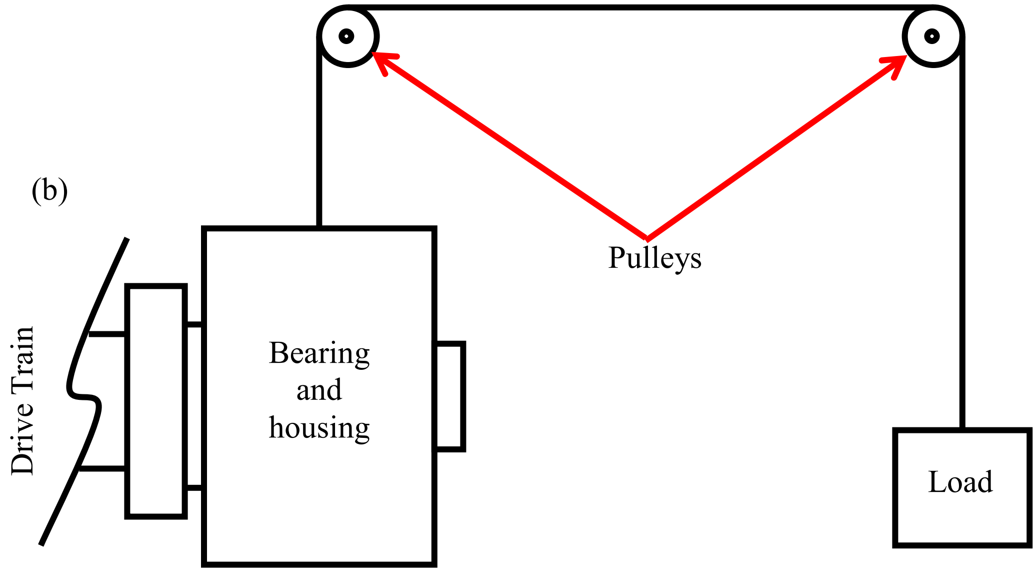

Figure 39: Continued

5.3 Test results

Several tests were performed to determine the load carrying capacity of HAFB at various operating speeds. The test conditions, observations and results from load capacity tests at each speed follows.

5.3.1 Test 1

The first test conducted on the prototype HAFB was with the bow in the shaft (see section 4.5). All the other operating conditions are summarized in Table 6. To determine the load carrying capacity of the bearing in the present case increasing loads was applied to the bearing and within each load application the temperature was allowed to stabilize (Figure 40). As reported by Kim and Park [4] the threshold where the bearing reaches the load capacity there should be a sharp increase in temperature. This sharp increase in temperature either corresponds to rotor rubbing on the top foil surface or the thermal runaway of the bearing.

In the present case the test was not concluded (see Figure 40) as the wire used in the loading mechanism snapped after the load of 155.9 N was applied. Note, though the test didn’t finish and was done when the shaft was bowed, still the load that the bearing was able to sustain before the loading mechanism failed far surpassed the previously reported load capacity of 116.1 N by Kim and Park [4] which was also at a higher speed (20,000 RPM). The better performance of the present bearing in terms of load carrying capacity can be attributed to the stiffer complaint structure as compared to the bearing in [4].

Table 6: Operating parameters: Test 1

Parameters	Values
Speed	10,000 RPM
Supply Pressure	80 psi
Air Flow	8 SCFH

The condition of the top foil after the test was completed is shown in Figure 41.

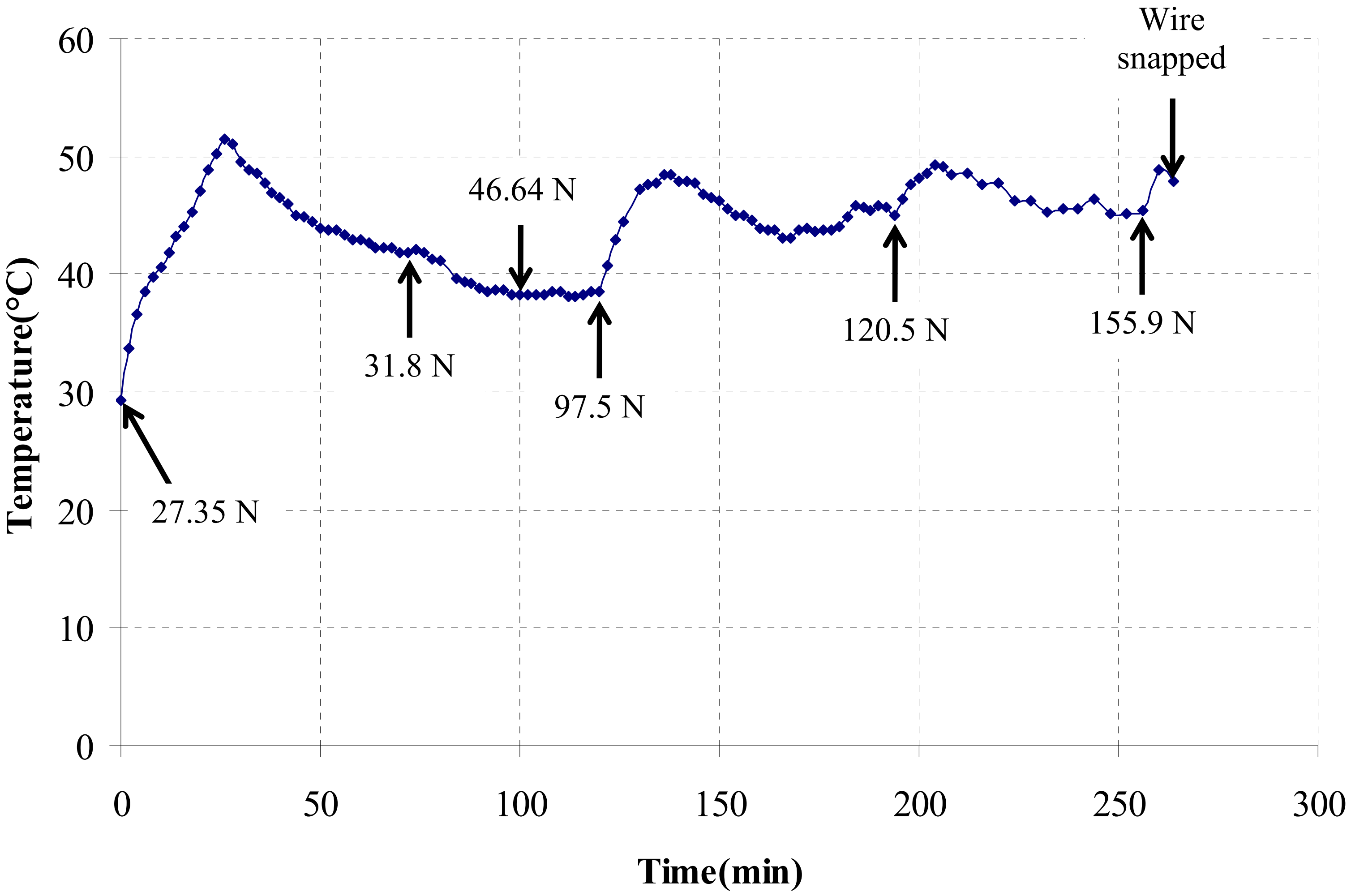

Figure 40: Test1: Load capacity test at 10,000 RPM with supply pressure of 80 psi and 8 SCFH air flow

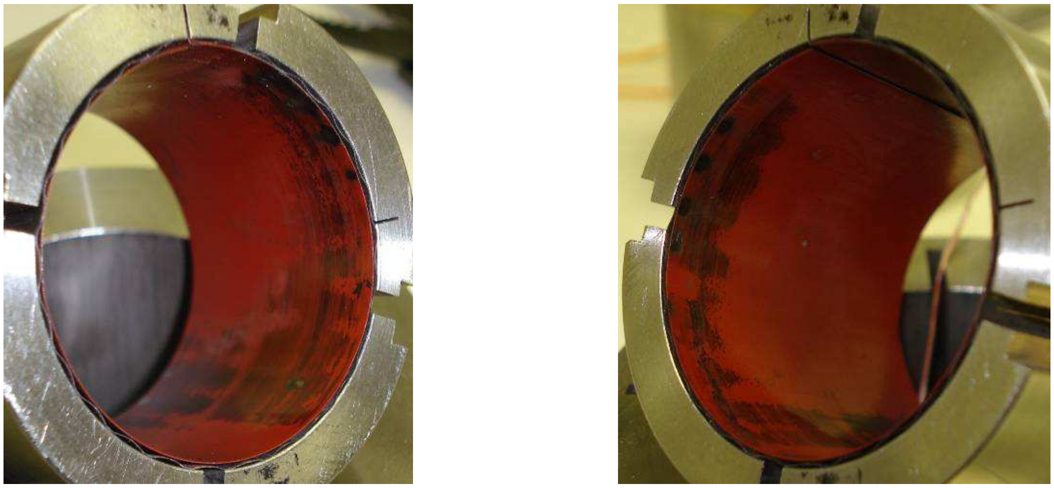

Figure 41: Top foil condition after Test 1; 10,000 RPM with supply pressure of 80 psi and 8 SCFH air flow

5.3.2 Test 2

The second test was performed with the same bearing (as Test1) but at a higher operating speed of 20,000 RPM. The operating parameters are summarized in table below.

Table 7: Operating parameters: Test 2

Parameters	Values
Speed	20,000 RPM
Supply Pressure	80 psi
Air Flow	8 SCFH

In this case even a small initial load of 27.35 N to the bearing resulted in bearing failure. The bearing failure was preceded with high vibration of the bearing and housing.

These vibrations point to the severe stick-slip rubbing of the rotor on the bearing surface. The reason for the rubbing was found to be the shaft bow which generates significant shaft whirl (see section 4.5). The wear on the top foil after the bearing failure is shown Figure 42. Note, the damage on the top foil is uniform in the circumferential direction and is predominantly on one of the edge. All the subsequent tests were done with the slow roll elimination of the shaft bow as described in section 4.5. Also, during the testing it was observed that the rubbing between the top foil and rotor results in localized welding of the two. This localized welding puts a significant amount of strain on the driving motor and damages the surface of the test section. Therefore in order to circumvent the damage an upper limit on the top foil temperature was required when estimating the load capacity of the bearing. This upper limit will however not provide the ultimate load capacity but given the possibility of damaging the test section this methodology was adopted for further testing. The upper limit on the temperature was established in the subsequent test.

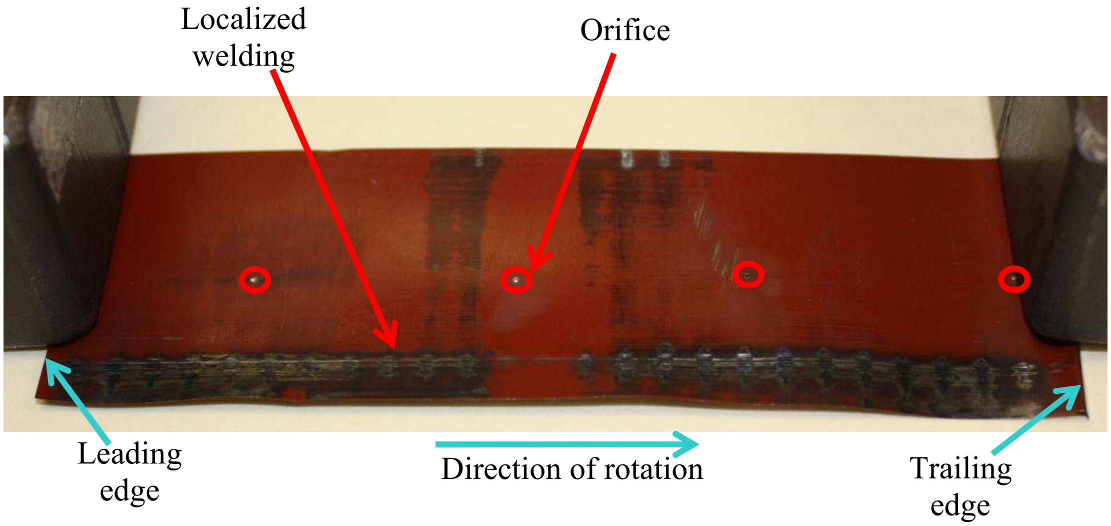

Figure 42: Top foil wear after Test 2; 20,000 RPM with supply pressure of 80 psi and 8 SCFH air flow

5.3.3 Test 3

Following the failure of the previous bearing, a new HAFB was made and as mentioned earlier the shaft bow was removed by grinding the test section. The present testing was done at 20,000 RPM, the speed at which the previous bearing failed. Further, the air flow was increased to contribute in circumventing any bearing failure. The operating parameters are listed in Table 8.

Table 8: Operating parameters: Test 3

Parameters	Values
Speed	20,000 RPM
Supply Pressure	80 psi
Air Flow	14 SCFH

The same methodology for increasing the load on the bearing was followed as in Test 1. The result from the present testing is shown in Figure 43. The bearing was tested up to 153N and the bearing failed at 159N. Note the top foil temperature at the bearing failure was in excess of 70°C. This temperature was established as the temperature beyond which there is very high possibility of bearing failure. As compared to the load capacity test done in [4] at the same operating speed, the load capacity in the present case is much higher.

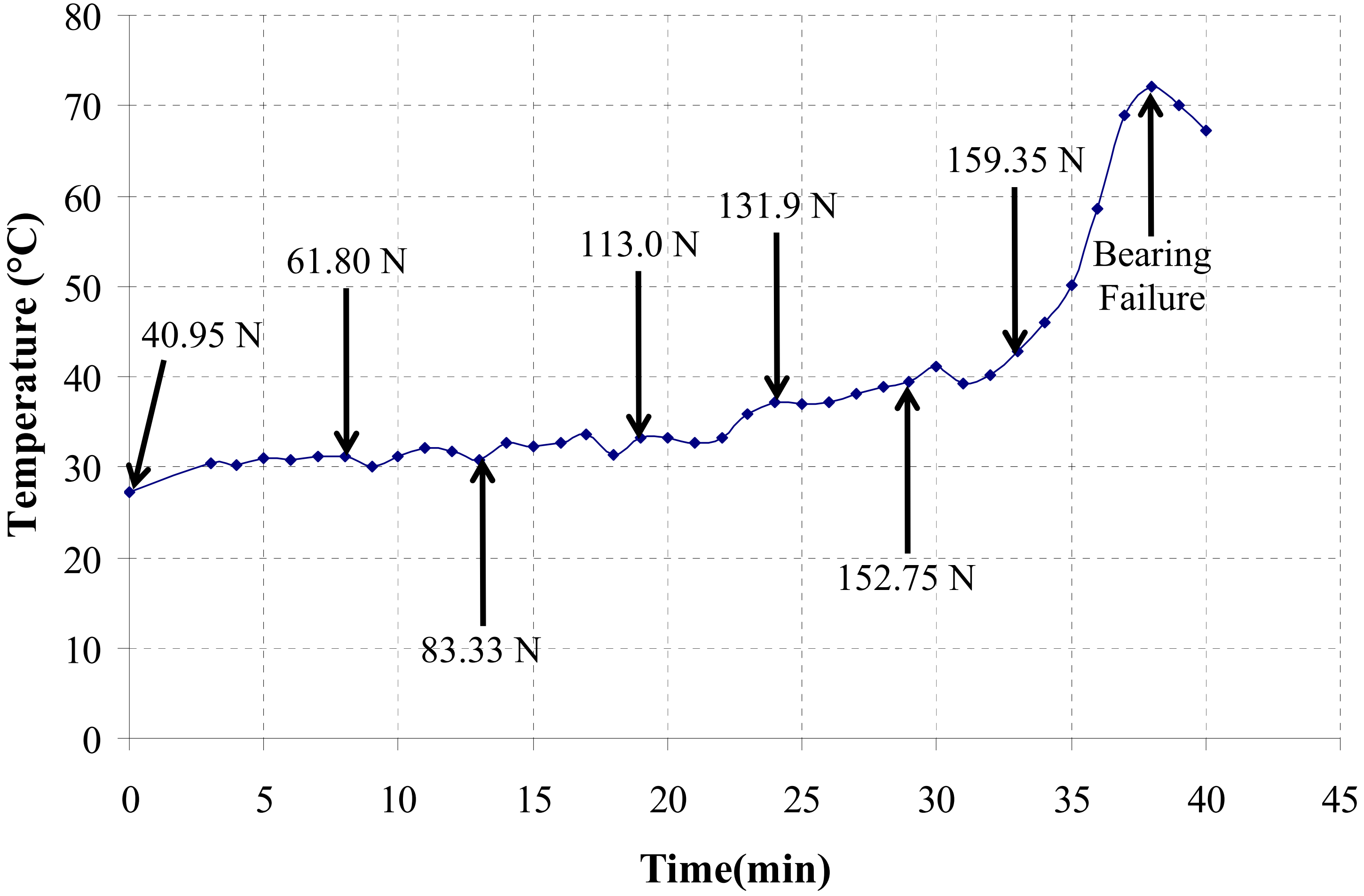

Figure 43: Load capacity test at 20,000 RPM with supply pressure of 80 psi and 14 SCFH air flow

The bearing failure in this case also resulted in localized welding and damage to the test section surface. See Figure 44 for the top foil wear after the test. Here again the damage was on one of the edge of the top foil and is circumferentially uniform.

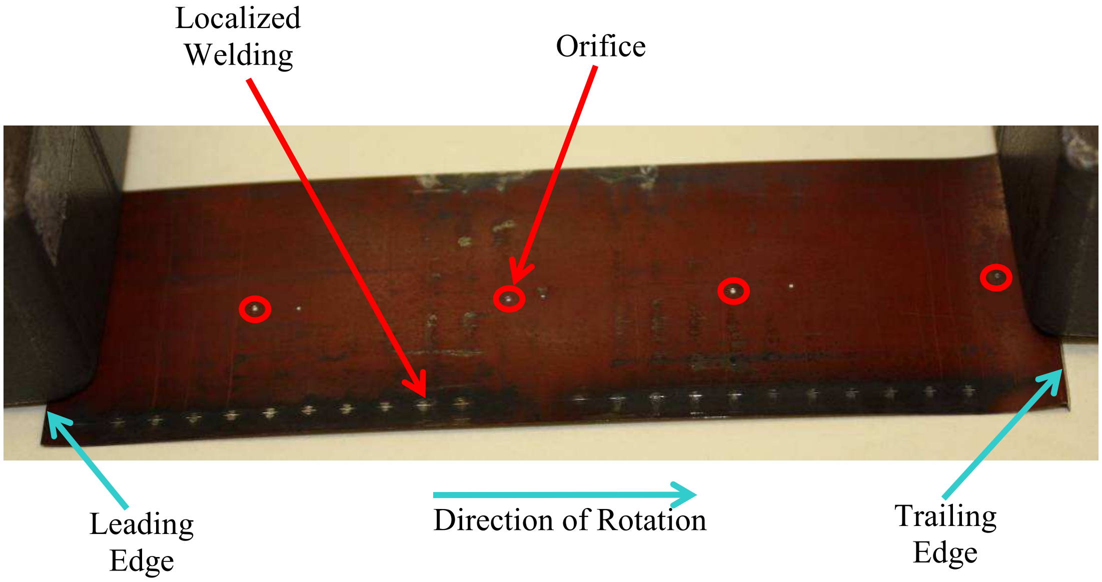

Figure 44: Top foil wear after Test 3; 20,000 RPM with supply pressure of 80 psi and 14 SCFH air flow

5.3.4 Test 4

Since the prototype bearing failed during the previous test, a new bearing was constructed. The previous tests were conducted at 10,000 RPM and 20,000 RPM, but this test was conducted at 15,000 RPM. Other operating parameters are listed in Table 9.

Table 9: Operating parameters: Test 4

Parameters	Values
Speed	15,000 RPM
Supply Pressure	80 psi
Air Flow	14 SCFH

Result of the test conducted is shown in Figure 45. The sharp increase in temperature initially (t=18 to t=20 min) was due to sudden increase in load (60.80 to 80.1 N). Subsequently the bearing load was decreased (80.1 to 60.25 N) and then the increment in load was gradually applied. Note that the test was stopped at about 80°C which is 10° higher than the temperature where the previous bearing failed. Also at this time the top foil was experiencing a sharp increase in temperature. Since the top foil temperature was well beyond the temperature where the previous bearing failed and was sharply increasing it was decided to stop the test to avoid any damage to the test section surface and preserve this bearing for future testing.

The load on the bearing (120.85 N) before the sharp increase in temperature (t <90 min) was established as the load capacity under the above mentioned operating conditions. The top foil after the test is shown in Figure 46, where only minor break-in rubbing marks were observed.

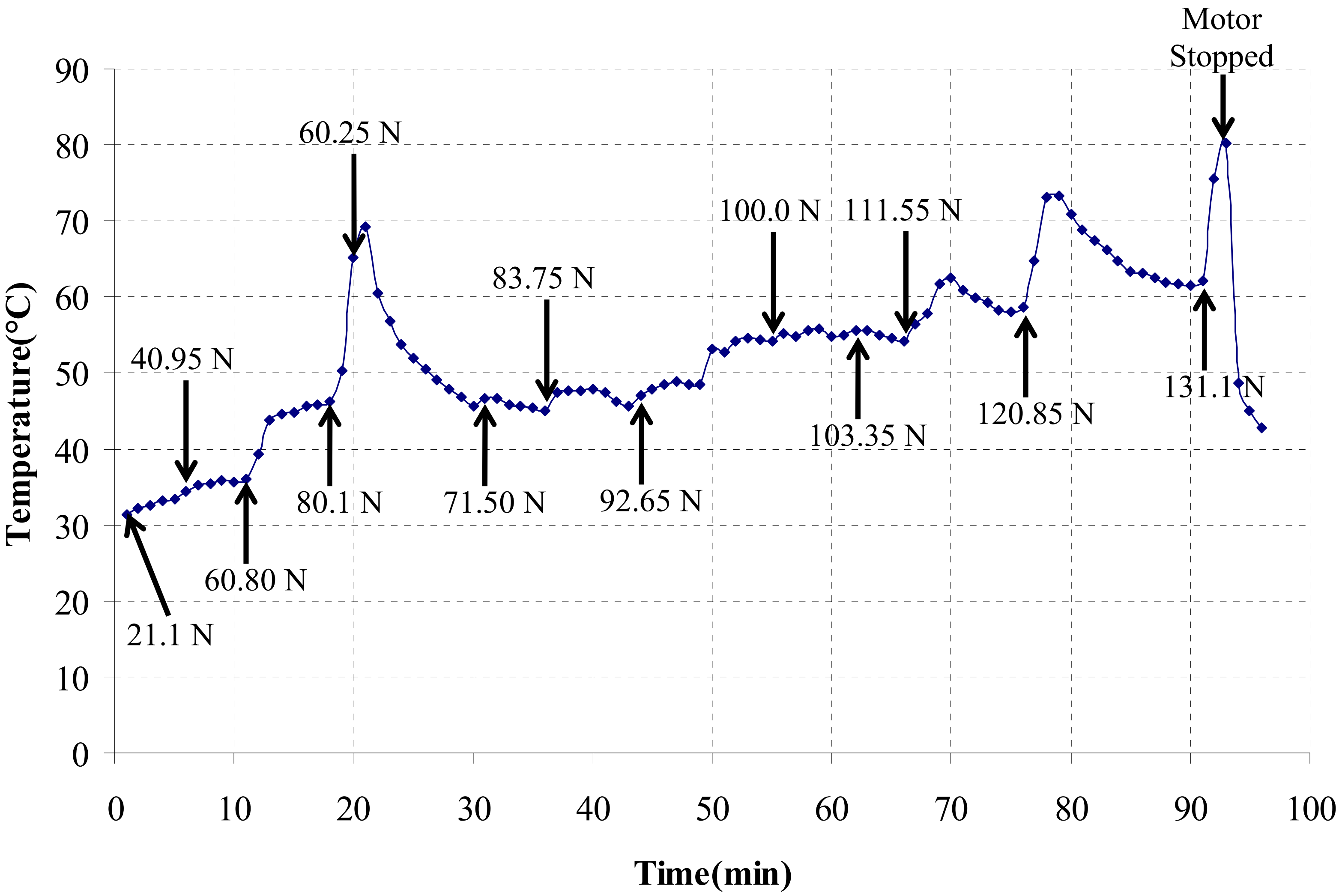

Figure 45: Load capacity test at 15,000 RPM with supply pressure of 80 psi and 14 SCFH air flow

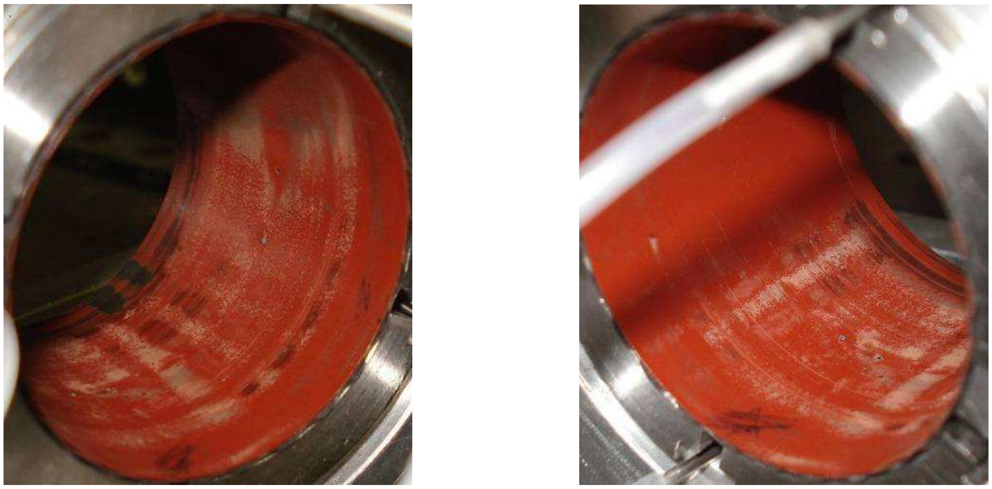

Figure 46: Top foil after Test 4; 15,000 RPM with supply pressure of 80 psi and 14 SCFH air flow

5.3.5 Tests 5 & 6

The same bearing as in Test 4 was used for the present tests. Except for the speeds all the other operating parameters were kept the same and are listed below.

Table 10: Operating parameters: Test 5 & 6

Parameters	Values	
Speed	Test 5	25,000 RPM
	Test 6	35,000 RPM
Supply Pressure	80 psi	
Air Flow	14 SCFH	

To maintain consistency with the previous test (Test 4), in both the present cases testing was done up to a maximum top-foil temperature of 80°C. The wear on the top foil after the tests is shown in Figure 47 and Figure 48. Note the condition of top foil after the test at 35,000 rpm is almost identical to the condition after the test at 25,000 rpm.

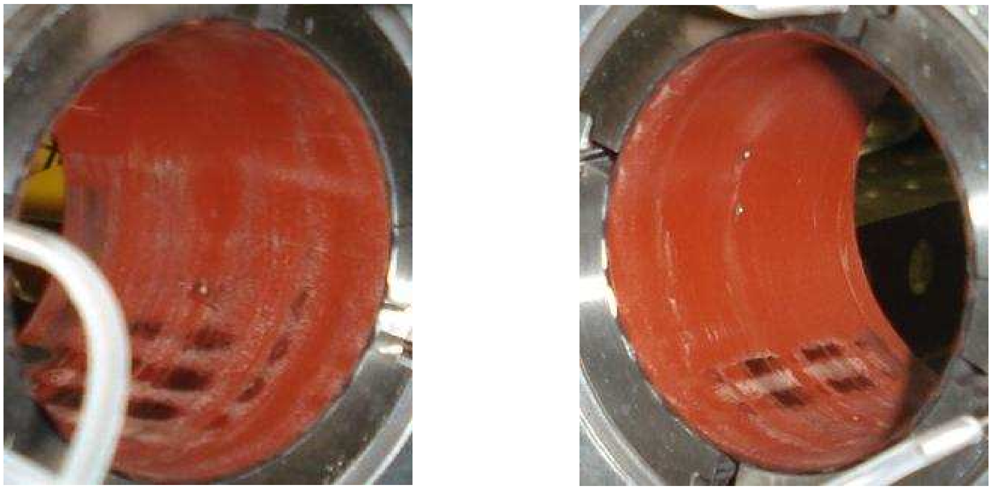

Figure 47: Top foil after Test 5; 25,000 RPM with supply pressure of 80 psi and 14 SCFH air flow

Figure 48: Top foil wear after Test 6; 35,000 RPM with supply pressure of 80 psi and 14 SCFH air flow

Results for the two cases are shown in Figure 49 and Figure 50. Note in Test 5 (Figure 49) the last bearing load resulted in a steady increase in top foil temperature, taking a conservative estimate the second last applied load (164.75N) was established as the load capacity. In Test 6 (Figure 50) the last applied load (202.23N) resulted in a steady temperature of around 80°C and hence the load capacity was established as 202.23N

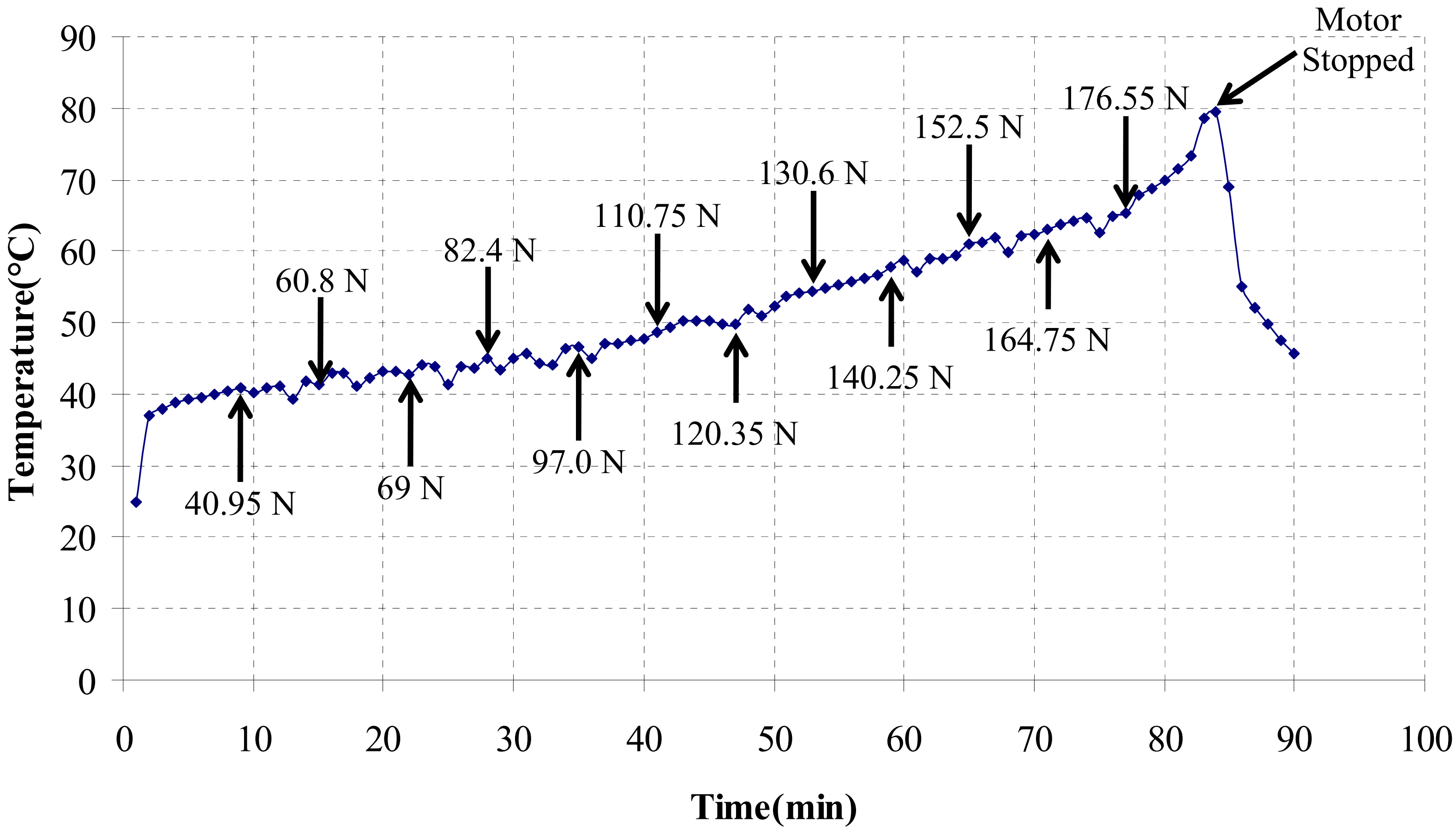

Figure 49: Load capacity test at 25,000 RPM with supply pressure of 80 psi and 14 SCFH air flow

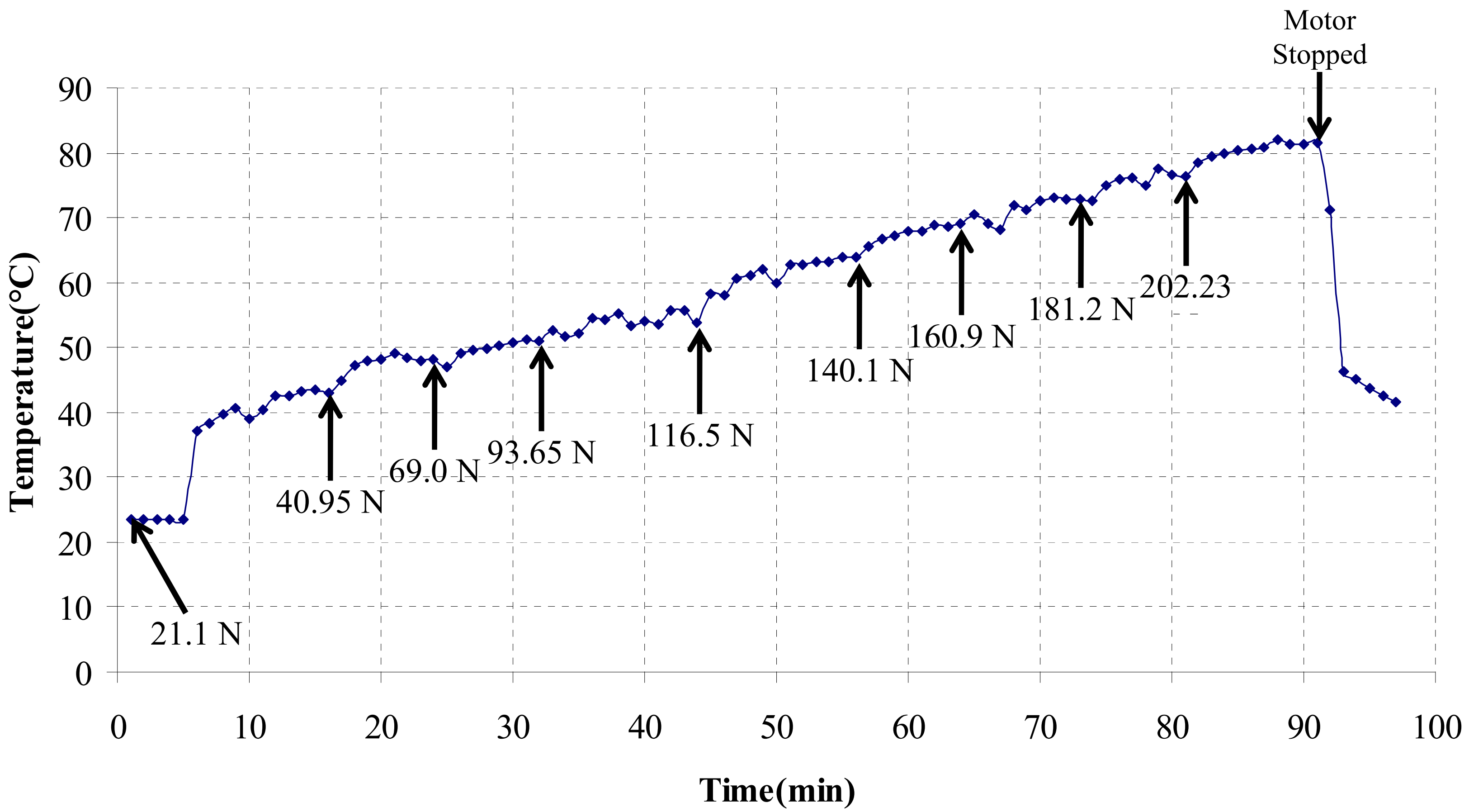

Figure 50: Load capacity test at 35,000 RPM with supply pressure of 80 psi and 14 SCFH air flow

.

5.3.6 Tests 7

The present test was conducted with bearing under hydrodynamic operation to compare with the hybrid operation. Note, the present bearing can be made to run hydrodynamically just by shutting the air supply to the feed lines. The rotor speed was chosen as 25,000 RPM. Top-foil wear after the test is shown in Figure 51 and the result in Figure 52. The last load applied took the bearing on the verge of failure. At this time the motor was bogging down and the top foil temperature shot up to 110°C. To avoid any damage, the load to the bearing was reduced and motor was subsequently stopped.

Taking the last load that resulted in a steady temperature of the top foil, the load capacity was established as 179.5 N. It is interesting to note that the current load capacity is higher than the load capacity in Test 5 where the bearing was under hybrid operation with the same rotor speed. This difference can be attributed to the fact that the load capacity in the present case is the ultimate load capacity which was not the case for the bearing in Test 5. However it should also be noted that last load applied to the bearing in Test 5 resulted in the top foil temperature of around 80°C, the temperature at which the present bearing was about to fail. These results indicate that the hydrostatic supply lines have no contribution towards the load capacity, especially when the bearing is heavily loaded.

Table 11 shows the top foil temperature at similar loads from the present test and Test 5. The top foil temperature is lower in the case of hybrid operation at each load indicating cooling effect from the hydrostatic air supply.

Table 11: Top foil temperature

Load (N)	Hybrid (°C)	Hydrodynamic (°C)
41	41.7	48.1
82	46.3	53.5
120	54.1	59.9
152	62.4	67.8
165	64.9	70.8

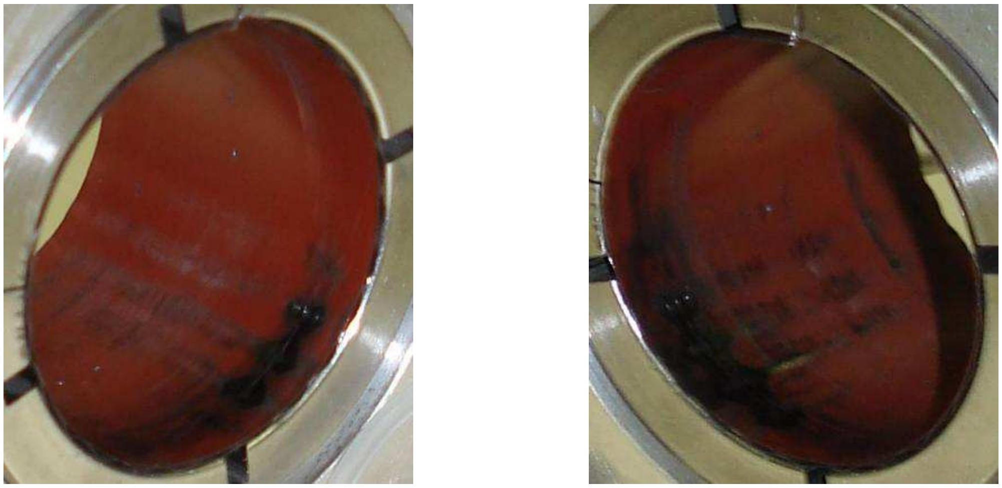

Figure 51: Top foil wear after Test 7; 25,000 RPM under hydrodynamic conditions

The summary of all the tests done is given in Table 12.

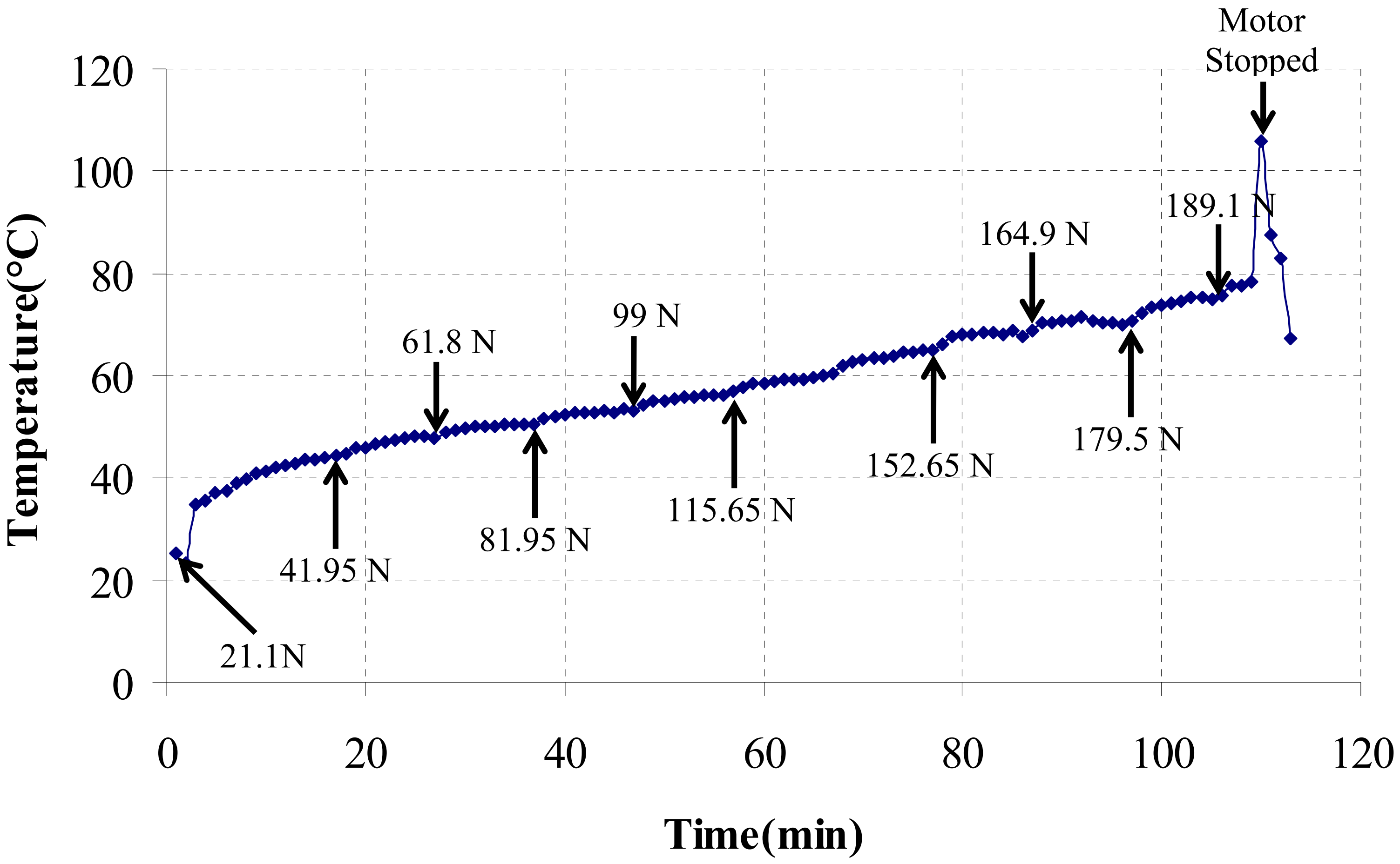

Figure 52: Load capacity test at 25,000 RPM – Hydrodynamic operation

Table 12: Summary of bearing load capacities

Test	Speed (RPM)	Clearance (µm)	Air Supply (SCFH)	Pressure (psi)	Shaft Bow	Test Completed	Maximum Load Applied (N)	Load Capacity (N)
1	10,000	25.4	8	80	Yes	No	155.9	—
2	20,000	25.4	8	80	Yes	No	27.35	—
3	20,000	38.1	14	80	No	Yes	159.35	152.75
4	15,000	38.1	14	80	No	Yes	131.1	120.85
5	25,000	38.1	14	80	No	Yes	176.55	164.75
6	35,000	38.1	14	80	No	Yes	202.23	202.23
7	25,000	38.1	—	—	No	Yes	189.1	179.5

5.3.7 Test 8

To ascertain the effectiveness of the supply lines at low speeds and under light loads a comparative test was conducted. The bearing was run under hydrodynamic and hybrid modes at 10,000 RPM and under 21.1N load, see Table 13 for other parameters. Since the speed is low, the hydrodynamic pressure generated will be low and hence one can see the effectiveness of the hydrostatic supply lines in terms of load sustenance. The results from the comparative test are shown in Figure 53. Running the bearing under hydrodynamic mode resulted in thermal instability and severe vibrations. The bearing was consequently unloaded and the motor was stopped. In the hybrid case the bearing didn't show any instability or vibrations and the top foil temperature stabilized after some time. Also, the top foil temperature under hybrid conditions was significantly low. These results indicate the superior performance of the bearing under hybrid mode.

Table 13: Operating parameters Test 8

Parameters	Values
Speed	10,000 RPM
Supply Pressure (Hybrid)	80 psi
Air Flow (Hybrid)	14 SCFH

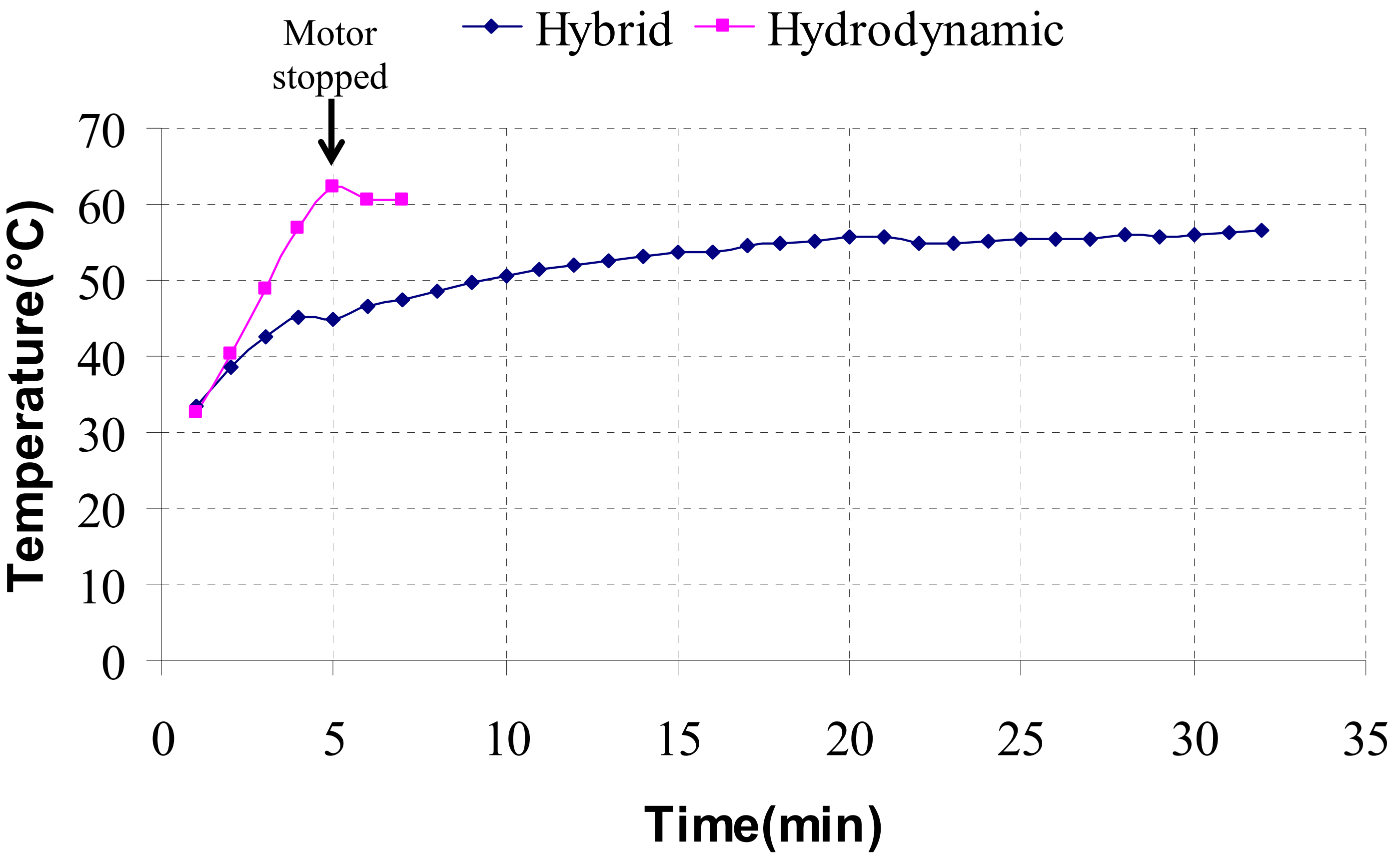

Figure 53: Comparative study at 10,000 RPM

6 CONCLUSIONS AND FUTURE WORK

6.1 Conclusions from analytical studies

Simulations show that feed parameter and supply pressure affects the dynamic characteristics of air foil bearings. With the increase in either the supply pressure or the feed parameter, the rotor centers itself and hence one sees a decrease in direct stiffness. Simulations show that the cross-coupled stiffness, which contributes as a destabilizing force, could be reduced by increasing either the supply pressure or the feed parameter. There is a critical feed parameter (Γ_s) at which the cross-coupled stiffness is minimal. Direct damping, which dampens the vibrations in the bearing, showed increasing trend with the supply pressure and the feed parameter. The predictions demonstrate the instabilities in air bearings can be attenuated by modulating the supply pressure.

Frequency-domain analysis of the bearing coefficients showed expected trends. The direct damping showed marginal changes with supply pressure but showed rapid increase with increasing excitation frequencies. The damping converged to null values for all the pressures for super-synchronous excitations. The loss in damping with high stiffness values for high frequency excitation is a typical hardening effect of gas bearings. In almost all the cases there are rapid decrease in cross-coupled stiffness and damping and the values show converging trends in super-synchronous regime.

The trends one sees in bearing stiffness coefficients with increasing bearing number are basically the trends with increasing rotational speed. In general direct stiffness increases rapidly at low bearing number but showed converging trends at high bearing number. It is interesting to note that the cross-coupled stiffness and direct damping decrease with increasing bearing number and cross-coupled stiffness is in fact negative for high pressures. Note that the destabilizing force is proportional to $K_{XY} - \frac{C_{XX}}{\omega}$ and with the trends in cross-coupled stiffness and direct-damping, there is a possibility that backward whirl may be induced in the bearing. But this backward whirl will always be dominated by forward whirl generated by the imbalance.

6.2 Conclusions from experimental studies

A new test rig with high speed capability was designed, constructed and commissioned. With minimal cooling (air as coolant) of the motor and grease lubrication in the spindle ball bearings, the test rig was commissioned up to 45,000 RPM. Commissioning of the test rig beyond this speed may require better cooling and air-mist lubrication of the ball bearings. The test rig was designed such that both of the above mentioned enhancements can be implemented very easily.

Following the completion of the test rig, experiments were conducted on the prototype HAFB. Several tests were conducted to determine the load capacity of the hybrid air foil bearing at various operating speeds. Noticeable enhancement in load capacity was observed as compared to the tests conducted by authors in [4]. Major contribution in the enhancement of the load capacity came form the stiffer complaint structure of the present bearing as compared to the HAFB in [4]. An increase in load capacity was observed with increasing speeds (see Tests 4, 5&6). This trend is expected because higher speeds results in higher wedge effect which consequently increases the generated hydrodynamic pressure. Comparison between hybrid and hydrodynamic operation at a relatively high speed (25,000 rpm) indicated no contribution from the hydrostatic supply lines towards the load capacity especially when the bearing is heavily loaded. However in the case of hybrid operation the top foil temperature was lower at a given load which can be attributed to the cooling provided by the hydrostatic supply lines. Furthermore, the comparative test at low speed (10,000 RPM) showed much better performance of the bearing under hybrid operation as compared to hydrodynamic operation.

6.3 Future work

Zeroth order orbit simulations can be extended to three dimensional orbit simulations. These simulations include both rotor and bearings in the analysis and can include both cylindrical and conical modes. Furthermore the bearing code can be coupled with the rotordynamic code which can extend the analysis beyond the rigid modes to the bending modes. This approach will however be iterative and time consuming.

On the experimental side, the investigation can be extended to higher speeds. The experiments at higher speeds will help in studying the effect of shaft bending on the bearing load capacity. It will also be interesting to monitor not only the temperature but the viscous torque generated by the bearing during the load capacity tests. More thermocouples can be included along the bearing's circumferential and axial direction to get a better picture of the efficiency of the hydrostatic effect. More temperature probes will also be helpful in determining thermal gradients within the bearing.

The bearing it self can be improved with better feed lines, possibly replacing all the silicone tube with steel tubes. Improvements in the test rig can include a pneumatic loading system. A pneumatic system with an electronic regulator will provide an accurate loading mechanism as compared to the present system which utilizes dead weights. The data acquisition system can also be upgraded to a faster data logger.

REFERENCES

[1] Agrawal, G. L., 1997, "Foil Air/Gas Bearing Technology - an Overview," *in Proceedings of the International Gas Turbine & Aeroengine Congress & Exposition*, Orlando, FL, ASME paper 97-GT-347.

[2] Lemmens, J. J. M., Gasunie, N. V. N., Overdiep, J. J., Bos, K. H., and Bartholomeus, P. M. G., 2006, "Demonstration of Capstone Microturbines Including High Efficiency Heat Exchanger, Gas Safeguard Module and Natural Gas Compressor, Developed by Gasunie Engineering & Technology," 23rd World Gas Conference.

[3] Mohawk, 2008(Feburary 15), "Miti - Foil Bearing Example Applications - Compressor - Gas Turbine - Turbocharger - Motors," http://www.miti.cc/foil-bearings-applications.html.

[4] Kim, D., and Park, S., 2006, "Hybrid Air Foil Bearings with External Pressurization," *in Proceedings of the International Mechanical Engineering Congress and Exposition*, Chicago, IL.

[5] Heshmat, H., Walowit, J. A., and Pinkus, O., 1983, "Analysis of Gas-Lubricated Foil Journal Bearings," Journal of Lubrication Technology, **105**, pp. 647-655.

[6] Heshmat, H., and Ku, C.-P. R., 1992, "Compliant Foil Bearing Structural Stiffness Analysis: Part I – Theoretical Model Including Strip and Variable Bump Foil Geometry," ASME Journal of Tribology, **114**(2), pp. 394-400.

[7] Ku, C.-P. R., and Heshmat, H., 1992, "Compliant Foil Bearing Structural Stiffness Analysis Part II: Experimental Investigation," ASME Journal of Tribology, **115**(3), pp. 364-369.

[8] Peng, J.-P., and Carpino, M., 1992, "Calculation to Stiffness and Damping Coefficients for Elastically Supported Gas Foil Bearings," ASME Journal of Tribology, **115**, pp. 20-27.

[9] Carpino, M., 1997, "Finite Element Approach to the Prediction of Foil Bearing Rotor Dynamic Coefficients," ASME Journal of Tribology, **119**, pp. 85-90.

[10] Han, D.-C., Park, S.-S., Kim, W.-J., and Kim, J.-W., 1994, "A Study on the Characteristics of Externally Pressurized Air Bearings," Journal of American Society of Precision Engineering, **16**, pp. 164-173.

[11] Dellacorte, C., and Valco, M. J., 2001, "Load Capacity Estimation of Foil Air Journal Bearing for Oil-Free Turbomachinery Application," STLE Tribology Transactions, **43**(4), pp. 795-801.

[12] Radil, K., Howard, S., and Dykas, B., 2002, "The Role of Radial Clearance on the Performance of Foil Air Bearings," STLE Tribology Transactions, **45**(4), pp. 485-490.

[13] Wilde, D. A., and Andres, L. S., 2003, "Comparison of Rotordynamic Analysis Predictions with the Test Response of Simple Gas Hybrid Bearings for Oil Free Turbomachinery," ASME Journal of Engineering for Gas Turbines and Power, **128**, pp. 634-643.

[14] Peng, Z.-C., and Khonsari, M. M., 2006, "A Thermohydrodynamic Analysis of Foil Journal Bearings," ASME Journal of Tribology, **128**, pp. 534-541.

[15] Song, J.-H., and Kim, D., 2007, "Foil Gas Bearing with Compression Springs: Analyses and Experiments," ASME Journal of Tribology, **129**(3), pp. 628-639.

[16] Kim, D., 2007, "Parametric Studies on Static and Dynamic Performance of Air Foil Bearings with Different Top Foil Geometries and Bump Stiffness Distributions," ASME Journal of Tribology, **129**(2), pp. 354-364.

[17] Iordanoff, I., 1999, "Analysis of an Aerodynamic Compliant Foil Thrust Bearing: Method of a Rapid Design," ASME Journal of Tribology, **121**, pp. 816-822.

[18] Rubio, D., and Andrés, L. S., 2005, "Structural Stiffness, Dry-Friction Coefficient and Equivalent Viscous Damping in a Bump-Type Foil Gas Bearing," ASME Journal of Engineering for Gas Turbines and Power, **129**(2), pp. 494-502.

[19] Ku, C. P., and Heshmat, H., 1994, "Structural Stiffness and Coulomb Damping in Compliant Foil Journal Bearing: Parametric Studies," STLE Tribology Transactions, **37**, pp. 455-464.

[20] Salehi, M., Heshmat, H., and Walton, J., 2003, "On the Frictional Damping Characteristics of Compliant Bump Foils," ASME Journal of Tribology, **125**, pp. 804-813.

[21] GMN, 2007(March 15), "Bearing Catalog," http://www.gmnbt.com/pdf/ballbearings.pdf.

[22] e+a, 2007(March 15), "2 Pole Types Overview," http://www.eunda.ch/images/stories/downloads/2-pole_types_overview.pdf.

[23] INSTA, 2008(May 15), "Insta Controls - Ptc Thermistors," http://www.faet.it/data/UserFiles/File/Ptc.pdf.

[24] Newport, 2008(May 15), "High-Performance Low-Profile Ball Bearing Linear Stages," http://www.newport.com/file_store/PDFs/tempPDFs/e3164_423-433-443-Series-High-Performance-Low-Profile-B.pdf.

APPENDIX A

NON-DIMENSIONALIZATION OF REYNOLDS EQUATION

Reynolds Equation for Hydrostatic Bearing is given by, see section 3.2 for derivation

$$\frac{R_g T \dot{m}_s}{A} + \nabla.\left(\frac{1}{12\mu} ph^3 \nabla p\right) = \frac{U}{2}\frac{\partial}{\partial x}(ph) + \frac{\partial}{\partial t}(ph) \tag{20}$$

In the above equations *x* is a local coordinate attached on the bearing surface along the circumferential direction, *z* is a coordinate in axial direction, *h* is a film thickness, *p* is pressure, μ is viscosity of air, R_g is the gas constant of air and *T* is the temperature of supplied air. In the above equation $\dot{m}_s$ is the mass flow rate from the hydrostatic supply line and for isentropic processes under choked and unchoked conditions is case is given by

Choked case, $\frac{P}{P_s} > \left(\frac{2}{k+1}\right)^{\frac{k}{(k-1)}} = 0.5283$

$$\dot{m}_s = \rho_s A_o V_0 = \frac{p_s}{\sqrt{R_g T_s}} A_o \left[\left(2\gamma_g \frac{k}{k+1}\right)^{1/2} \left(\frac{2}{k+1}\right)^{1/(k-1)}\right]^{1/2} \tag{21}$$

Unchoked case, $\frac{P}{P_s} < \left(\frac{2}{k+1}\right)^{\frac{k}{(k-1)}} = 0.5283$

$$\dot{m}_s = \rho_s A_o V_0 = \frac{p_s}{\sqrt{R_g T_s}} A_o \left[2\gamma_g \frac{k}{k-1}\left(\left(\frac{P}{P_s}\right)^{2/k} - \left(\frac{P}{P_s}\right)^{(k+1)/k}\right)\right]^{1/2} \tag{22}$$

Let

$$P=\frac{p}{P_a},\theta=\frac{x}{R},Z=\frac{z}{R},\tau=\omega t,H=\frac{h}{C} \tag{23}$$

Substituting we get

$$\frac{R_g T\dot{m}_s}{A}+\nabla.\left(\frac{1}{12\mu}PP_aH^3C^3\ \nabla PP_a\right)=\frac{U}{2R}\frac{\partial}{\partial\theta}(PP_aHC)+\omega\frac{\partial}{\partial\tau}\left(PP_aHC\right) \tag{24}$$

Expanding we get

$$\begin{aligned}&\frac{R_g T\dot{m}_s 12\mu R^2}{AP_a^2C^3}+\frac{\partial}{\partial\theta}\left(PH^3\frac{\partial P}{\partial\theta}\right)+\frac{\partial}{\partial Z}\left(PH^3\frac{\partial P}{\partial\theta}\right)\\&=\left(\frac{6U\mu R}{P_aC^2}\right)\frac{\partial}{\partial\theta}(PH)+\left(\frac{12\omega\mu R^2}{P_aC^2}\right)\frac{\partial}{\partial\tau}\left(PH\right)\end{aligned} \tag{25}$$

Now

$$U=\omega R,\ \Lambda=\frac{6\omega\mu}{P_a}\left(\frac{R^2}{C^2}\right),\ \sigma=\frac{12\omega\mu}{P_a}\left(\frac{R^2}{C^2}\right),\ A=\Delta x\Delta z=\Delta\theta\Delta ZR^2 \tag{26}$$

Where $U,\ \Lambda,\ \sigma$ are rotor surface velocity, bearing number and squeeze number respectively. Substituting the above expressions in equation (25) we get

$$\frac{12\mu R_g T\dot{m}_s}{P_a^2C^3\Delta\theta\Delta Z}+\frac{\partial}{\partial\theta}\left(PH^3\frac{\partial P}{\partial\theta}\right)+\frac{\partial}{\partial Z}\left(PH^3\frac{\partial P}{\partial\theta}\right)=\Lambda\frac{\partial}{\partial\theta}\left(PH\right)+\sigma\frac{\partial}{\partial\tau}\left(PH\right) \tag{27}$$

Let $\dot{M}_s=\dfrac{12\mu R_g T\dot{m}_s}{P_a^2C^3}$ and since σ=2Λ we get

$$\frac{\dot{M}_s}{\Delta\theta\Delta Z}+\frac{\partial}{\partial\theta}\left(PH^3\frac{\partial P}{\partial\theta}\right)+\frac{\partial}{\partial Z}\left(PH^3\frac{\partial P}{\partial\theta}\right)=\Lambda\frac{\partial}{\partial\theta}\left(PH\right)+2\Lambda\frac{\partial}{\partial\tau}\left(PH\right) \tag{28}$$

The above equation is non-dimensional form of Reynolds equation for hydrostatic bearings. Again using equations (21) and (22) we get the following expressions for $\dot{M}_s$.

Choked,

$$\dot{M}_S = \Gamma_s P_s H \left(2\gamma_g \frac{k}{k+1} \right)^{\frac{1}{2}} \left(\frac{2}{k+1} \right)^{\frac{1}{(k-1)}} \tag{29}$$

Unchoked,

$$\dot{M}_S = \Gamma_s P_s H \left[2\gamma_g \frac{k}{k-1} \left(\left(\frac{P}{P_s} \right)^{\frac{2}{k}} - \left(\frac{P}{P_s} \right)^{\frac{(k+1)}{k}} \right) \right]^{\frac{1}{2}} \tag{30}$$

where $\Gamma_s = \dfrac{12\mu C_d A_0 \sqrt{R_g T}}{p_a C^3}$ is a feed parameter, P_s is the supply pressure, k is the ratio of specific heats for air, C_d is a discharge coefficient. In the feed parameter, A_0 is the reference orifice curtain area defined as $A_0 = \pi d_o C$, where d_0 is the orifice diameter.

Equation (28) can also be expressed in vector form as shown below

$$\frac{\dot{M}_s}{\Delta\theta\Delta Z} - 2\Lambda \frac{\partial}{\partial \tau}\left(PH\right) = \nabla . Q_J \tag{31}$$

where

$$Q_J = \left(\Lambda PH - PH^3 \frac{\partial P}{\partial \theta} \right) i_\theta + \left(-PH^3 \frac{\partial P}{\partial Z} \right) i_z \tag{32}$$

APPENDIX B

ZEROTH AND FIRST ORDER EQUATIONS

The shaft is perturbed harmonically about the steady state position as shown below

$$e_X = e_{X0} + \Delta e_X e^{i\omega_S t},\ e_Y = e_{Y0} + \Delta e_Y e^{i\omega_S t} \tag{33}$$

Where ω_s is the excitation frequency. These perturbations will also produce small harmonic deflections in the bump foil along with the steady state deflection

$$u = u_0 + \Delta u_X e^{i\omega_S t} + \Delta u_Y e^{i\omega_S t} \tag{34}$$

The film thickness for the air foil bearing using the coordinate system shown in Figure 2, page 11 is given by

$$h = C + e_X \cos\theta + e_y \sin\theta + u \tag{35}$$

Substituting values from values from (33) and (34) we get

$$\begin{aligned} &h = C + e_{X0}\cos\theta + e_{Y0}\sin\theta + \Delta e_X e^{i\omega_S t}\cos\theta + \Delta e_Y e^{i\omega_S t}\sin\theta \\ &+u_0 + \Delta u_X e^{i\omega_S t} + \Delta u_Y e^{i\omega_S t} \end{aligned} \tag{36}$$

Rearranging we get

$$h = h_0 + \Delta h_X e^{i\omega_S t} + \Delta h_Y e^{i\omega_S t} \tag{37}$$

Where

$$\begin{aligned} \Delta h_X &= \Delta e_X \cos\theta + \Delta u_X \\ \Delta h_Y &= \Delta e_Y \sin\theta + \Delta u_Y \end{aligned} \tag{38}$$

In non-dimensional form the above equations is given by

$$\begin{aligned} &H = H_0 + \Delta H_X e^{i\tau} + \Delta H_Y e^{i\tau}, U = U_0 + \Delta U_X e^{i\tau} + \Delta U_Y e^{i\tau} \\ &\Delta H_X = \Delta\varepsilon_X \cos\theta + \Delta U_X, \\ &\Delta H_Y = \Delta\varepsilon_Y \sin\theta + \Delta U_Y \end{aligned} \tag{39}$$

The harmonic excitations will also perturb the pressure profile; the total non-dimensional pressure is given by

$$P = P_0 + \Delta P = P_0 + \Delta\varepsilon_X P_X e^{i\tau} + \Delta\varepsilon_Y P_Y e^{i\tau} = P_0 + \sum_{\alpha = X,Y} \Delta\varepsilon_\alpha P_\alpha e^{i\tau} \tag{40}$$

Where $P_\alpha = \dfrac{\Delta P}{\Delta\varepsilon_\alpha}$ ($\alpha = X,Y$). Note that P_X and P_Y are complex number with real and imaginary parts.

Non-dimensional bump deflection equation is given by

$$P = K_b U + C_b \nu \frac{dU}{d\tau} \tag{41}$$

Substituting values from equation (39) and (40) in the above equation we get

$$\begin{aligned} & P_0 + \Delta\varepsilon_X P_X e^{i\tau} + \Delta\varepsilon_Y P_Y e^{i\tau} \\ & = K_b \left(U_0 + \Delta U_X e^{i\tau} + \Delta U_Y e^{i\tau} \right) + C_b \nu \left(\Delta U_X i e^{i\tau} + \Delta U_Y i e^{i\tau} \right) \end{aligned} \tag{42}$$

Using relations from equation (39) and dropping the zeroth order terms we get

$$\begin{aligned} & \Delta\varepsilon_X P_X + \Delta\varepsilon_Y P_Y \\ & = K_b \left(\Delta H_X - \Delta\varepsilon_X \cos\theta + \Delta H_Y - \Delta\varepsilon_Y \sin\theta \right) \\ & + C_b \nu i \left(\Delta H_X - \Delta\varepsilon_X \cos\theta + \Delta H_Y - \Delta\varepsilon_Y \sin\theta \right) \end{aligned} \tag{43}$$

Separating the X and Y components we get

$$\begin{aligned} \Delta\varepsilon_X P_X &= K_b \left(\Delta H_X - \Delta\varepsilon_X \cos\theta \right) + C_b \nu i \left(\Delta H_X - \Delta\varepsilon_X \cos\theta \right) \\ \Delta\varepsilon_Y P_Y &= K_b \left(\Delta H_Y - \Delta\varepsilon_Y \sin\theta \right) + C_b \nu i \left(\Delta H_Y - \Delta\varepsilon_Y \sin\theta \right) \end{aligned} \tag{44}$$

Dividing by $\Delta\varepsilon_\alpha$ and using $\dfrac{\Delta H_\alpha}{\Delta\varepsilon_\alpha} = H_\alpha$ ($\alpha = X,Y$) we get

$$\begin{aligned} P_X &= K_b \left(H_X - \cos\theta \right) + C_b \nu i \left(H_X - \cos\theta \right) \\ P_Y &= K_b \left(H_Y - \sin\theta \right) + C_b \nu i \left(H_Y - \sin\theta \right) \end{aligned} \tag{45}$$

Rearranging we get

$$\frac{P_X}{K_b + C_b \nu i} + \cos\theta = H_X, \quad \frac{P_Y}{K_b + C_b \nu i} + \sin\theta = H_Y \tag{46}$$

Introducing small perturbations in equation (28) we get

$$\begin{aligned}
&\frac{\partial}{\partial\theta}\left(\left(P_0 + \Delta P\right)\left(H_0 + \Delta H\right)^3 \frac{\partial\left(P_0 + \Delta P\right)}{\partial\theta}\right) + \\
&\frac{\partial}{\partial Z}\left(\left(P_0 + \Delta P\right)\left(H_0 + \Delta H\right)^3 \frac{\partial\left(P_0 + \Delta P\right)}{\partial Z}\right) + \frac{\dot{M}_s(H_0 + \Delta H, P_0 + \Delta P)}{\Delta\theta\Delta Z} = \\
&\Lambda \frac{\partial}{\partial\theta}\left[\left(P_0 + \Delta P\right)\left(H_0 + \Delta H\right)\right] + 2\Lambda \frac{\partial}{\partial\tau}\left[\left(P_0 + \Delta P\right)\left(H_0 + \Delta H\right)\right]
\end{aligned} \tag{47}$$

Expanding the above equation we get

$$\begin{aligned}
&\frac{\partial}{\partial\theta}\left(\left(P_0 + \Delta P\right)\left(H_0^3 + \Delta H^3 + 3\Delta H^2 H_0 + 3\Delta H H_0^2\right)\left(\frac{\partial P_0}{\partial\theta} + \frac{\partial\Delta P}{\partial\theta}\right)\right) + \\
&\frac{\partial}{\partial Z}\left(\left(P_0 + \Delta P\right)\left(H_0^3 + \Delta H^3 + 3\Delta H^2 H_0 + 3\Delta H H_0^2\right)\left(\frac{\partial P_0}{\partial Z} + \frac{\partial\Delta P}{\partial Z}\right)\right) + \\
&\frac{\dot{M}_s(H_0 + \Delta H, P_0 + \Delta P)}{\Delta\theta\Delta Z} = \\
&\Lambda \frac{\partial}{\partial\theta}\left(P_0 H_0 + P_0\Delta H + H\Delta P + \Delta P\Delta H\right) + 2\Lambda\nu \frac{\partial}{\partial\tau}\left(P_0 H_0 + P_0\Delta H + H\Delta P + \Delta P\Delta H\right)
\end{aligned} \tag{48}$$

By further expansion and neglecting higher order terms we get

$$\begin{aligned}
&\frac{\partial}{\partial\theta}\left(\left(P_0 H_0^3 + 3P_0\Delta H H_0^2 + \Delta P H_0^3\right)\left(\frac{\partial P_0}{\partial\theta} + \frac{\partial\Delta P}{\partial\theta}\right)\right) + \\
&\frac{\partial}{\partial Z}\left(\left(P_0 H_0^3 + 3P_0\Delta H H_0^2 + \Delta P H_0^3\right)\left(\frac{\partial P_0}{\partial Z} + \frac{\partial\Delta P}{\partial Z}\right)\right) + \\
&\frac{\dot{M}_s(H_0 + \Delta H, P_0 + \Delta P)}{\Delta\theta\Delta Z} = \\
&\Lambda \frac{\partial}{\partial\theta}\left(P_0 H_0 + P_0\Delta H + H\Delta P\right) + 2\Lambda\nu \frac{\partial}{\partial\tau}\left(P_0 H_0 + P_0\Delta H + H\Delta P\right)
\end{aligned} \tag{49}$$

The perturbations in the mass flow term is done using Taylor series expansion. Let the mass flow be represented by

$$\dot{M}_S = \left(2\gamma_g \frac{k}{k-1} \right)^{\frac{1}{2}} \Gamma_s P_s f\left(H, P\right) \tag{50}$$

Therefore

$$\dot{M}_S \left(H + \Delta H, P + \Delta P\right) = \left(2\gamma_g \frac{k}{k-1} \right)^{1/2} \Gamma_s P_s f(H + \Delta H, P + \Delta P) \tag{51}$$

Using Taylor series expansion and neglecting higher order terms we get

$$f(H_0 + \Delta H, P_0 + \Delta P) = f(H_0, P_0) + \left. \frac{\partial f(P,H)}{\partial P} \right|_{P_0, H_0} \Delta P + \left. \frac{\partial f(P,H)}{\partial H} \right|_{P_0, H_0} \Delta H \tag{52}$$

The function f and its derivates for the choked and unchoked conditions is given by

Choked,

$$f(H_0, P_0) = H_0 \tag{53}$$

$$\left. \frac{\partial f(P,H)}{\partial P} \right|_{P_0, H_0} = 0 \tag{54}$$

$$\left. \frac{\partial f(P,H)}{\partial H} \right|_{P_0, H_0} = 1 \tag{55}$$

Un-Choked

$$f(H_0, P_0) = H_0 \left(\left(\frac{P_0}{P_s} \right)^{\frac{2}{k}} - \left(\frac{P_0}{P_s} \right)^{\frac{(k+1)}{k}} \right)^{\frac{1}{2}} \tag{56}$$

$$\left. \frac{\partial f(P,H)}{\partial P} \right|_{P_0, H_0} = H_0 \frac{1}{2} \left(\left(\frac{P_0}{P_s} \right)^{\frac{2}{k}} - \left(\frac{P_0}{P_s} \right)^{\frac{k+1}{k}} \right)^{-\frac{1}{2}} \left(\frac{2}{k} \left(\frac{1}{P_s} \right)^{\frac{2}{k}} P_0^{\left(\frac{2}{k}-1\right)} - \frac{k+1}{k} \left(\frac{1}{P_s} \right)^{\frac{k+1}{k}} P_0^{\frac{1}{k}} \right) \tag{57}$$

$$\left.\frac{\partial f(P,H)}{\partial H}\right|_{P_0,H_0} = \left(\left(\frac{P_0}{P_s}\right)^{\frac{2}{k}} - \left(\frac{P_0}{P_s}\right)^{\frac{k+1}{k}}\right)^{\frac{1}{2}} \tag{58}$$

Using equation (52) equation (49) becomes

$$\begin{aligned}
&\frac{\partial}{\partial\theta}\left(\left(P_0H_0^3 + 3P_0\Delta HH_0^2 + \Delta PH_0^3\right)\left(\frac{\partial P_0}{\partial\theta} + \frac{\partial\Delta P}{\partial\theta}\right)\right) + \\
&\frac{\partial}{\partial Z}\left(\left(P_0H_0^3 + 3P_0\Delta HH_0^2 + \Delta PH_0^3\right)\left(\frac{\partial P_0}{\partial Z} + \frac{\partial\Delta P}{\partial Z}\right)\right) + \\
&\frac{\Gamma_s P_s}{\Delta\theta\Delta Z}\left(2\gamma_g \frac{k}{k-1}\right)^{1/2}\left(f(H_0,P_0) + \left.\frac{\partial f(P,H)}{\partial P}\right|_{P_0,H_0}\Delta P + \left.\frac{\partial f(P,H)}{\partial H}\right|_{P_0,H_0}\Delta H\right) \\
&= \Lambda\frac{\partial}{\partial\theta}\left(P_0H_0 + P_0\Delta H + H\Delta P\right) + 2\Lambda\nu\frac{\partial}{\partial\tau}\left(P_0H_0 + P_0\Delta H + H\Delta P\right)
\end{aligned} \tag{59}$$

Let the perturbations in pressure and film thickness be represented as

$$\Delta P = \sum_{\alpha=X,Y}\Delta\varepsilon_\alpha P_\alpha e^{i\tau},\ \Delta H = \sum_{\alpha=X,Y}\Delta\varepsilon_\alpha H_\alpha e^{i\tau} \tag{60}$$

Substituting and rearranging using the above perturbations expressions equation (59) can be written as

$$\left(\text{Zeroth Order terms}\right) + \sum_{\alpha=X,Y}\Delta\varepsilon_\alpha e^{i\tau}\left(\text{First Order terms}\right) = 0 \tag{61}$$

The above will be true for any $\Delta\varepsilon_\alpha$ if and only if

$$\text{Zeroth Order terms} = 0 \tag{62}$$

and

$$\text{First Order terms} = 0 \tag{63}$$

The above condition leads to Zeroth and First order equation as shown below

Zeroth order equation

$$\frac{\partial}{\partial\theta}\left(P_0H_0^3\frac{\partial P_0}{\partial\theta}\right)+\frac{\partial}{\partial z}\left(P_0H_0^3\frac{\partial P_0}{\partial z}\right)+\frac{\Gamma_sP_s}{\Delta\theta\Delta Z}\left(2\gamma_g\frac{k}{k-1}\right)^{\frac{1}{2}}f(H_0,P_0)$$
$$=\left(\Lambda\frac{\partial}{\partial\theta}\left(P_0H_0\right)+2\Lambda\nu\frac{\partial}{\partial\tau}\left(P_0H_0\right)\right) \tag{64}$$

First order equation

$$\frac{\partial}{\partial\theta}\left(\left(3P_0H_\alpha H_0^2+P_\alpha H_0^3\right)\frac{\partial P_0}{\partial\theta}\right)+\frac{\partial}{\partial Z}\left(\left(3P_0H_\alpha H_0^2+P_\alpha H_0^3\right)\frac{\partial P_0}{\partial Z}\right)$$
$$+\frac{\partial}{\partial\theta}\left(\left(3P_0H_\alpha H_0^2+P_\alpha H_0^3\right)\frac{\partial P_\alpha}{\partial\theta}\right)+\frac{\partial}{\partial Z}\left(\left(3P_0H_\alpha H_0^2+P_\alpha H_0^3\right)\frac{\partial P_\alpha}{\partial Z}\right)$$
$$+\frac{\partial}{\partial\theta}\left(P_0H_0^3\frac{\partial P_\alpha}{\partial\theta}\right)+\frac{\partial}{\partial Z}\left(P_0H_0^3\frac{\partial P_0}{\partial Z}\right) \tag{65}$$
$$+\frac{\Gamma_sP_s}{\Delta\theta\Delta Z}\left(2\gamma_g\frac{k}{k-1}\right)^{\frac{1}{2}}\left(\left.\frac{\partial f(P,H)}{\partial P}\right|_{P_0,H_0}P_\alpha+\left.\frac{\partial f(P,H)}{\partial H}\right|_{P_0,H_0}H_\alpha\right)$$
$$=\Lambda\frac{\partial}{\partial\theta}\left(P_0H_\alpha+H_0P_\alpha\right)+2\Lambda\nu\frac{\partial}{\partial\tau}\left(P_0H_\alpha+H_0P_\alpha\right)$$

Using relations between P_α and H_α from equation (46) in the above equation we get

$$\frac{\partial}{\partial\theta}\left[P_0{H_0}^3\frac{\partial P_\alpha}{\partial\theta}\right]+\frac{\partial}{\partial Z}\left[P_0{H_0}^3\frac{\partial P_\alpha}{\partial Z}\right]$$
$$+\left(\frac{2k}{k-1}\right)^{\frac{1}{2}}\frac{\Gamma_sP_s}{\Delta Z\Delta\theta}\left[\left.\frac{\partial f(P,H)}{\partial P}\right|_{P_0,H_0}P_\alpha+\left.\frac{\partial f(P,H)}{\partial H}\right|_{P_0,H_0}\left(\frac{P_a}{K_b\left(1+\eta i\right)}+g_\alpha\right)\right]$$
$$\frac{\partial}{\partial\theta}\left[\left(3{H_0}^2P_0\left(\frac{P_a}{K_b\left(1+\eta i\right)}+g_\alpha\right)+{H_0}^3P_\alpha\right)\left(\frac{\partial P_0}{\partial\theta}\right)\right] \tag{66}$$
$$+\frac{\partial}{\partial Z}\left[\left(3{H_0}^2P_0\left(\frac{P_a}{K_b\left(1+\eta i\right)}+g_\alpha\right)+{H_0}^3P_\alpha\right)\left(\frac{\partial P_0}{\partial Z}\right)\right]$$
$$=\Lambda\frac{\partial}{\partial\theta}\left(P_0\left(\frac{P_a}{K_b\left(1+\eta i\right)}+g_\alpha\right)+P_\alpha H_0\right)+2\Lambda\nu iP_0\left(P_0\left(\frac{P_a}{K_b\left(1+\eta i\right)}+g_\alpha\right)+P_\alpha H_0\right)$$

where $\alpha=X,Y$ and $g_X=\cos\theta$, $g_Y=\sin\theta$.

APPENDIX C

PTC CHARACTERISTICS

The characteristics of the positive type thermistor are shown in Figure 54.

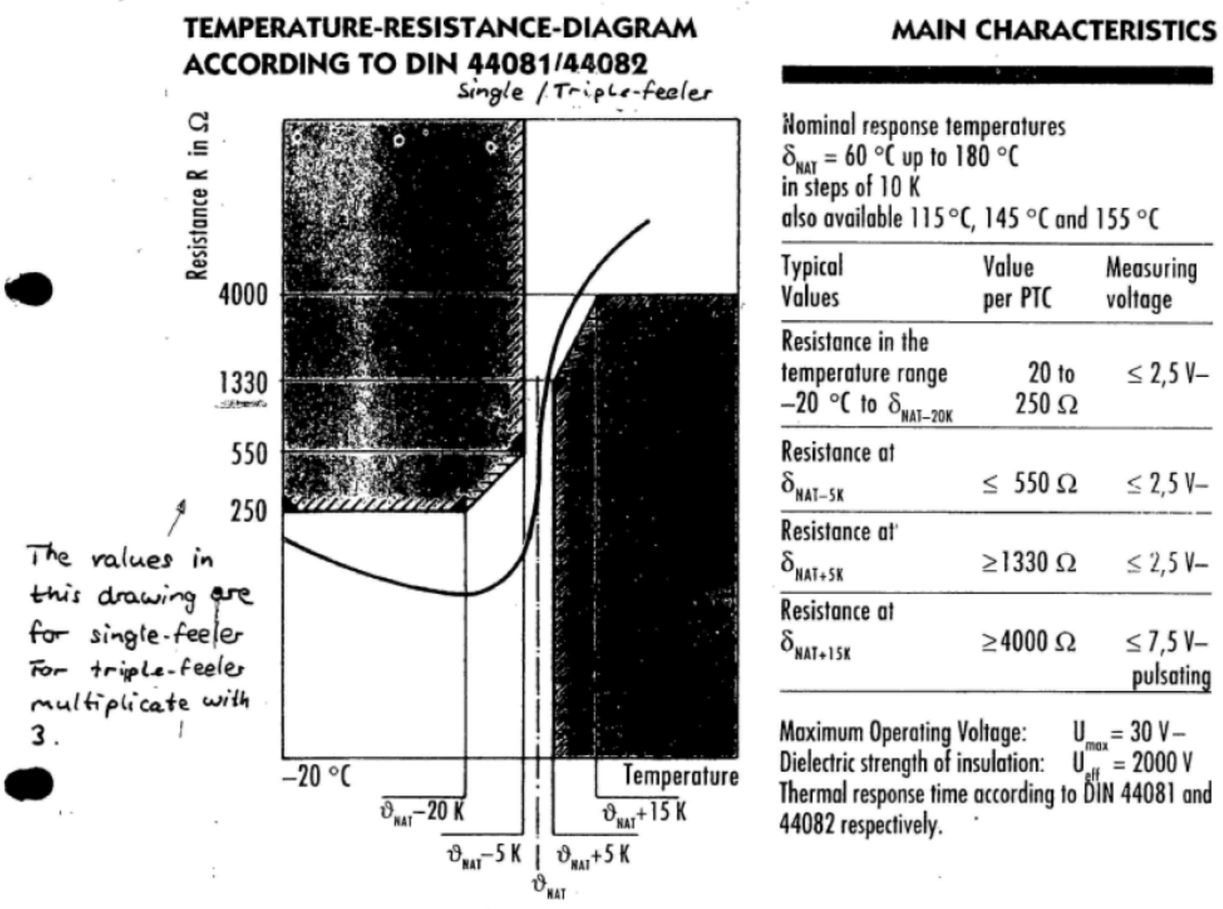

TEMPERATURE-RESISTANCE-DIAGRAM ACCORDING TO DIN 44081/44082

Single / Triple-feeler

The values in this drawing are for single-feeler For triple-feeler multiplicate with 3.

MAIN CHARACTERISTICS

Nominal response temperatures
δ_{NAT} = 60 °C up to 180 °C
in steps of 10 K
also available 115 °C, 145 °C and 155 °C

Typical Values	Value per PTC	Measuring voltage
Resistance in the temperature range –20 °C to $\delta_{NAT-20K}$	20 to 250 Ω	≤ 2,5 V–
Resistance at δ_{NAT-5K}	≤ 550 Ω	≤ 2,5 V–
Resistance at δ_{NAT+5K}	≥1330 Ω	≤ 2,5 V–
Resistance at $\delta_{NAT+15K}$	≥4000 Ω	≤ 7,5 V– pulsating

Maximum Operating Voltage: U_{max} = 30 V–
Dielectric strength of insulation: U_{eff} = 2000 V
Thermal response time according to DIN 44081 and 44082 respectively.

Figure 54: PTC characteristics, Source: Insta Controls [23]

APPENDIX D

CALIBRATION OF PROXIMITY PROBE

Below curve shows the calibration data of proximity probe installed near the test section (see Figure 34 on page 52) to measure the shaft bow. The x axis shows the vernier reading and the y axis the corresponding reading from the proximity probe. The specification of the vernier scale is given in Table 14.

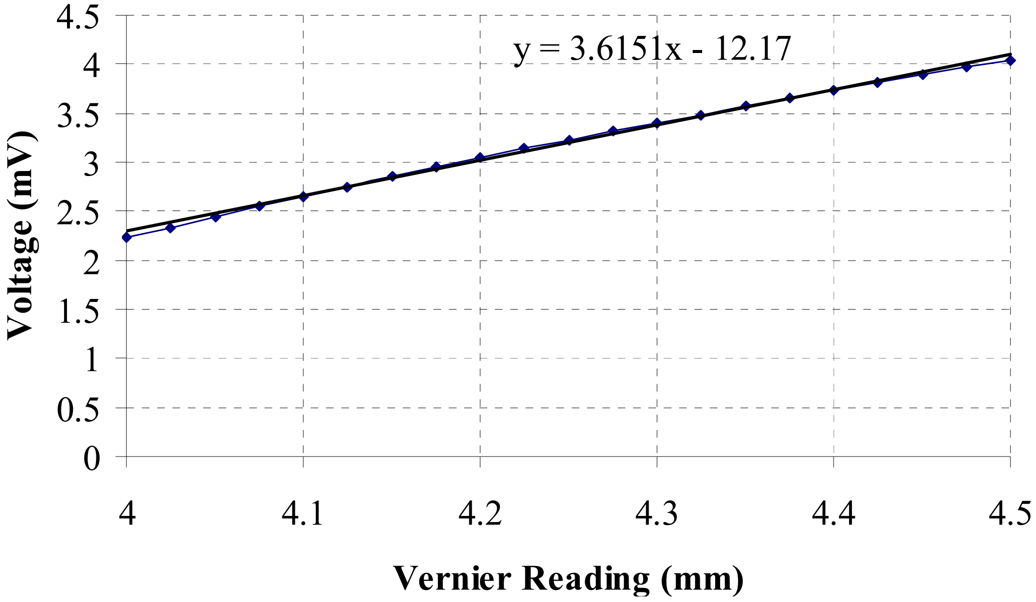

Figure 55: Calibration curve of proximity probe

Table 14: Vernier specifications, Source : Newport Corporation [24]

Parameter	Value
Thread Pitch (mm)	0.5
Graduations (µm)	10
Vernier Graduations (µm)	1
Sensitivity (µm)	1

APPENDIX E

BENCHMARKING OF SOLUTIONS

This section describes the benchmarking of the zeroth and first order solutions described in Section 3 with results from Kim [16]. Kim [16] presents a parametric study involving hydrodynamic gas bearings where the compliant structure is modeled by assigning average stiffness and damping values to individual computational grid points. Note that this model differs from the model in the present analysis since stiffness and damping are only assigned to grid points that lie on bumps.

For comparison, synchronous force coefficients were found under the limiting case of zero feed parameter. Zero feed parameter represents the case of no external pressurization and makes the bearing hydrodynamic. Table 15 show the hydrodynamic bearing parameters listed in [16]. Results from [16] and present analysis are shown in Table 16

Table 15: Bearing parameters in [16]

Parameters	Value
Bearing diameter, 2*R*	38.1 mm
Bearing axial length, *L*	38.1 mm
Nominal clearance, *C*	32 μm
Bump stiffness per unit area	4.7 GN/m^3
Load on Bearing	30 N
Structural Loss Factor	0.25

Table 16: Results comparison

Parameters	Present Case	Reference [16]	% Variation
e/C	0.63	0.4 ~ 0.6	–
c_{xx} (KN-s/m)	0.39	0.55	28.83
c_{yx} (KN-s/m)	0.19	0.20	7.02
k_{xx} (MN/m)	1.97	2.20	10.85
k_{xy} (MN/m)	0.49	0.39	23.67

Note that Kim [16] specifies a range of eccentricity and does not include attitude angle. Comparison shows that there is difference in the force coefficients values from the two analyses, which may be attributed to the different modeling of bearing compliant structure in the two analyses. Also, the present analysis includes sagging effect of the top foil which is absent in [16].

APPENDIX F

FABRICATION OF BUMP FOIL AND TOP FOIL

This section outlines the procedures and instructions for the fabrication of top foils and bump foils. Also included is the description of jigs used for the fabrication of foils.

Bump foil fabrication

Bump foils form the compliant structure in air foil bearings. Compliance from bump foils can help in accommodating misalignments, prevent high-precision manufacturing and provide greater damping. Bump foils made and used in the present study are generation I bump foils. This means that stiffness in the axial and circumferential directions are constant.

For fabrication of bump strips a forming jig was constructed in which the desired bump foil geometry was machined on two halves of the jig dies (see Figure 56). This machining was done using wire EDM. The description of the bump foil geometry is shown in Figure 57. The geometry was provided by Foster Miller Corporation, a leading foil bearing manufacturer. The bump foil fabrication procedure is as follows:

1. Cut a 4 mil (0.004”) thick stainless steel sheet of size 1.5” X 5”.
2. Place the sheet between the mating surfaces of the forming jig and align the two halves using the dowel pins (see Figure 56). Note that it is important to align the sheet properly in jig (sheet and jig should have parallel edges).
3. Compress the two halves of the forming jig using a hydraulic press. Load the press to a maximum force of 15 tons and bolt the jig.

4. Unload the hydraulic press and place the forming jig in a furnace for heat treatment. Heat the forming jig to a temperature of 500°C for four hours.
5. Switch off the furnace but keep the forming jig inside until the furnace temperature reaches room temperature.
6. Remove the jig from the furnace and place it under the hydraulic press again. Load the press to 15 ton force.
7. Remove the bolts and dowel pins and unload the press to get the bump foil.
8. Retain 26 bumps on the bump strip and cut away the rest.

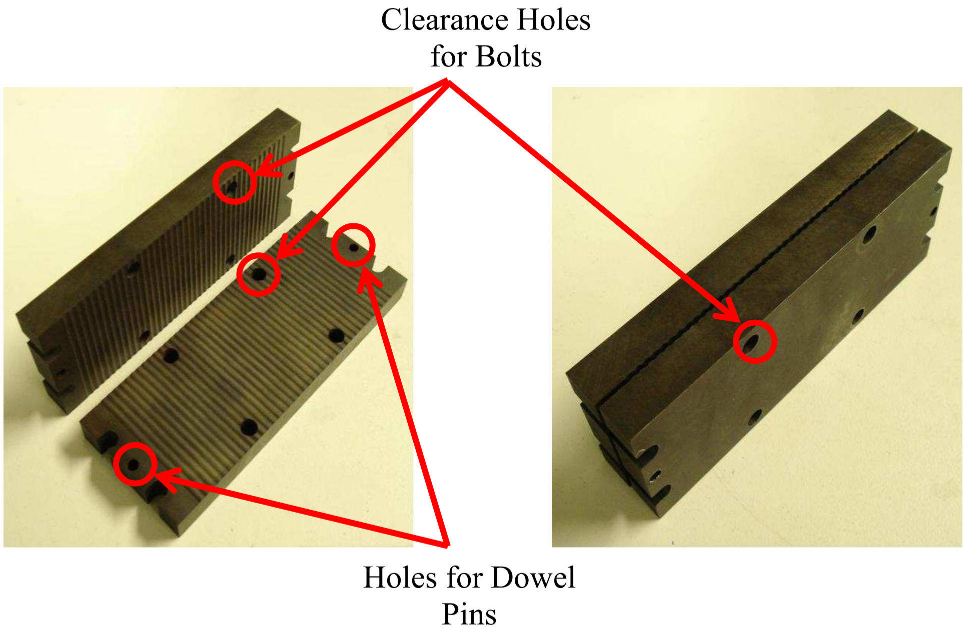

Figure 56: Two halves of the forming jig

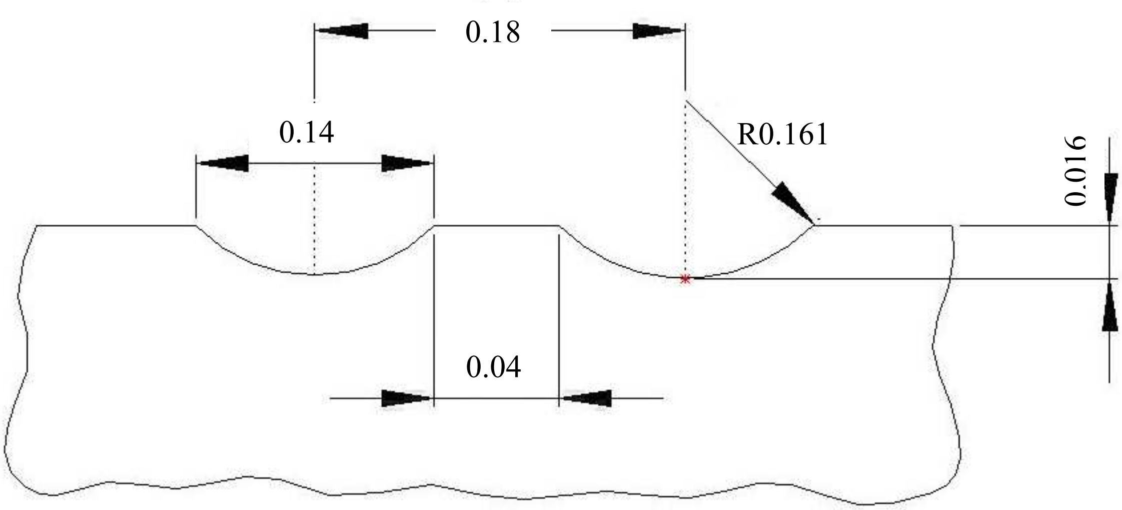

Figure 57: Bump foil geometry

Once the bump foil is formed a second heat treatment is done to make the foil circular in shape. The bump foil is wrapped around a mandrel, placed inside a forming jig and heat treated to 400°C. See Figure 58 for details on the mandrel and forming jig.

Note, the above fabrication process outlines the construction of a single strip bump foil. A bump foil may have 3-4 strips that are attached at one end. These types of bump foils provide enhanced axial compliance. To make such a bump foil one can start with a stainless steel sheet with appropriate strip cuts.

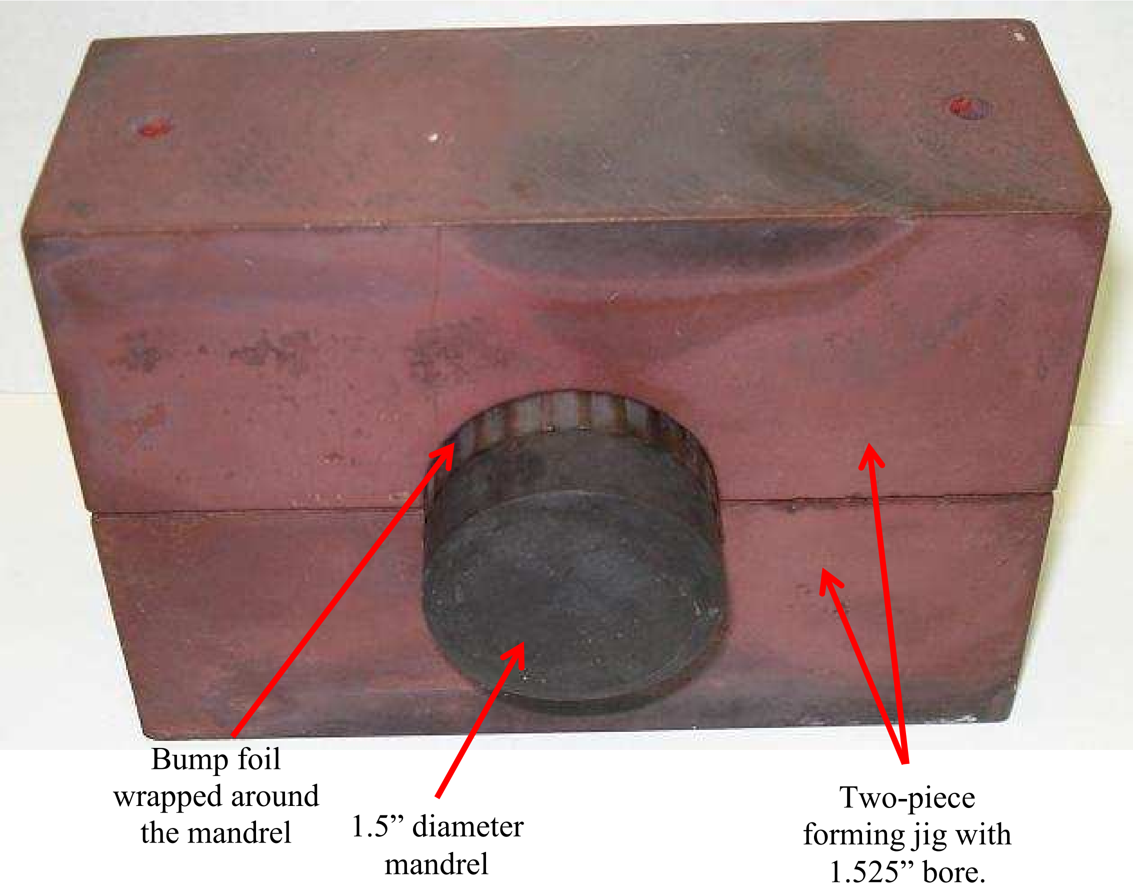

Figure 58: Forming jig with mandrel and bump foil

Top foil fabrication

Top foil makes the smooth surface of the compliant structure and is placed over the bump foil (see Figure 1 on page 2). Top foil is made using a 4 mil thick stainless steel sheet of size 1.5” X 5”. The construction of top foil is similar to the heat treatment process to make the bump foils circular. Here again the steel sheet is wrapped around the mandrel and placed in the forming jig. One of the edges of the steel sheet is bent and is inserted in the gap between the two halves of the forming jig (see Figure 59). The bent part is trimmed after the heat treatment and it goes inside a 0.012” groove in the bearing sleeve. The bent part locks in place the top-foil and the underlying bump foil circumferentially in the bearing sleeve, see Figure 2 on page 11 for details.

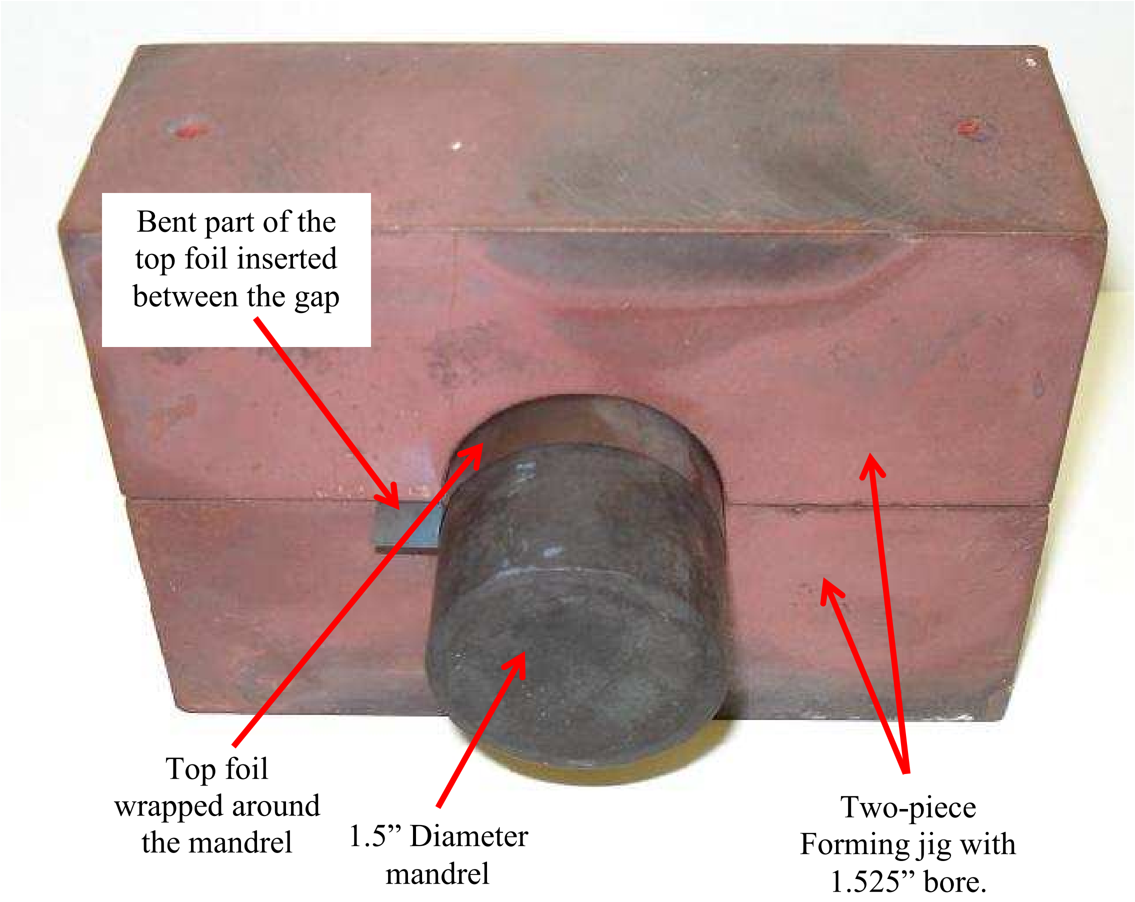

Figure 59: Forming jig with mandrel and top foil

VITA

Manish Kumar received his Bachelor of Technology in mechanical engineering from Indian Institute of Technology in 2004. He entered the mechanical engineering program at Texas A&M University in August 2006. His research areas include dynamics of rotating machinery, fluid dynamics and heat transfer.

Manish may be reached at R8/110 New Raj Nagar Ghaziabad, India 201002. His email is manish1268@gmail.com.